Remote Sensing of Environment 257 (2021) 112349

Contents lists available at ScienceDirect

Remote Sensing of Environment

journal homepage: www.elsevier.com/locate/rse

Review

NASA's surface biology and geology designated observable: A perspective on surface imaging algorithms

Kerry Cawse-Nicholson [a,*], Philip A. Townsend [b], David Schimel [a], Ali M. Assiri [c], Pamela L. Blake [d], Maria Fabrizia Buongiorno [e], Petya Campbell [f,g], Nimrod Carmon [a], Kimberly A. Casey [g,h], Rosa Elvira Correa-Pabón [i], Kyla M. Dahlin [j], Hamid Dashti [k], Philip E. Dennison [l], Heidi Dierssen [m], Adam Erickson [n,g], Joshua B. Fisher [a], Robert Frouin [o], Charles K. Gatebe [p], Hamed Gholizadeh [q], Michelle Gierach [a], Nancy F. Glenn [r,an], James A. Goodman [s], Daniel M. Griffith [t,p], Liane Guild [p], Christopher R. Hakkenberg [u], Eric J. Hochberg [v], Thomas R.H. Holmes [g], Chuanmin Hu [w], Glynn Hulley [a], Karl F. Huemmrich [f,g], Raphael M. Kudela [x], Raymond F. Kokaly [y], Christine M. Lee [a], Roberta Martin [z], Charles E. Miller [a], Wesley J. Moses [aa], Frank E. Muller-Karger [w], Joseph D. Ortiz [ab], Daniel B. Otis [w], Nima Pahlevan [ac,g], Thomas H. Painter [ad], Ryan Pavlick [a], Ben Poulter [g], Yi Qi [ae], Vincent J. Realmuto [a], Dar Roberts [af], Michael E. Schaepman [ag], Fabian D. Schneider [a], Florian M. Schwandner [p], Shawn P. Serbin [ah], Alexey N. Shiklomanov [g], E. Natasha Stavros [a,ad], David R. Thompson [a], Juan L. Torres-Perez [ai], Kevin R. Turpie [f,g], Maria Tzortziou [aj,g], Susan Ustin [ak], Qian Yu [al], Yusri Yusup [am], Qingyuan Zhang [n,g], the SBG Algorithms Working Group

[a] Jet Propulsion Laboratory, California Institute of Technology, Pasadena, CA, USA
[b] University of Wisconsin-, Madison, WI, USA
[c] KACST, Space and Aeronautics Research Institute, Riyadh, Saudi Arabia
[d] The Boeing Company, Seal Beach, CA, USA
[e] Istituto Nazionale di Geofisica e Vulcanologia, Italy
[f] University of Maryland Baltimore County (UMBC), MD, USA
[g] NASA Goddard Space Flight Center, MD, USA
[h] U.S. Geological Survey, Reston, VA, USA
[i] Instituto Tecnológico Vale Mineração, Ouro Preto, Brazil
[j] Michigan State University, East Lansing, MI, USA
[k] University of Arizona, School of Natural Resources and the Environment, Tucson, AZ, USA
[l] University of Utah, Salt Lake City, UT, USA
[m] Marine Sciences Department, University of Connecticut, Groton, CT, USA
[n] Universities Space Research Association (USRA), MD, USA
[o] Scripps Institution of Oceanography, University of California San Diego, La Jolla, CA, USA
[p] NASA Ames Research Center, Moffett Field, CA, USA
[q] Oklahoma State University, Stillwater, OK, USA
[r] University of New South Wales, Australia
[s] HySpeed Computing, Miami, FL, USA
[t] U.S. Geological Survey, Western Geographic Science Center, Moffett Field, CA, USA
[u] Northern Arizona University, AZ, USA
[v] Bermuda Institute of Ocean Sciences, St. George's, Bermuda
[w] University of South Florida, College of Marine Science, Saint Petersburg, FL, USA
[x] University of California, Santa Cruz, CA, USA
[y] U.S. Geological Survey, Denver, CO, USA
[z] Arizona State University, SGSUP & GDCS, AZ, USA
[aa] U.S. Naval Research Laboratory, Washington, D.C., USA
[ab] Kent State University, Dept. of Geology, Kent, OH, USA
[ac] Science Systems and Applications Inc., Lanham, MD, USA

* Corresponding author.

https://doi.org/10.1016/j.rse.2021.112349

Available online 20 February 2021
0034-4257/© 2021 The Authors. Published by Elsevier Inc. This is an open access article under the CC BY-NC-ND license (http://creativecommons.org/licenses/by-nc-nd/4.0/).

[ad] Joint Institute for Regional Earth System Science and Engineering, UCLA, CA, USA
[ae] University of Nebraska Lincoln, NE, USA
[af] University of California, Santa Barbara, CA, USA
[ag] University of Zurich, Department of Geography, Remote Sensing Laboratories, Zurich, Switzerland
[ah] Brookhaven National Laboratory, Environmental and Climate Sciences Department, Upton, NY, USA
[ai] Bay Area Environmental Research Institute, NASA Ames Research Center, Moffett Field, CA, USA
[aj] City University of New York, New York, NY, USA
[ak] University of California, Davis, CA, USA
[al] University of Massachusetts, Amherst, MA, USA
[am] Universiti Sains Malaysia, Penang, Malaysia
[an] Boise State University, USA

ARTICLE INFO

Editor: Jing M. Chen

Keywords:
Hyperspectral
Remote sensing
Thermal infrared
Vegetation
Snow
Volcano
Aquatic

ABSTRACT

The 2017–2027 National Academies' Decadal Survey, *Thriving on Our Changing Planet*, recommended Surface Biology and Geology (SBG) as a "Designated Targeted Observable" (DO). The SBG DO is based on the need for capabilities to acquire global, high spatial resolution, visible to shortwave infrared (VSWIR; 380–2500 nm; ~30 m pixel resolution) hyperspectral (imaging spectroscopy) and multispectral midwave and thermal infrared (MWIR: 3–5 μm; TIR: 8–12 μm; ~60 m pixel resolution) measurements with sub-monthly temporal revisits over terrestrial, freshwater, and coastal marine habitats. To address the various mission design needs, an SBG Algorithms Working Group of multidisciplinary researchers has been formed to review and evaluate the algorithms applicable to the SBG DO across a wide range of Earth science disciplines, including terrestrial and aquatic ecology, atmospheric science, geology, and hydrology. Here, we summarize current state-of-the-practice VSWIR and TIR algorithms that use airborne or orbital spectral imaging observations to address the SBG DO priorities identified by the Decadal Survey: (i) terrestrial vegetation physiology, functional traits, and health; (ii) inland and coastal aquatic ecosystems physiology, functional traits, and health; (iii) snow and ice accumulation, melting, and albedo; (iv) active surface composition (eruptions, landslides, evolving landscapes, hazard risks); (v) effects of changing land use on surface energy, water, momentum, and carbon fluxes; and (vi) managing agriculture, natural habitats, water use/quality, and urban development. We review existing algorithms in the following categories: snow/ice, aquatic environments, geology, and terrestrial vegetation, and summarize the community-state-of-practice in each category. This effort synthesizes the findings of more than 130 scientists.

1. Introduction

The 2017–2027 Decadal Survey, *Thriving on our Changing Planet*, was released in January 2018 by the committee on the Decadal Survey for Earth Science and Applications from Space (ESAS) of the National Academy of Sciences, Engineering and Medicine (NASEM) Space Studies Board (NASEM, 2018). The report provides a vision and strategy for Earth observation that informs federal agencies responsible for the planning and execution of civilian space-based Earth-system programs in the coming decade, including the National Aeronautics and Space Administration (NASA), the National Oceanic and Atmospheric Administration (NOAA), and the U.S. Geological Survey (USGS). High-priority emphasis areas and targeted observables include global-scale Earth science questions related to hydrology, ecosystems, weather, climate, and solid earth. Notably, the Decadal Survey identified Surface Biology and Geology (SBG) as a Designated Observable (DO) to acquire concurrent global spectroscopic (hyperspectral) visible to shortwave infrared (VSWIR; 380–2500 nm) and multispectral midwave and thermal infrared (MWIR: 3–5 μm; TIR: 8–12 μm) imagery at high spatial resolution (~30 m in the VSWIR and ~ 60 m in the TIR) and sub-monthly temporal resolution globally. An introduction to the mission and summary of the first community workshop is provided by Schneider et al. (2019). The final sensor characteristics will be determined during the mission formulation phase, but the Decadal Survey provides guidance for a VSWIR instrument with 30–45 m pixel resolution, ≤16 day global revisit, SNR > 400 in the VNIR, SNR > 250 in the SWIR, and 10 nm sampling in the range 380–2500 nm. It also recommends a TIR instrument with more than five channels in 8–12 μm, and at least one channel at 4 μm, ≤60 m pixel resolution, ≤3 day global revisit, and noise equivalent delta temperature (NEdT) ≤0.2 K (NASEM, 2018; Schimel et al., 2020). Alone, SBG will provide a comprehensive monitoring approach globally. Complemented with systems like Landsat and Sentinel-2, global change processes with faster than 16-day global change rates can be mapped—at lower spectral resolution—but high temporal revisit. Synergistic approaches to coexisting Earth observation missions are assumed to deliver additional science beyond the SBG promise (cf. Malenovsky et al., 2012).

This unique combination of high spatial resolution VSWIR and TIR spectral imagery is intended to capture the hydrological, ecological, weather, climate, and solid earth dynamic states of the Earth's surface and quantify uncertainties. The results will address a range of outstanding global Earth science questions and facilitate new applications that target pressing societal priorities.

Spectral imaging has been employed since the earliest days of Earth remote sensing, originating with black and white, then color photography from balloons, pigeons, and airplanes (Chuvieco, 2020). The first satellite imagery of the Earth was returned by NASA's TIROS Program (Television Infrared Observation Satellite) in the early 1960s (Stroud, 1960; Bandeen et al., 1961), demonstrating the power of space-based observations to improve global weather forecasts. Since then, space-based TIR and reflected solar spectral imagery has been acquired more or less continuously (Manna, 1985).

Passive remote sensing techniques have expanded to span the electromagnetic spectrum from the ultraviolet to microwave, and active remote sensing such as radar and lidar has been used to provide additional information on forest structure, topography, oceanography, clouds, and many other areas, with applications in biomass estimation, earthquake monitoring, weather predictions, sea level rise, among many others (Thenkabail et al., 2018). Active and passive imaging in the microwave is often used in the monitoring of sea ice, snow and water content of soils and vegetation, alongside other applications (Thenkabail et al., 2018). All of these measurements are vital to understand the whole Earth surface and are covered in part by existing and other recommended missions in the Decadal Survey (NASEM, 2018). Here we focus on passive imaging in the visible to thermal wavelengths. We define panchromatic imagery as a single image acquired over a single (potentially broad) spectral channel; multispectral imagery as the simultaneous acquisition of tens of channels; and hyperspectral imagery

as the simultaneous acquisition of hundreds of channels.

Multispectral instruments such as Landsat 8 Operational Land Imager, Sentinel-2 MultiSpectral Instrument, Terra and Aqua MODIS, Suomi National Polar-Orbiting Partnership VIIRS, and others are commonly used for applications such as landcover classification, wildfire detection, urban growth, volcanology, detection of harmful algal blooms and oil spills, estimation of chlorophyll concentration, primary production, water transparency, resuspended particles, among others (Chuvieco, 2020). However, additional information is to be gained by measuring contiguous swaths of the spectrum at high spectral resolution (usually 10 nm or less) (Schimel et al., 2020). We label this spectroscopy (Schaepman et al., 2009), which, alongside thermal multispectral observations, forms the key measurement of SBG. We anticipate that these data will be complementary to the existing suite of remote sensing

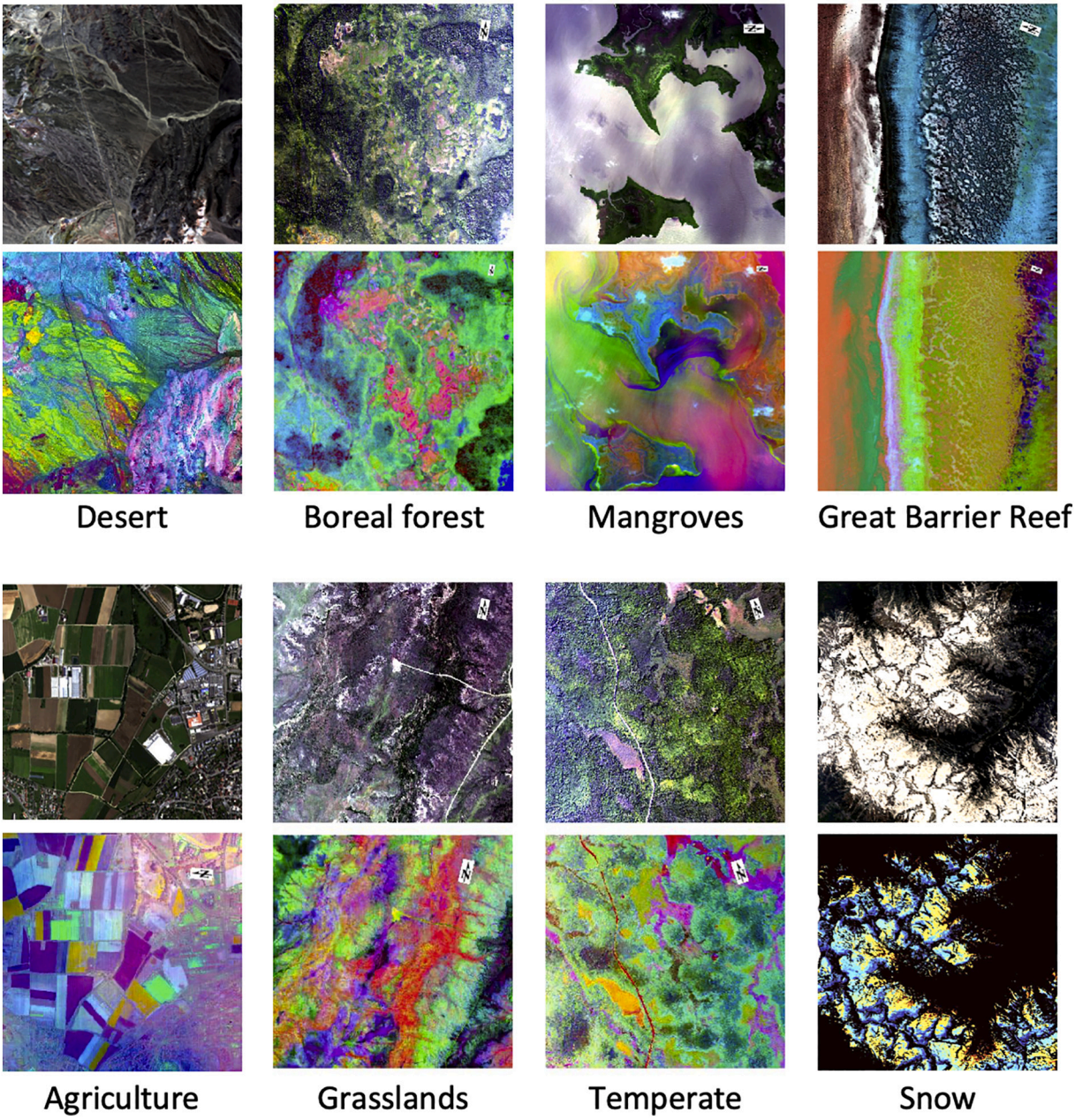

Fig. 1. Examples of spectroscopic imagery for terrestrial applications. Top and third rows: true color composites acquired by airborne AVIRIS-Classic (VSWIR), AVIRIS-NG (VSWIR), PRISM (visible to near-infrared; VNIR, 350-1050 nm) and HyTES (TIR) instruments over different biomes. Second and fourth rows: A minimum-noise fraction (MNF; Green et al., 1988) transformation is applied to each spectroscopic image to illustrate the additional information that can be derived from the spectral content (MNF bands 2,3,4 as red, green, blue, respectively). Each image covers approximately 4 km^2. The desert image was acquired by HyTES over Cuprite, Nevada, USA on 3 May 2015 (https://hytes.jpl.nasa.gov/order); the boreal forest image was acquired by AVIRIS-NG in the Northwest Territories, Canada on 11 August 2018 (https://avirisng.jpl.nasa.gov/dataportal/); the mangrove scene was acquired by AVIRIS-NG in Louisiana, USA on 9 May 2015; the Great Barrier Reef, Australia was acquired by PRISM on 17 September 2016 (https://prism.jpl.nasa.gov/prism_data.html); the agricultural image was acquired by AVIRIS-NG in Zurich, Switzerland on 9 July 2018; the grasslands image was acquired by AVIRIS-NG in Oklahoma, USA on 14 June 2017; the temperate forest was acquired by AVIRIS-NG in Wisconsin, USA on 4 September 2015; and the snow image was acquired by AVIRIS-Classic over Senator Beck Basin, Colorado on 15 June 2011. For AVIRIS-Classic, AVIRIS-NG and PRISM, color images are shown using the channels closest to 640 nm, 550 nm, and 470 nm for red, green and blue, respectively. For HyTES, a false-color composite is shown using 11.04 μm, 9.35 μm, and 8.56 μm as red, green, and blue, respectively. (For interpretation of the references to color in this figure legend, the reader is referred to the web version of this article.)

instruments planned and currently in orbit. In many applications, such as the identification and quantification of the biochemical components of plant canopies, the Decadal Survey states that spectroscopic imagery is the "only" sufficient technology (NASEM, 2018; Schimel et al., 2020).

Spectroscopic imagery contains far more information than can be seen by the human eye, as illustrated in Fig. 1, where a depiction of a small subset of the spectroscopic data reveals mineral types, vegetation species and health, water quality, and more. The VSWIR spectrum covers wavelengths that provide information about vegetation pigments, structure, water content, and non-pigment biochemistry; mineral composition; snow grain size and dust; water quality; and other applications (Fig. 2). SBG observations in this range will also be critical to derive complementary and high spatial resolution (compared to heritage ocean color sensors) Essential Ocean Variables (EOVs) and Essential Biodiversity Variables (EBVs) that are the basis for new aquatic science and applications (Muller-Karger et al., 2018; O'Connor et al., 2020). The TIR measures wavelengths that enable identification of minerals that do not have absorption or reflectance features in the VSWIR and provides information about vegetation water content (Fig. 3). In addition to emissivity changes, the midwave infrared (MWIR, 3–5 μm) and TIR radiance can also be used to compute land surface temperature. This is important for monitoring fires and lava flows, as well as drought and vegetation stress (Fig. 4).

The information content of each acquired scene is a function of the spatial and spectral resolution as well as the signal-to-noise ratio (SNR). Within hyperspectral imagery, there is often a tradeoff between noise and resolution, as finer division of pixels or channels results in fewer available photons per pixel per channel, whereas broad channels may

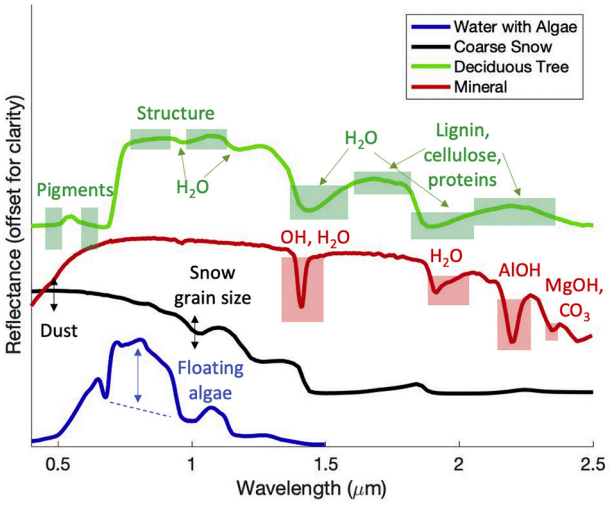

Fig. 2. Example spectra of reflected light to illustrate processes at different wavelengths. For instance, vegetation pigments (e.g., chlorophyll) can be evaluated in groups of narrow channels in the range 400–700 nm, with different pigments expressing absorption features at a range of wavelengths, whereas structure (e.g., size and arrangement of leaves within a canopy or cellular structure within leaves) impacts the range 0.8–1.2 μm, and lignin, cellulose, proteins, and other non-pigment plant components impact the shortwave infrared wavelengths. Many diagnostic mineral features are found beyond 2 μm, and these can be small and require fine spectral resolution (<10 nm) to distinguish. The boxes encompass the features of interest, and several spectral channels are required within each box to determine the feature shape. Snow grain size and dust impact the amplitude (denoted by arrows) of snow reflectance around 1 and 0.5 μm, respectively. Floating algae causes an increase in reflectance in a water spectrum between 0.7 and 1 μm (note that when algae do not aggregate at the surface, reflectance in this wavelength range is typically much lower than in the visible, and both reflectance shapes and magnitudes can vary substantially). In all applications, multiple absorption features throughout the visible to shortwave infrared shed light on important physical characteristics and processes on the ground.

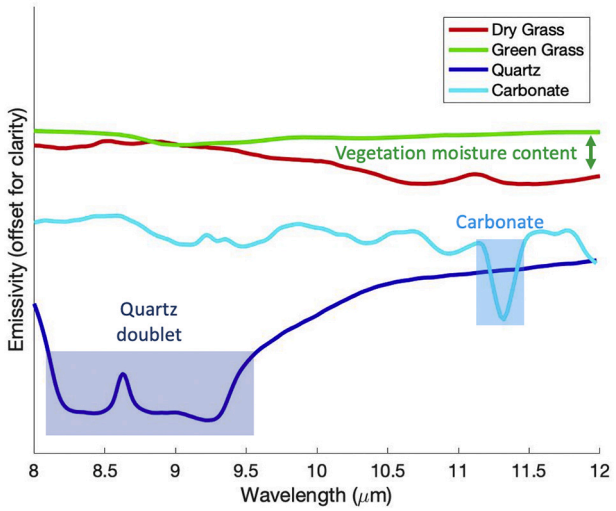

Fig. 3. Silicates and feldspar minerals are difficult to detect using the VSWIR spectral range but can be identified by features in the TIR. Water content in vegetation also impacts the energy emitted in the thermal part of the spectrum, and thermal indicators of vegetation stress are used as an input into evapotranspiration models. A combination of VSWIR and TIR wavelength ranges yields complementary spectral information.

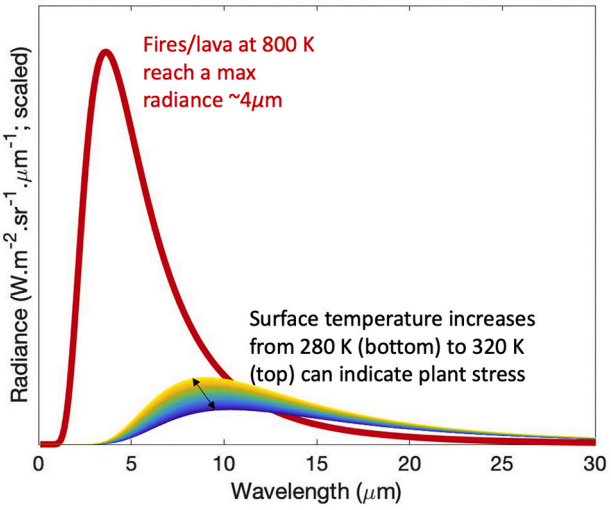

Fig. 4. The Planck curve shows the radiation of a blackbody at different temperatures across the electromagnetic spectrum. The radiation peaks at different wavelengths depending on temperature: extreme heat such as fires and lava are best detected in the midwave infrared (~4 μm), whereas typical Earth surface temperatures are best detected in the range 7–12 μm. Small changes in surface temperature can be used to detect the beginnings of plant stress, before the vegetation turns brown. (For interpretation of the references to color in this figure legend, the reader is referred to the web version of this article.)

return more photons but miss key identifying features. The intrinsic dimension (ID) of an image is the number of unique detectable classes within an image or the observable degrees of freedom within a particular electromagnetic range. A survey of dimensionality across space, time, and land cover types is shown for airborne hyperspectral imaging in Thompson et al. (2017a), and the fusion of VSWIR and TIR ranges has been shown to yield significantly more degrees of freedom than a single modality alone (Cawse-Nicholson et al., 2019).

The Decadal Survey calls for specific products, including Earth surface temperature and emissivity; VSWIR reflectance; vegetation traits; evapotranspiration; substrate composition; volcanic gases and plumes;

high temperature features; water biogeochemistry; water biogeophysics; aquatic and terrestrial classification; and snow albedo. Here, we focus on the state-of-the-practice algorithms used to derive the products identified by the Decadal Survey. All of the overarching science and societal questions/goals assigned to the SBG DO were considered when selecting products. Decadal Survey questions are divided into the focus areas of the hydrological cycle (H), weather (W), terrestrial and aquatic ecosystems and natural resource management (E), climate variability and change (C), and Earth surface and interior (S). These labels are used in tables henceforth, with the exact question codes provided in the Decadal Survey (NASEM, 2018).

This paper is organized as follows: in Section 2, we survey the state-of-practice algorithms for SBG core products; in Section 3, we address caveats and other algorithm/product considerations; Sections 4 and 5 follow with a discussion and conclusion, respectively.

2. The diversity of surface imaging algorithms

The SBG Algorithms Working Group surveyed more than 130 imaging spectroscopy researchers spanning the hydrology, ecosystems, weather, climate, and solid earth communities. This year-long interdisciplinary collaboration gathered information on algorithms and data products that address the SBG science questions. Section 2 summarizes 22 potential product suites and nearly 100 subproducts contained therein, per the survey results. In section 2.1, we cover universal products, and in section 2.2, we detail products within each science and application domain. This work serves as a record of the state-of-the-practice as it represents a community of scientists interested in the SBG Designated Observable. We do not present the list of algorithms that will be implemented for SBG, but rather document the breadth of potential algorithms suitable for SBG, with a focus on those that require measurements such as are proposed for SBG.

2.1. Universal algorithms

Several universal preprocessing steps are required to produce many of the products listed in Section 2.2, including atmospheric correction in the VSWIR and TIR, spectral unmixing and sometimes land cover classification.

2.1.1. Atmospheric correction

Most products described in this manuscript start from a foundation of atmospheric correction, which estimates atmospheric properties related to aerosols, trace gases, and water vapor as a basis to remove atmospheric interference and convert data to surface reflectance or emissivity. The atmosphere varies at fine spatiotemporal scales, with the time scales of variation decreasing in duration at increasingly finer spatial resolutions. Thus, while climatological or model-based estimates may provide background constraints, it is important to estimate the atmospheric contribution to the spectral and thermal signals directly from the targets being measured. Historically, different communities have applied algorithms developed for their specific domains and instruments. In the terrestrial domain, VSWIR and TIR retrievals have been treated separately due to the underlying differences in radiative transfer and physics between the two wavelength regions.

2.1.1.1. Visible shortwave infrared (VSWIR). The SBG concept involves collection of imaging spectroscopy data with global coverage and provision of surface reflectance maps with per-spectral channel and per-pixel uncertainty estimates. Those uncertainties are of special significance for global observations, as different biomes, atmospheric conditions, observation geometries, and illumination geometries yield spatially and temporally varied retrieval accuracies (Thompson et al., 2019a, 2019c). The primary objective of VSWIR atmospheric correction is the accurate retrieval of surface reflectance, removing effects of light absorption and scattering by aerosols, water vapor, ozone, and other gases, particularly in visible wavelengths and with variation in elevation and solar illumination. In addition to surface reflectance, atmospheric correction algorithms also yield useful maps of atmospheric column vapor content.

In the VSWIR, recent algorithm surveys include Frouin et al. (2019) for ocean environments, and Thompson et al. (2019b) and Ientilucci and Adler-Golden (2019) for terrestrial environments. In aquatic and near-coastal environments, only a small fraction of sensor-reaching radiance constitutes relevant information about water-column or benthic properties, requiring a more rigorous accounting of atmospheric signal than is necessary for terrestrial applications (Gordon and Wang, 1994; Gordon, 1997; Wang, 2007; Palacios et al., 2015). Generally, this necessitates high-performance instrumentation and calibration (Meister et al., 2011). Traditionally, aquatic algorithms are based on the assumptions that reflectance at longer wavelengths—usually red, near-infrared (NIR), and shortwave infrared (SWIR) —is either negligible (i.e., below sensor noise) or well correlated to enable iterations. Such assumptions are mostly applicable, with exceptions due to oil spills (Clark et al., 2010; Lu et al., 2019) or other types of floating matters on the water surface (Hu, 2009; Qi et al., 2016; Wang and Hu, 2016; Qi et al., 2020). While hyperspectral algorithms developed for atmospheric correction in ocean environments have shown promise for coastal and inland waters (Ibrahim et al., 2018), other alternative methods have also been developed, such as curve-fitting algorithms (POLYMER; Steinmetz et al., 2011) and neural network models (OCSMART; Fan et al., 2017). In developed coastal areas, in addition to aerosols, highly variable absorbing trace gases such as NO_2 introduce additional uncertainties in estimates of surface reflectance at wavelengths traditionally used for retrievals of phytoplankton pigments and dissolved organic carbon dynamics (Ahmad et al., 2007; Tzortziou et al., 2014). Regional/empirical algorithms (e.g., line height methods) have proven practical for the retrieval of some water quality parameters (e.g., chlorophyll-a) directly from top-of-atmosphere (TOA) radiance/reflectance, taking advantage of strong reflectance features that are prominent even in the presence of atmospheric effects (Stumpf et al., 2016; Binding et al., 2018).

In general, atmospheric correction approaches fall into three categories: (1) *empirical or scene-based approaches*, which are not discussed here because they do not scale to global implementation, (2) *sequential methods*, which estimate atmospheric content from radiance data prior to inverting for surface reflectance, and (3) *simultaneous approaches* that fit atmospheric and surface properties simultaneously. *Sequential methods* are generally faster because they use fast algebraic solutions or pre-formulated lookup tables (LUTs) from cached sets of common optical atmospheric conditions. The atmospheric state is estimated using features in the radiance spectrum, with reflectance then inverted from radiance as an algebraic function of atmospheric transmission and path radiance from the LUT (Thompson et al., 2019a). Examples include ATREM (Gao et al., 2009), ATCOR (Richter and Schläpfer, 2017), and FLAASH (Perkins et al., 2012) for the land, and different, long-standing algorithms for the ocean (Gordon and Wang, 1994; Gordon, 1997; Montes et al., 2001; Wang, 2007). Complex landscapes confound sequential methods (Thompson et al., 2019a). While some *simultaneous* methods are slower due to iterative computations (i.e., optimization), they fit the entire spectrum by concurrently solving for the atmosphere and surface; that is, they do not make assumptions about the atmosphere as sequential methods do. This provides the accuracy and flexibility to measure subtle atmospheric parameters lacking obvious visible cues. Statistical versions may incorporate background information for improved accuracy, and enable rigorous uncertainty accounting (e.g., Optimal Estimation in Thompson et al., 2018, 2019a, 2019b, 2019c; and Chomko et al., 2003; Steinmetz et al., 2011; Bayesian Methods in Frouin and Pelletier, 2015; Frouin and Gross-Colzy, 2016). This class of algorithm has the flexibility to use diverse ancillary surface and atmosphere information where available, including multiple observations of the same location that can serve as a prior reflectance base map enabling

improved accuracy. However, these methods often constrain the retrieved surface reflectance to known sets of spectra and may not accurately retrieve new spectral information, particularly because global hyperspectral data are lacking, especially in aquatic environments (Dierssen et al., 2020). Finally, atmospheric correction algorithms designed for terrestrial and aquatic applications often have fundamental differences in defining the atmospheric path radiance: terrestrial algorithms typically do not include the surface reflected light, but aquatic algorithms include the light due to Fresnel reflection, a function of not only water's refraction index and observing geometry, but also winds (for surface roughness calculations).

2.1.1.2. Thermal infrared (TIR). Maximum radiometric emission for the typical range of Earth surface temperatures occurs in two infrared spectral "window" regions that have minimal interference from atmospheric absorption and scattering—the 3–5 μm MWIR and the 8–12 μm TIR. The radiance measured in these windows includes emission, absorption and scattering by atmospheric constituents. As with VSWIR, the purpose of the atmospheric correction for TIR data is to remove the atmospheric effects and isolate those features of the observation that are intrinsic to the surface. Only after accurate atmospheric correction can reliable surface temperatures and spectral emissivity be retrieved.

For TIR, a sequential approach is generally used by first estimating atmospheric profiles, then inputting these into a radiative transfer model such as MODTRAN (Berk et al., 1999) or Radiative Transfer for TOVS (RTTOV; where TOVS is the TIROS Operational Vertical Sounder, and TIROS is the Television Infrared Observation Satellite) (Matricardi et al., 2001) to estimate the necessary atmospheric parameters, and then inverting to obtain surface radiance. Even with perfect knowledge of the atmospheric properties, the problem of separating surface temperature and emissivity from multispectral TIR measurements is a non-deterministic problem. This is because the total number of measurements available (N channels) is always less than the number of variables to be solved for (emissivity in N channels, and one surface temperature $= N + 1$). If the emissivity is assumed *a priori* from a land-cover classification or over water, then the problem becomes deterministic with only the surface temperature being the unknown variable, and various split-window formulations can be used (Price, 1984; Prata, 1994; Wan and Dozier, 1996; Coll and Caselles, 1997; Yu et al., 2008; Minnett et al., 2019). Non-deterministic approaches can be applied to multispectral sensors with three or more channels in the TIR (e.g., ASTER, ECOSTRESS, MODIS) so that spectral variations in the retrieved emissivity can be related to surface composition and cover, in addition to retrieving surface temperatures. In non-deterministic approaches, the temperature and spectral emissivity are solved using an additional constraint or extra degree of freedom that is independent of the data source. These types of solutions are able to account for dynamic land surface changes such as those due to wildfires or surface soil moisture since the emissivity retrieval is based on spectral variance in the observed radiances. Example non-deterministic approaches include the MODIS day/night algorithm (Wan and Li, 1997), the temperature-independent spectral indices (TISI) algorithm (Becker and Li, 1990), Kalman filter (KF) (Masiello et al., 2013), and the Temperature Emissivity Separation (TES) algorithm (Gillespie et al., 1998; Kealy and Hook, 1993). Of these, the TES algorithm is currently used operationally for a number of NASA TIR sensors in low-Earth orbit, including VIIRS (VNP21) in Version 1, MODIS land surface temperature (LST) (MOD21/MYD21) products in Collection 6 (Hulley et al., 2012; Islam et al., 2017; Malakar and Hulley, 2016), and the ECOSTRESS Level-2 standard products (Hulley and Hook, 2018).

2.1.2. Spectral Unmixing and surface cover

Precursor steps are necessary for some algorithms in all application areas, such as partitioning pixels into cover fractions (Roberts et al., 1998; Asner and Heidebrecht, 2002; Painter et al., 2003; Asner et al., 2009; Jones et al., 2018) or pre-classification of surface cover necessary for implementation of surface-type dependent algorithms (e.g., view-angle dependent corrections where surface vertical structure affects model parameterization; Jensen et al., 2018). Likewise, some downstream algorithms may require fractional cover to correct for non-vegetation proportions of pixels (Serbin et al., 2015). Here, we do not exhaustively review the range of classification approaches available for generation of categorical maps from SBG data, but we note that (1) basic cover type classifications will likely be necessary for some algorithms for every scene that is acquired to reduce issues with geometric misalignment or change that would result from using stock classification layers, and (2) a range of methods are available for classifying imagery based on reference (training) data (e.g., random forests, support vector machines), and that VSWIR and TIR data offer opportunities for improved detail and accuracy in surface cover classification compared to multispectral imagery (Pande and Tiwari, 2013; Loncan et al., 2015).

Fractional cover algorithms allow for mapping of subpixel surface composition by finding the best-fit combination and fraction of pure "endmembers" that represent a pixel spectrum. Spectral features caused by chemical and/or particle size differences between different surfaces are essential for distinguishing endmembers and modeling their fractional contributions to mixed pixels. The fine resolution and contiguous spectra provided by VSWIR instruments are able to resolve the spectral features needed to "unmix" pixel spectra using spectral mixing models. Example applications include fractional snow cover and grain size (Painter et al., 2003), fractional cover of substrate and photosynthetic and non-photosynthetic vegetation (Dennison et al., 2019), forest cover, deforestation, and disturbance (e.g., Asner et al., 2005), burn proportion and recovery (Tane et al., 2018), fractional cover of impervious surfaces and vegetation in urban environments (Roberts et al., 2015), fire fractional area (Dennison et al., 2006), fractional cover of coral, algae, and sand (Hochberg and Atkinson, 2003), and fractional coverage of floating materials like vegetation (Wang et al., 2019) and plastic debris (Biermann et al., 2020). In the aquatic community, spectroscopic methods have been demonstrated for numerous retrievals related to water surface and column composition (Roesler et al., 2003; Bracher et al., 2009) and were recommended for spaceborne spectrometers (Devred et al., 2013), but approaches have not been widely tested across diverse aquatic regimes (Muller-Karger et al., 2018). Various methods have been proposed to unmix phytoplankton groups from hyperspectral reflectance with the majority focused on decomposing reflectance and/or absorption features related to pigments (Palacios et al., 2015; Wang et al., 2016; Chase et al., 2017; Mouw et al., 2017), with others focused on statistical methods using eigenvalue-eigenvector decomposition (Ortiz et al., 2019) or neural networks (Hieronymi et al., 2017). Fractional cover of various floating algae on the water surface has been explored by Hu et al. (2009), Qi et al. (2016), and Wang and Hu (2016).

2.2. Focused products and algorithms

Once the reflectance and emissivity are estimated from radiance data, a large number of specific algorithms exist to answer the science questions laid out in the Decadal Survey. In this section, we cover the algorithms used in snow/ice, aquatic environment, geology, and terrestrial vegetation applications. For all of the algorithms reported, we also note dependencies, which are intermediate algorithms or products necessary for implementation of an algorithm. An example is BRDF (bidirectional reflectance distribution function) and topographic correction for sun-sensor-target geometry that is sometimes needed for vegetation studies (Ma et al., 2020; Vögtli et al., 2021). In fact, these intermediate algorithms may result in products for distribution themselves, but an exhaustive list of potential intermediate algorithms is beyond the scope of this paper; such information can be found in individual references associated with specific products.

2.2.1. Snow

Monitoring of snow is important because large populations rely on snowmelt for water availability. In addition, snow has associated implications for water resources, weather, climate, flooding, and drought. The melt rate of snow is affected by snow grain size, presence of algae and particulates, surface temperature, and albedo. In addition, it can be difficult to separate snow from clouds in optical imagery, presenting challenges to the determination of the fractional area occupied by snow. Historically, MODIS data have been used to provide global maps of snow cover (Rittger et al., 2013). However, MODIS is a discontinuous multiband radiometer with isolated 50–100 nm wide spectral bands, whereas the SBG VSWIR instrument is envisioned to provide continuous spectral coverage from 400 to 2500 nm with ~10 nm spectral resolution. The combination of improved spectral resolution and continuous spectral coverage provides dramatically increased information content/spectral dimensionality (Thompson et al., 2018). Hyperspectral data leverage the entire spectrum to more accurately determine snow albedo, grain size, cloud cover over snow, and unmix pixels containing both vegetation and snow (Painter et al., 2013). A model developed by Painter et al. (2013) compares the observed snow reflectance (scaled by a hemispherical-directional reflectance factor; HDRF) to a library spectrum. The absorption feature at 1.03–1.06 μm can be used to derive snow grain size, and the difference between the observed snow spectrum and a library spectrum of the same grain size can be used to determine light absorbing impurities (Painter et al., 2013). Table 1 lists the snow subproducts with their dependencies and heritage, while Table 2 lists the algorithms typically used to derive these subproducts.

2.2.2. Aquatic environment

The aquatic environment comprises inland seas, lakes and rivers; nearshore coastal, estuarine and oceanic waters; and the margins of water bodies near shorelines or the edges of ice. Study areas include emergent wetland and submerged benthic habitats; floating biotic and abiotic materials; water column ecology, water quality and biochemistry properties; and coastline mass flux and dynamics (Turpie et al., 2015a). The nature of the aquatic environment inherently presents additional challenges to retrieving information from the recorded signal. Besides atmospheric effects mentioned in 2.1.1.1, the recorded signal is also affected by glint (Wang and Bailey, 2001; Hochberg et al., 2003; Hedley et al., 2005; Goodman et al., 2008; Kay et al., 2009; Hu, 2011), and bubbles and whitecaps (Frouin et al., 1996; Dierssen, 2019). The necessity to correct for these effects depends on the particular algorithm used to retrieve a data product (Hochberg et al., 2011). Moreover, the added optical complexity of the water column itself often requires the generation of subproducts such as inherent optical properties (Lee et al., 2009) and bathymetry (Lee et al., 1998; Lee et al., 1999; Goodman and Ustin, 2007; Dekker et al., 2011; Thompson et al., 2017b; Barnes et al., 2018; Garcia et al., 2020) as intermediate outputs for retrieval of water column and benthic properties. Spectral techniques can provide characterization of various types of floating algae and other floating matter (Qi et al., 2020), carbon:chlorophyll ratios for kelp (e.g., Bell et al., 2015) or changes in fluorescence yielding satellite-derived estimates of phytoplankton physiology (e.g., Behrenfeld et al., 2009). Imaging spectroscopy, combined with thermal imagery, was recommended for estimating ecological conditions in the water column (Devred et al., 2013). The combination of imaging spectroscopy and thermal imagery can also offer new insight to aquatic processes along the margins of the sea, including the effects of freshwater discharge to benthic ecosystem distribution and composition (Jo et al., 2019). Imaging spectroscopy is also expected to provide useful data for assessment of inland water quality (Dekker and Hestir, 2012), provided the instrument can sufficiently resolve water bodies from surrounding terrain (Hestir et al., 2015), and with reduced uncertainty of targeted spectral data supporting algorithms utilizing in-water and near-surface validation (Guild et al., 2020). Table 3 lists the aquatic subproduct suites with their dependencies and heritage, while Tables 4-10 list the algorithms typically used to derive these subproducts.

Table 2
Examples of algorithms used to produce snow products.

Subproduct	Citations
Light absorbing particles	Painter et al. (2013); Painter et al. (2016); Khan et al. (2017)
Snow albedo	Stamnes et al. (2007); Painter et al. (2013); Painter et al. (2016)
Snow algae abundance	Painter et al. (2001)
Snow algae composition	Khan et al. (2020)
Grain size	Painter et al. (2013); Painter et al. (2016)
Snow cover fraction	Hall et al. (2002); Painter et al. (2003); Metsämäki et al. (2005); Q. Zhang et al. (2020a, 2020b)

2.2.2.1. Water biogeochemistry. Water biogeochemistry (Table 4) and water quality (section 2.2.2.2, Table 5) comprise overlapping areas of application for which differences in visible to near infrared (VNIR) absorption, scattering, and reflectance of water column constituents enable their retrieval. Water biogeochemistry also overlaps with entries under the water column environment (section 2.2.2.5, Table 8). Overlapping spectral features can confound explicit discrimination among some constituents in both categories, necessitating grouping of retrievals of some products (e.g., sediments and organic particulate matter). Note that entries on Tables 4 and 5 are not necessarily mutually exclusive; an important need for the imaging spectroscopy community moving forward is for an agreed upon terminology and set of definitions and an understanding of the overlaps among retrieved parameters.

2.2.2.2. Water quality. In our survey, the term "water quality" refers to

Table 1
Snow products possible from SBG, including their dependencies, requirements for solar zenith angle (SZA; degrees), view zenith angle (VZA; degrees), and heritage.

Products	Dependencies	External	Max SZA	Max VZA	VSWIR	MWIR	TIR	Mission/ Instrument Heritage	Spatial Areas
Snow fraction	Cloud Filter, Reflectance		75	45	X		X	ASO, AVIRIS-C, AVIRIS-NG,	Terrestrial cryosphere
Snow albedo	Cloud filter, HDRF reflectance, TOA radiance, surface temp, snow algae	Snow/sea ice discriminator	75	45	X			ASO, AVIRIS-C, AVIRIS-NG,	Terrestrial cryosphere
Snow/ice surface temperature	Cloud filter, thermal radiance						X	ECOSTRESS	Terrestrial cryosphere
Snow - light absorbing particles	Cloud filter, HDRF corr. Reflectance		75	45	X			ASO, AVIRIS-C, AVIRIS-NG	Terrestrial cryosphere
Snow algae concentration	Cloud filter, HDRF corr. Reflectance		75	45	X			ASO, AVIRIS-C, AVIRIS-NG	Terrestrial cryosphere
Snow grain size	Cloud filter, HDRF corr. Reflectance		75	45	X			ASO, AVIRIS-C, AVIRIS-NG	Terrestrial cryosphere

Table 3
Aquatic products possible from SBG, including their dependencies, requirements for solar zenith angle (SZA; degrees), view zenith angle (VZA; degrees), and heritage.

Product Suites	Dependencies	External Data	Max SZA	Max VZA	VSWIR	MWIR	TIR	Mission/Instrument Heritage	Spatial Areas
Water biogeochemistry	Water Spectral Reflectance	Stratification/species composition/nutrient/ CDOM/salinity/depth	70	60	X			AVIRIS-C, AVIRIS-NG, SeaWIFS, MERIS, (Hyperion) MODIS, PRISM, HICO, HSI,OLCI, Landsat 8/OLI	Global open and coastal oceans, inland lakes, rivers
Water quality	Water Spectral Reflectance	Stratification/species composition/nutrient/ CDOM/salinity/depth	70	60	X		X	AVIRIS-C, AVIRIS-NG, SeaWiFS, HICO, MERIS, MODIS, OLCI, PRISM, HSI, Landsat 8/OLI	Global open and coastal oceans, inland lakes, rivers
Benthic environment	Water Spectral Reflectance, water column environment	Spectral libraries	70	60	X			HICO, Landsat, PRISM, AVIRIS-C, Sentinel-2, WorldView	Coastal ocean
Water surface environment and hazards	Water Spectral Reflectance, Rayleigh-corrected spectral reflectance	Wind, water depth, surface feature spectral libraries	70	60	X			AVIRIS-NG, CASI, DMSC, HICO, HSI,HJ-1 A/B, Landsat, SeaWiFS, MERIS, MODIS, PRISM, QuickBird, Sentinel-2-3, SPOT, WorldView	Global open and coastal oceans, inland lakes
Water column environment	TIR radiance, LST, Water Spectral Reflectance				X		X	HICO, MERIS, MODIS, OLCI, ECOSTRESS	
Water-volcanic	TIR radiance, LST, Water Spectral Reflectance, emissivity	Stratification, species, composition, turbidity, nutrient, salinity, depth	70	60	X		X	AVIRIS-C, AVIRIS-NG, PRISM, HSI, Landsat, MASTER, HyTES, ASTER	Inland lakes and ocean island lakes
Wetlands	Terrestrial Spectral Reflectance		70	60	X			AVIRIS-C, Landsat, Sentinel-2, WorldView	

Table 4
Water biogeochemistry subproducts.

Subproduct	Citations (including, but not limited to)
Dissolved Organic Carbon (DOC)	Mannino et al. (2008); Fichot et al. (2015); Cao et al. (2018); Li et al. (2018)
Particulate Organic Carbon (POC)	Stramski et al. (2008); Mouw et al. (2016); Le et al. (2018)
Particulate Inorganic Carbon (PIC)	Sadeghi et al. (2012); Mitchell et al. (2017)
Suspended particulate matter (SPM)	Nechad et al. (2010); Han et al. (2016); Novoa et al. (2017); Balasubramanian et al. (2020)
Dissolved Organic Matter (DOM)	Dong et al. (2013)
Absorption for SPM and DOM	Dong et al. (2013)
Chromophoric (or colored) Dissolved Organic Matter (CDOM):	
- Spectral CDOM absorption	Mannino et al. (2008); Zhu et al. (2011); Zhu and Yu (2013); Li et al. (2017); Cao et al. (2018); Hooker et al. (2020); Housekeeper et al. (2021)
- CDOM spectral slope	Aurin et al. (2018); Cao et al. (2018)
Phytoplankton net primary production (NPP)	Behrenfeld et al. (2005); Westberry and Behrenfeld (2014); Silsbe et al. (2016); Kahru (2017)
Partial pressure of carbon dioxide (pCO2)	Lohrenz and Cai (2006); Friedrich and Oschlies (2009); Chen et al. (2019)

Table 5
Water quality subproducts.

Subproduct	Citations (including, but not limited to)
Water column constituents (simultaneous retrieval of algal and cyanobacterial pigments, suspended minerals, and pigment degradation products)	Lee et al. (2002); Maritorena et al. (2002); Ortiz et al. (2013); Ali et al. (2014); Lekki et al. (2017); Ortiz et al. (2017); Avouris and Ortiz (2019); Ortiz et al. (2019)
Chlorophyll-a concentration	Gilerson et al. (2010); Gurlin et al. (2011); Matthews (2011); Moses et al. (2012); Odermatt et al. (2012a, 2012b); Pahlevan et al. (2020)
Phytoplankton accessory pigment concentration	Chase et al. (2017); Bracher et al. (2015); Devred et al. (2013); Qi et al. (2014); Wang et al. (2016)
Algal bloom indicators (general), and specifically:	Stumpf (2001); Frolov et al. (2013); Dierssen et al. (2015b); Kudela et al. (2015); Smith and Bernard (2020)
– Noctiluca	Qi et al. (2019a, 2019b); Qi et al. (2020)
– Trichodesmium	Hu et al. (2010); Dupouy et al. (2011); McKinna (2015)
– Karenia sp. Harmful Algal Blooms (red tides)	Hu et al. (2005); Wynne et al. (2005); Craig et al. (2006); Soto et al. (2016)
– High biomass event detection (indicator of eutrophication)	Klemas (2012); Ryan et al. (2014)
– Pseudo-nitzschia	Anderson et al. (2016)
– Floating algae and other floating matters	See Table 8
– Red tide - *Cochlodinium polykrikoides*	Ahn and Shanmugam (2006); Kim et al. (2016)
Algal bloom indicator (common methods):	
– Red Band difference	Amin et al. (2009); Freitas and Dierssen (2019)
– Adaptive reflectance peak height	Ryan et al. (2014); Smith and Bernard (2020)
Phytoplankton spectral classifiers	Bracher et al. (2009); Odermatt et al. (2012a, 2012b); Palacios et al. (2015); Xi et al. (2015)
Spectral CDOM absorption	See Table 4
Dissolved Organic Carbon (DOC)	See Table 4

constituents of the water column that are detectable using imaging spectroscopy and for which some level of value could be assessed (e.g., sediment concentrations due to erosion and runoff or chlorophyll concentrations as a result of eutrophication). Some of the water quality subproducts are reformulations of biogeochemistry (Table 4) or water surface environment (Table 7) subproducts, and can be utilized independent of value judgment as measures of biological composition of the water column habitat (e.g., different pigment concentrations representative of different taxa present).

2.2.2.3. Benthic environment. Benthic habitats include optically shallow ecosystems that reside on the seafloor, such as coral reefs and seagrass. In this domain, the signal at the water surface includes a combination of reflectance from both the benthic surface and the water column (e.g., Maritorena et al., 1994), so algorithms typically resolve this interconnectedness by either simultaneously or sequentially deriving the three

Table 6
Benthic habitat subproducts.

Subproduct	Citations (including, but not limited to)
Benthic visible/NIR spectral reflectance	Lee et al. (1998, 1999); Mobley et al. (2005); Goodman and Ustin (2007); Dekker et al. (2011); Torres-Pérez et al. (2012); Torres-Perez et al. (2015); Thompson et al. (2017b); Barnes et al. (2018); Garcia et al. (2018, 2020)
Benthic cover classification	Lee et al. (1998, 1999); Hochberg and Atkinson (2003); Mobley et al. (2005); Goodman and Ustin (2007); Dekker et al. (2011); Torres-Perez et al. (2015); Asner et al. (2017a, 2017b); Thompson et al. (2017b); Barnes et al. (2018); Garcia et al. (2018, 2020); Li et al. (2019a, 2019b)

Table 7
Water surface environment subproducts.

Subproduct	Citations (including, but not limited to)
FAI (floating algal index) or FVI (floating vegetation index) to identify water surface anomalies	Hu et al. (2009); Dierssen et al. (2015a); Gao and Li (2018)
Floating biota classification	Hu et al. (2015); Qi et al. (2020)
η (% cover) of floating macroalgae	Qi et al. (2016); Wang et al. (2016)
σ (biomass density, g m-2) of floating macroalgae	Hu et al. (2017); Wang et al. (2018)
Flotsam, including micro- and macroplastics	Garaba and Dierssen (2018); Garaba et al. (2018); Biermann et al. (2020); Kikaki et al. (2020)
Floating pumice rafts	Jutzeler et al. (2014); Qi et al. (2020)
Oil type and thickness	Clark et al. (2010); Sun and Hu (2019); Lu et al. (2019, 2020)
Water surface skin temperature	(see Section 2.1.1.2); Minnett et al. (2019)

Table 8
Subproducts for water column environments.

Subproduct	Citations (including, but not limited to)
Inherent and Apparent Optical Properties (IOPs and AOPs such as absorption and scattering coefficients, diffuse attenuation coefficients)	Lee et al. (1999, 2002, 2009); Loisel et al. (2018); Twardowski and Tonizzo (2018); Grunert et al. (2019); Pahlevan et al. (2021)
Bathymetry	Lee et al. (1999, 2010); Dekker et al. (2011); Thompson et al. (2017b)
Salinity	Palacios et al. (2009); Urquhart et al. (2012); Chen and Hu et al. (2017)
Turbidity	Dogliotti et al. (2015); Knaeps et al. (2015)

Table 9
Volcanic and glacier lakes are represented by the following subproducts.

Subproduct	Citations (including, but not limited to)
Volcanic lake color composition	Oppenheimer (1997)
Volcanic and glacier lake temperature	Oppenheimer (1996); Oppenheimer (1997); Trunk and Bernard (2008); Ramsey and Harris (2013); Zhang et al. (2020a)

basic unknowns: water depth, water optical properties, and bottom reflectance. Algorithms typically generate either an indication of proportional benthic composition (e.g., percent coral, sand, algae) or a measure of benthic reflectance to which standard classification methods can be applied.

2.2.2.4. Water surface environment and hazards. Various types of macroalgae can float on the water surface, and some microalgae can also form surface scums (Qi et al., 2020). These include cyanobacterium *Microcystis*, *Trichodesmium*, green *Noctiluca scintillans*, red *Noctiluca scintillans*, *Sargassum fluitans*, *Sargassum natans*, *Sargassum horneri*, *Ulva prolifera*, dead seagrass, and other aquatic plants, which includes several subproducts also listed in Table 5. Surface algae can be detected by VNIR reflectance but can be confounded by surrounding absorbing water optical properties and reflecting water column constituents. Other floating materials such as oil slicks, pumice rafts and water hazards such as flotsam have also been observed from spectral imagery (Hu et al., 2009; Clark et al., 2010; Jutzeler et al., 2014; Lu et al., 2020; Qi et al., 2020). Of particular importance are marine microplastics, macroplastics, and other forms of marine debris, yet due to their small size (relative to an image pixel), remote sensing detection is still at its infancy (Garaba et al., 2018; Biermann et al., 2020; Kikaki et al., 2020).

2.2.2.5. Water column environment. Water column environment refers to physical parameters affecting retrievals from the water column, with turbidity constituting a reformulation of entries in Tables 4 and 5.

2.2.2.6. Water – Volcanic and Glacier Lakes. Volcanic lakes (water lakes) often form in craters even in arid environments and can mask measurement of volcanic gas and ash emissions. Retrievals of turbidity, lake surface temperature, surface composition, albedo, stratification, biotic changes including algal blooms, and other changes of surface compositional characteristics, facilitate inference of volcanic emissions that are otherwise hidden from direct observation.

Glacier lakes are particularly sensitive to climate change and are useful indicators since many are spatially distant from direct anthropogenic influences. The changes in glacier lake surface area and temperature have been linked to regional climate changes and can be used to better understand glacial melting (Zhang et al., 2020a). In addition, surface algae biomass and biodiversity can also be an indicator of environmental and biochemical change (Ghunowa et al., 2019).

2.2.2.7. Wetlands. Remote sensing has been used to map wetland covers and differentiate wetland types for several decades (e.g., Townsend and Walsh, 2001; Simard et al., 2006; Han et al., 2018). Of these, statistical classification approaches are widely used and, as well, spectra-based pixel unmixing has been shown effective in quantifying wetland cover types at sub-pixel scale (Han et al., 2018). Many imaging spectroscopy and thermal imaging techniques used for terrestrial vegetation can be applied to emergent wetlands (Turpie et al., 2015b); however, the presence of water can complicate some methods, including nonlinear spectral mixing with an aquatic substrate affecting red-edge position (Turpie, 2013), the mixing between open water and emergent vegetation spectra suggesting finer spatial resolution, and the combined effect of specular reflectance (glint) and the emergent canopy BRDF (Turpie et al., 2015b). Approaches based on the use of the first or second order derivative of surface reflectance can effectively remove the effect of mild glint in wetlands. In forested wetlands, synergisms with synthetic aperture radar (SAR) can also aid with identification and correction for sub-canopy inundation (Lang et al., 2008; Lamb et al., 2019).

2.2.3. Geology

Over the past four decades, VSWIR imaging spectroscopy has been successfully applied to geologic and mineral deposit studies in well-exposed, mid-latitude areas at local scale (Coulter et al., 2007; Goetz, 2009; van der Meer et al., 2012; Swayze et al., 2014; Cudahy, 2016). VSWIR spectroscopy is key to identifying iron-rich minerals (e.g., goethite, hematite, and jarosite) and hydrous minerals (e.g., micas and clays) and defining mineral distribution patterns that are often products of hydrothermal alteration and which may be indicative of geologic processes and potential for mineral resources (Clark, 1999; Clark et al., 2003). Mineral maps can also be used to assess surface pH and metal leachability of mine waste and the potential of these materials to

Table 10
The geology products possible from SBG, including their dependencies, view zenith angle (VZA) requirements, and heritage (values are not shown where no studies were reported to quantitatively define said limits).

Products	Dependencies	External Data	Max SZA	Max VZA	VSWIR	MWIR	TIR	Mission/ Instrument Heritage	Spatial Areas
Mineralogy (including mixtures)	Terrestrial Spectral Reflectance, Fractional cover, emissivity	Digital Elevation, Spectral libraries			X	X	X	AVIRIS, ASTER, Hyperion, Landsat, HyTES AHS	Global
Naturally occurring asbestos	Terrestrial Spectral Reflectance, Fractional cover	Lithologic and vegetation cover maps			X			AVIRIS-C AVIRIS-NG	Global
Acid mine drainage	Terrestrial Spectral Reflectance	Digital Elevation, spectral libraries			X			AVIRIS-C AVIRIS-NG Hyperion	Global
Soils (texture, organic carbon, water content, clay mineralogy, degradation)	Terrestrial Spectral Reflectance, Fractional cover, emissivity	Elevation, veg communities Spectral libraries			X	X	X	AVIRIS, ASTER, Hyperion, MODIS, Landsat, HyTES AHS	Global
Soil erosion	Terrestrial Spectral Reflectance, Fractional cover, emissivity	Elevation, veg communities Spectral libraries			X	X	X	AVIRIS, ASTER, Hyperion, Landsat.	Global
High-temperature volcanic and wildfire phenomena (thermal anomaly detection, fire and lava temperature and area)	VSWIR and MWIR (~ 4 μm) for high temps, TIR radiance for ambient temps, Terrestrial Spectral Reflectance, emissivity	Historical reflectance/ emissivity, spectral libraries	Night-time observations beneficial for VSWIR-based temperature estimation		X	X	X	AVIRIS, MASTER, HyTES, ASTER, MODIS, VIIRS, Hyperion PRISMA	Global
Volcanic SO_2 and Ash Emissions (volcanic plumes and clouds, SO_2 and ash content, CO_2 plumes)	TIR radiance (7–12 mm) to measure SO_2 and ash absorption/emission, -SWIR to measure aerosol scattering	Surface elevation and emissivity, Plume thickness and altitude, Profiles of atmospheric temperature and water vapor			X		X	MASTER, HyTES, ASTER, MODIS, VIIRS, AIRS, SEVIRI, IASI	Global
Post-Event Monitoring	Terrestrial Spectral Reflectance, emissivity, surface temperature	Historical baseline			X	X	X		

contribute to acid mine drainage (Swayze et al., 2000). While VSWIR data are not effective in identifying rock forming minerals such as quartz, feldspars, and pyroxenes, multispectral TIR data are effective for making discriminations between these minerals (Hubbard et al., 2018). Airborne VSWIR imaging spectrometer and TIR multispectral data have been collected in diverse geologic terranes across the globe and applications have been expanding (Tukiainen and Thomassen, 2010; Bedini, 2012; Kokaly et al., 2013, 2018; Rogge et al., 2014; Black et al., 2016; Laakso et al., 2016; Graham et al., 2018).

2.2.3.1. Mineral mapping. Spectral feature comparison methods, such as Tetracorder (Clark et al., 2003; Swayze et al., 2003) and MICA (Material Identification and Characterization Algorithm; Kokaly, 2011) identify the spectrally dominant mineral(s) in each pixel of a data cube by comparing spectral features in its reflectance spectrum to absorption features in a reference spectral library of minerals. Continuum removal is the technique used to isolate diagnostic absorption features from background spectral variations (Clark and Roush, 1984; Clark, 1999) in both the pixel and reference spectra. Following continuum removal, the coefficient of determination (r^2) of a linear regression of these continuum-removed values is used as the metric to judge the degree of match (or fit) between the two spectra. In addition to identifying mineral components, estimation of mineral fractional abundance using imaging spectroscopy can be made using the spectral feature comparison methods outlined above. These methods produce a relative measure of absorption feature depth that has been interpreted as a proxy for mineral abundance or aerial fraction in a pixel (Clark, 1999; Clark et al., 2003). The EnGeoMAP 2.0 methodology (Mielke et al., 2016) extends the Tetracorder approach and the Processing Routines in IDL for Spectroscopic Measurements (PRISM) approach with the calculation of spatio-spectral gradients and the automated extraction of mineral anomalies according to geologic expert knowledge (Mielke et al., 2016).

Linear mixture analysis has been applied to estimate intimate (e.g., fine scale mixtures including multiple scattering) mixtures of minerals and rocks in lunar samples (Johnson et al., 1985). Multiple scattering and particle size effects result in nonlinear mineral mixtures, but can be linearized by conversion to single scattering albedo using the Hapke (1981) as shown by Johnson et al. (1992) for a series of minerals mixed in the laboratory and particle size mixtures from desert alluvial fans (Shipman and Adams, 1987), where the grain size is known. In validation of spectral unmixing techniques for minerals identification and abundance estimation, Kerekes et al. (2003) demonstrate the effectiveness of unconstrained linear demixing methods in comparison to an end-to-end radiometric transfer model, FASSP.

Rock formations are assemblages of minerals, whose small features may be lost in combination. In cases where small features are suspected, it may be better to compare rock spectra before continuum removal, using standard target detection techniques such as a foreground/background analysis (Smith et al., 1994), spectral matched filter (Stocker, 1990), constrained energy minimization (Farrand and Harsanyi, 1997), or an adaptive cosine estimator (Truslow et al., 2013).

2.2.3.2. Soil characterization. Soil erosion and degradation significantly impact food production and vegetation health (Ben-Dor et al., 2009). These, as well as soil texture, soil organic carbon, soil water content, nutrient content, and a range of other soil applications have strong

potential with imaging spectroscopy (Ben-Dor et al., 2009; Gupta, 2017). While the VSWIR is important for detecting organic components in soil as well as clay mineralogy, the TIR and MWIR range is also sensitive to soil organics (Hbirkou et al., 2012; Kopacková et al., 2017). Soil degradation such as wildfire-induced hydrophobicity (water repellent soils) has been mapped with imaging spectroscopy and spectral unmixing (Finley and Glenn, 2010). Numerous other studies have mapped bare soil properties (e.g., Lagacherie et al., 2008) relevant for agriculture and erosion monitoring. In some cases, strong narrow absorption features of minerals may be detected through significant vegetation cover, for example, Swayze et al. (2009) were able to detect serpentine mineral absorptions despite 80% vegetation cover. However, separating the soil signal from imaging spectrometers can often be complicated by the presence of vegetation or litter cover (including crop residue), soil moisture, or soil surface roughness. Thus, to estimate soil organic carbon, residual spectral unmixing has been used to separate vegetation from soil (Bartholomeus et al., 2011), and a shadow correction factor has been employed to minimize effects of surface roughness (Denis et al., 2014). Likewise, soil texture mapping with imaging spectroscopy was improved using spectral indices for soil moisture corrections (Diek et al., 2019). Multi-temporal approaches (e.g., Diek et al., 2016) may also provide better area-wide soil mapping and are promising in the context of global imaging spectroscopy missions. The effectiveness of multi-temporal radiometric approaches using both VSWIR and TIR data in conjunction with DEM data was demonstrated by Dobos (1998) and Dobos et al. (2000). The Dobos work used AVHRR multispectral data over large regions, but the methods are readily extensible to imaging spectroscopy data. In addition to spectral unmixing approaches, empirical techniques such as partial least squares regression (PLSR, e.g., Bartholomeus et al., 2011) or geostatistical techniques for regional calibration (e.g., Hbirkou et al., 2012) are typically employed in soil characterization studies.

2.2.3.3. High-temperature phenomena. This suite includes algorithms targeting both wildfires and high-temperature volcanic phenomena, such as active/recent lava and pyroclastic flows. High temperature phenomena are characterized by high emitted radiance across the full range of wavelengths (VSWIR, MWIR, and TIR) covered by SBG. High temperature phenomena can be characterized by modeled temperatures, or through the modeled emittance quantity known as Fire Radiative Power (FRP; Wooster et al., 2003) or Volcanic Radiative Power (VRP; Coppola et al., 2013). FRP is essential for understanding biomass burning, combustion efficiency, and emissions (Roberts et al., 2005; Vermote et al., 2009; Kaiser et al., 2012), while lava temperature and VRP are linked to lava effusion and cooling rates (Wright et al., 2010; Coppola et al., 2013). Temperature has been typically retrieved from coarser (kilometer-scale) spatial resolution data using two-source mixing models, which include a hot component representing fire or lava (assumed to be a blackbody emitting at a single temperature) and a background component (Dozier, 1981). Giglio and Kendall (2001) and Lombardo et al. (2012) examined the sensitivity of two-source temperature retrievals to a variety of assumptions for fire and lava, respectively.

An alternative approach for estimating fire or lava temperature is to rely on the magnitude and spectral shape of emitted radiance measured using imaging spectrometer data covering the VSWIR. Each measured pixel spectrum can be fit by a temperature dependent function or by a library of spectra modeled from a range of temperatures (Dennison et al., 2006; Wright et al., 2011). Scaling of this approach from AVIRIS data to SBG spatial resolution has been examined for fire (Matheson and Dennison, 2012), and spectral temperature modeling approaches are extensible to MWIR and TIR channels (Dennison and Matheson, 2011).

FRP and VRP, in contrast, are approximations of emittance integrated over all wavelengths based on the relationship between emittance and radiance for a channel near 4 μm (Wooster et al., 2003). FRP is a standard product for MODIS, VIIRS, Sentinel-3, and even geostationary satellites (Wooster et al., 2012; Wooster et al., 2015; Giglio et al., 2016). SBG 4 μm and TIR channels would allow calculation of FRP/VRP with more spatial detail and facilitate scaling with more frequently available products from coarser resolution sensors. Due to SBG's relatively fine spatial resolution, saturation is a significant concern for measuring fires or lava flows that may compose most of a pixel (Realmuto et al., 2015). Saturation thresholds for 4 μm and TIR channels will have to be carefully considered to enable creation of radiative power products.

2.2.3.4. Volcanic SO_2 and ash emissions. The TIR spectra of sulfur dioxide (SO_2) gas and volcanic ash (pulverized silicate rock) exhibit characteristic features that have long been used to map volcanic plumes and clouds (e.g., Prata, 1989a, 1989b; Realmuto et al., 1994, 1997; Wen and Rose, 1994; Prata and Bernardo, 2007; Prata and Prata, 2012; Realmuto and Berk, 2016; Prata and Lynch, 2019). In most situations, the plumes are detected in transmission, based on the attenuation of radiance passing through the plumes en route to the sensor. The origins of this radiance are the surface and atmosphere beneath the plume and, consequently, our estimations of gas and ash content require knowledge of the surface emissivity, topography, and profiles of atmospheric temperature and water vapor. These parameters initialize models of atmospheric emission and transmission radiative transfer models, which are then employed to estimate surface temperature and plume composition.

2.2.3.5. Atmospheric CH_4 and CO_2 emissions. SWIR channels proposed for SBG are particularly promising for detecting and retrieving concentrations for CH_4 and CO_2 and point source plumes. Individual CH_4 (Thorpe et al., 2014; Frankenberg et al., 2016; Duren et al., 2019) and CO_2 (Dennison et al., 2013; Thorpe et al., 2017) point source plumes have been mapped using airborne spectral imaging with moderate (5–10 nm) spectral resolution and high (1–16 m) spatial resolution. Thompson et al. (2016) mapped plumes from a natural gas well blowout using 10 nm spectral resolution and 30 m spatial resolution Hyperion data. Recent work has explored the potential for extending CH_4 and CO_2 point source imaging and concentration retrieval to the upcoming suite of space-based sensors: PRISMA, EnMAP, EMIT, SBG, and CHIME (Ayasse et al., 2019; Cusworth et al., 2019). Preliminary results from PRISMA observations of strong CO_2 and CH_4 emissions plumes are consistent with the performance estimated by Cusworth et al. (2019).

The OCO-2 atmospheric sounder measures fine spectral channels near 0.765 μm, 1.61 μm, and 2.06 μm. These data have been used to determine CO_2 emitted by active volcanoes (Schwandner et al., 2017; Johnson et al., 2020; Queißer et al., 2019), fires (Heymann et al., 2017), and industrial emissions (Nassar et al., 2017).

CO_2 absorption features in the MWIR region have been less thoroughly investigated, but recent studies have been developed to understand the capability to use the absorption band at 4.8 μm to detect and measure the CO_2 emissions from different point sources at high temperature as degassing from thermal active volcanoes (Romaniello et al., 2020).

2.2.4. Terrestrial vegetation

Imaging spectroscopy (although limited in spatial and temporal extents) has long been promoted for its potential to characterize vegetation with greater detail than multispectral broadband imagery, starting with studies that showed the sensitivity to foliage biochemicals such as lignin and nitrogen (Wessman et al., 1988) and capacity to classify detailed species composition (Martin et al., 1998; Roberts et al., 1998). The potential application of spectroscopic imagery for vegetation characterization grew out of a long and rich literature dating to the 1970s of using near-infrared spectroscopy (NIRS) to measure nutritional status of plant materials (Cotrozzi et al., 2018) and comprehensive reviews of features in plant spectra related to foliar biochemistry by Curran (1989) and Elvidge (1990). Imaging spectroscopy throughout the VSWIR and TIR

has extensive utility for characterizing and monitoring natural (Asner et al., 2017a), agricultural (Berger et al., 2020b) and managed (e.g., grazing lands) ecosystems (Knox et al., 2011), as well as in experimental studies (Z. Wang et al., 2019).

Three main categories of algorithms for optical remote sensing of vegetation are (1) empirical methods that are based on the statistical relationship between full spectrum or a feature derived from spectrum (e.g., vegetation indices, derivatives), and include both parametric and nonparametric methods (often called "data-driven" methods) including machine learning, (2) physical methods based on the concept of radiative transfer models (RTMs), and (3) hybrid methods that combine RTMs, empirical methods, and external models of biological functions (e.g., Penman-Monteith) to take advantage of the fidelity in physical models and flexibility of statistical approaches. Verrelst et al. (2019) provide a comprehensive taxonomy of retrieval methods for vegetation properties from imaging spectroscopy data.

2.2.4.1. Preprocessing and intermediate transformations. Regardless of category, most vegetation retrieval algorithms require corrections for topography and BRDF, which varies with plant canopy architecture and light environment (Painter et al., 2013, 2016; Ustin, 2013; Gatebe and King, 2016; Wang et al., 2017). In particular, the retrieval of nadir BRDF-adjusted reflectance (or NBAR; Schaepman-Strub et al., 2006) is a necessary intermediate step for many vegetation algorithms. For example, models that utilize biophysical properties derived from imaging spectroscopy, such as vegetation albedo, need to minimize angular effects for accurate vegetation parameter estimation (Laurent et al., 2014; Weyermann et al., 2014, 2015). There is a vast literature on methods for BRDF (Wanner et al., 1995; Collings et al., 2010; Colgan et al., 2012; Schlapfer et al., 2015; Weyermann et al., 2015; Jensen et al., 2018) and topographic (Soenen et al., 2005) correction and their practical implementation (Singh et al., 2015). These corrections are necessary to allow for broad application of the algorithms across different plant types, topographic features, and acquisition dates; a full description of preprocessing steps may be found in Serbin and Townsend (2020).

Empirical methods for spectral quantification of vegetation attributes range from physiologically based indices of vegetation function (e.g., NDVI, NIRv, PRI, CCI; Gamon et al., 1992, 2016; Campbell et al., 2013) to statistical classifiers of plant distributions (Ustin and Gamon, 2010; Fassnacht et al., 2016; Meerdink et al., 2019) and predictive models of continuous properties (Asner and Martin, 2015; Serbin et al., 2015; Singh et al., 2015; R. Wang et al., 2019). Continuously measured spectra allow for descriptions of spectral shape which can be related to leaf or canopy characteristics. Of note, these approaches often involve the use of intermediate data transformations to either discriminate fine-detail spectral features (e.g., absorption features associated with a particular biochemical substance at a particular wavelength) or to describe spectral shape. Methods include first and second derivative reflectance (Blackburn, 1998; Campbell et al., 2013), pseudo-absorption (calculated as log(1/(R)), vector normalization (Feilhauer et al., 2010), and continuum removal (normalization of reflectance to local maxima across a spectral segment). For example, spectral feature analysis (SFA) uses continuum removal techniques to quantify characteristics of absorption features in the spectrum (Kokaly, 2011; Campbell et al., 2013; Huemmrich et al., 2017).

The characteristics of vegetation canopy reflectance observed in imaging spectroscopy data are also influenced by internal canopy structural properties, including leaf shape, angle and distribution, larger canopy structure (e.g., crown size, shape, clumping), and background reflectance (e.g., soil, litter layer). These effects can obscure or confound the signal of leaf properties of interest. For empirical methods in particular, the same set of intermediate transformations also can dampen the effect of brightness variations in the data associated with structural differences in the canopy or background reflectance that may be a source of noise (Hall et al., 1990; Elvidge and Chen, 1995; Feilhauer et al., 2010; Singh et al., 2015). Likewise, the directional area scattering factor (DASF) correction of Knyazikhin et al. (2013) uses the concept of recollision probability to reduce canopy-structure effects in imaging spectroscopy data. However, in either case, development of models that capture the larger range of trait and structural complexity can also help to overcome these issues by accounting, empirically, for the various possible drivers of spectral variation (Schweiger, 2020) and allow the algorithm to separate influences on spectral albedo driven by structure from the changes related to the leaf functional trait of interest.

2.2.4.2. Plant functional traits. Plant functional traits, such as pigment and nutrient concentrations, metabolic capacity, and leaf/canopy morphology, may be retrieved from spectral observations at various scales (Serbin and Townsend, 2020). Imaging spectroscopy has been proposed for detecting many traits, and Table 12 provides a subset of traits that have been suggested for SBG, grouped by their functional roles. At the leaf scale, a narrow set of biochemical and morphological traits (especially pigments and water content) can be estimated by inversion of semi-mechanistic, physically based leaf radiative transfer models (RTMs; Di Vittorio, 2009; Shiklomanov et al., 2016; Féret et al., 2017). These approaches are computationally intensive and, at present, not readily implementable for spectroscopic imagery collected at the volumes generated for global-scale mapping such as SBG. Many traits of interest are not in current formulations of RTMs due to, among other considerations, lack of distinctive spectral features, inclusion could dramatically increase model complexity, or simply because the dimensionality of the data is poorly understood before the model run. Finally, RTMs can be limiting due to the ancillary information needed but not available to the models (such as estimates of leaf area index or soil background reflectance). However, the use of RTM emulators (Verrelst et al., 2017) or hybrid machine-learning methods (Berger et al., 2020a) may eventually reduce the computational limitation.

Regression against vegetation indices is commonly used, especially for pigments and other traits with unique spectral absorption features (Gitelson and Solovchenko, 2018), but least squares regression is not normally recommended for traits that are expressed throughout the spectrum due to the potential for spurious correlations (Grossman et al., 1996). More typically, partial least squares regression (PLSR, Wold et al., 2001), a chemometric method that utilizes the original spectral measurements (or transformed spectra), is designed for robust implementation where the number of predictors (spectral channels) relative to observations is high. PLSR methods derive model coefficients, or channel weights, based on a partial least squares regression between spectroscopic measurements and laboratory measurements of various chemical and constitutional traits of the same sample (Serbin et al., 2014). The derived trait estimates can then be linked to imaging spectroscopy datasets for prediction and mapping (Singh et al., 2015). Additional methods gaining traction include Gaussian process regression (Verrelst et al., 2013; Z. Wang et al., 2019), which in comparison to PLSR has the benefit of directly estimating uncertainties, at the cost of higher computational needs and lower direct interpretability.

A very large number of traits are commonly estimated through statistical techniques such as PLSR, most notably leaf mass per area (LMA) and nitrogen concentration (indicators of plant tradeoffs between investment in photosynthesis/growth vs. leaf structure), chlorophyll *a* and other pigments, water and lignin (a structural compound) (Coops et al., 2003; Townsend et al., 2003; Martin et al., 2018; Asner and Martin, 2015; Singh et al., 2015; Wang et al., 2019; 2020). A wider range of plant compounds have also been mapped from imaging spectroscopy, including phenolics (Kokaly et al., 2003) and other plant defensive compounds (Madritch et al., 2014), macronutrients (e.g., Ca, Mg, K), nonstructural carbohydrates (Asner and Martin, 2015) and structural carbohydrates associated with plant growth and defense (Asner et al., 2015; Singh et al., 2015), including in forests (Asner et al., 2015),

grasslands (Z. Wang et al., 2019) and across multiple physiognomic vegetation types (Wang et al., 2020). In addition, recent work has also illustrated the utility of combining passive optical imaging spectroscopy and active lidar for mapping total canopy estimates of nitrogen and LMA (e.g., Chlus et al., 2020; Kamoske et al., 2020).

Imaging spectroscopy has also been used to map physiological traits that are not specific chemical or morphological characteristics of vegetation, but rather can be inferred from the spectra due to correlation with the traits hypothesized to control them. These include light use efficiency (Huemmrich et al., 2019), photosynthetic carboxylation capacity and its temperature sensitivity (Vcmax and Ev; Serbin et al., 2015), and ecosystem production (Campbell et al., 2013; Huemmrich et al., 2017; Dubois et al., 2018). Imaging spectroscopy has been shown to be sensitive to $\delta^{13}C$ and $\delta^{15}N$, measures of isotopic fractionation that are indicators of water and nitrogen availability, respectively (Singh et al., 2015; Wang et al., 2020).

The range of traits and conditions of measurement that have been estimated using leaf level spectral data is much greater than what has been estimated from imaging data (e.g., Serbin et al., 2012, 2019; Couture et al., 2016; Wu et al., 2019), suggesting the need for additional data and research at the image scale to assess the full range of vegetation traits that can be reliably retrieved from SBG-like imagery. Note that traits can be estimated both at the top-of-canopy leaf level or the canopy level and can be measured on an area or mass basis. Different retrievals may have different assumptions about knowledge of canopy biomass or leaf area for accurate retrieval.

While not strictly a trait, we have listed the fraction of Absorbed Photosynthetically Active Radiation (fAPAR) alongside them since this describes the photosynthetic processes by describing the light absorption over an integrated plant canopy, which is directly related to primary productivity (Q. Zhang et al., 2012).

2.2.4.3. Plant species. With sufficient spatial resolution, certain plant species or genera can be mapped directly from the spectral features of grasses (Pottier et al., 2014), herbs, and tree canopies (Baldeck et al., 2015; Fassnacht et al., 2016; Kattenborn et al., 2019). Species mapping has been extended to characterizing communities of mixes of species in a variety of ecosystems including grasslands (Feilhauer et al., 2011; Rossi et al., 2020), bogs/fens (Schmidtlein et al., 2007), temperate (Foster and Townsend, 2004; Gu et al., 2015) and tropical forests (Asner et al., 2017a). Because of the rich spectral information in imaging spectroscopy datasets, endmember analysis is widely used to map both species and communities (Roberts et al., 1998). Other methods use statistical methods such as conditional random forests (Pottier et al., 2014), and biased support vector machines (Baldeck et al., 2015) to map vegetation species. Approaches combining remote sensing and species distribution models are continuously emerging (Randin et al., 2020). While much of the fine spatial resolution airborne vegetation remote sensing has focused on species mapping, at larger spatial extents mapping plant functional types (PFTs; groups of species that are physiologically similar) becomes more feasible, for example, discrimination of C3 and C4 dominated grasslands (Huemmrich et al., 2018) or lianas within tropical forests (Foster et al., 2008; Marvin et al., 2016). Uncertainty in PFT distributions is also a critical source of uncertainty in Earth system models (ESMs) (Wullschleger et al., 2014; Poulter et al., 2015). As Earth system model representations of plant functional groups become more complex (Fisher et al., 2017), more nuanced mapping of PFTs will be essential (Wullschleger et al., 2014). With global coverage of imaging spectroscopy data, SBG will provide input for significant improvements in these models.

2.2.4.4. Diversity. Indicators of spectral diversity derived from airborne and ground-based imaging spectrometers have proven useful in modeling multi-scale taxonomic, phylogenetic, and functional diversity of vegetation (Rocchini et al., 2010; Wang and Gamon, 2019; Cavender-Bares et al., 2020; Thonicke et al., 2020). Measures of diversity derived from imagery provide indirect metrics of diversity, and as such most approaches involve linkage of image-derived metrics to ground-based measures of diversity from field surveys via statistical methods. This points to the necessity of ground metrics to interpret image-derived diversity. There are two basic approaches to diversity mapping using spectroscopic data: (1) diversity metrics based on derived products, such as foliar traits (see 2.4.2.2) (e.g., Schneider et al., 2017; Zheng et al., 2021) or (2) methods based on spectral dissimilarity (e.g., Féret and de Boissieu, 2020). The mapping of taxonomic diversity, which includes species richness and abundance-based diversity measures such as the Shannon index (H′), has been conducted across tropical forested landscapes (Féret and Asner, 2014), North American prairie landscapes (Wang et al., 2016), and regional environmental gradients (Somers et al., 2015). Given the large number of vascular plant species on Earth, there is increasing interest in characterizing functional diversity (e.g., evenness, divergence, richness) as a metric relevant to the prediction of ecosystem processes and taxonomic diversity (Schneider et al., 2017; Durán et al., 2019; Zheng et al., 2021), and as a basis for conservation planning (Asner et al., 2017b). Recent studies have also extended taxonomic diversity mapping to assess genetic and phylogenetic diversity in a variety of experimental settings, including aspen forests (Madritch et al., 2014), temperate forests (Czyz et al., 2020), temperate grasslands (Schweiger et al., 2018), tropical oak forests (Cavender-Bares et al., 2016), and at large scales across several biomes (Meireles et al., 2020).

While the inherent high dimensionality of imaging spectroscopy data enables characterization of multiple metrics of diversity, both species and diversity mapping are sensitive to the size of the organism of interest, and hence the pixel size of imaging. There is an extensive literature examining the sensitivity of spectral diversity to spatial scales and species composition (Wang et al., 2018), sensor characteristics and multi-scale diversity mapping (Hakkenberg et al., 2018), and to validate spectral diversity hypotheses (Dahlin, 2016; Gholizadeh et al., 2019).

2.2.4.5. Evapotranspiration. Evapotranspiration (ET) is a key bioclimatic variable, linking water, energy, and carbon cycles (Fisher et al., 2017). ET is controlled by water (soil moisture, atmospheric moisture), energy (net radiation, temperature), and plants (stomatal conductance, leaf area index, plant habit). As such, ET can be retrieved from space through the combination of observables related to water, energy, and plant canopies. Algorithms to retrieve ET synthesize thermal data to capture energy dynamics and infer water, and spectral data to characterize crown characteristics. Tradeoffs among various models balance spatial and temporal scale of interests, which is particularly important because ET exhibits high diurnal variability. Existing remote sensing models of ET include: Priestley-Taylor Jet Propulsion Laboratory (PT-JPL) (Fisher et al., 2008); Global Land Evaporation Amsterdam Model (GLEAM) (Miralles et al., 2011); Disaggregated Atmosphere Land-Exchange model (DisALEXI) (Anderson et al., 2007); Penman-Monteith Mu (PM-Mu) (Mu et al., 2011); Mapping ET with high Resolution and Internalized Calibration (METRIC) (Allen et al., 2007); Surface Energy Balance System (SEBS) (Su, 2002); and Surface Energy Balance Algorithm over Land (SEBAL) (Bastiaanssen et al., 1998).

For high accuracy, remote sensing algorithms for ET require ancillary datasets to characterize interrelated drivers associated with weather, climate, and especially light availability. Remote sensing algorithms to map ET at large scales are especially sensitive to estimates of net radiation, which is typically derived from radiative, atmospheric and surface data (Fisher et al., 2008, 2009; Jiménez et al., 2011; Polhamus et al., 2013; Badgley et al., 2015). Meteorological data are needed to define microclimates at medium scales (< 5 km) and are essential at high temporal resolution to capture rapidly changing weather (Anderson et al., 1997; Allen et al., 2007; Fisher et al., 2008; Allen et al., 2011). At the field scale (e.g., <100 m), land surface temperature captures fine

spatial dynamics over heterogenous land cover, which is important in the partitioning of energy. At all scales, vegetation dynamics are required and are especially important during rapid vegetation change, such as during green-up, crop harvest and senescence (Anderson et al., 1997; Allen et al., 2007; Fisher et al., 2008; Allen et al., 2011; Polhamus et al., 2013).

ECOSTRESS serves as a precursor to the SBG TIR instrument, acquiring imagery in five channels in the range 8–12 μm from the International Space Station from 2018 to 2021. In combination with ancillary VNIR and meteorological data, it produces standard ET products, and studies have shown that high quality land surface temperature (<1 K) is required for an ET accuracy <10% (Cawse-Nicholson et al., 2020; Fisher et al., 2020).

2.2.4.6. Photo- and non-photosynthetic vegetation characterization (fractional cover). Photosynthetic (green) vegetation can be discriminated from non-photosynthetic vegetation (i.e., senesced foliage as well as wood) primarily through detection of pronounced ligno-cellulose absorption features in the SWIR that are absent from soils (Roberts et al., 1998; Nagler et al., 2000; Daughtry et al., 2006; Guerschman et al., 2009; Dennison et al., 2019). Spectral fitting, mixture models, and spectral vegetation indices (for a review see Dennison et al., 2019) have been developed that facilitate accurate discrimination between crop residues and bare soil surfaces, better capturing differing agricultural practices, and carbon balance in agricultural landscapes (Daughtry et al., 2006). The ratio of non-photosynthetic vegetation to soil is also an important indicator of pasture quality in grazed landscapes in the tropics (Numata et al., 2008).

2.2.4.7. Temporal unmixing. Different vegetation types display distinct temporal patterns as a function of photoperiod, season length, landscape, and spatiotemporal characterization (Sousa and Davis, 2020). The dense time series of multispectral instruments such as MODIS, Landsat, and Sentinel have enabled the characterization and subpixel unmixing of vegetation types using temporal signatures (Lobell and Asner, 2004; Ozdogan, 2010; Sousa and Davis, 2020; Garonna et al., 2016). With the advances of SBG, a regular time series of spectroscopic information will enable similar analysis in both the spectral and temporal domain, as well as combining simultaneous effects of the Earth system (e.g., snow and vegetation; Xie et al., 2018), previously treated separately. Chlus et al. (2019) have demonstrated relationships between environmental variables and spatiotemporal patterns in foliar traits derived from airborne spectroscopic data.

3. Caveats and considerations

A global suite of imaging spectroscopy and thermal imagery is needed to fully understand the composition, functioning, and health of ecosystems, including snow, volcanoes, aquatic environments, and terrestrial vegetation. In combination with active instruments, such as lidar and synthetic aperture radar, as well as passive radar and a range of multispectral data with high temporal or spatial resolution and long measurement legacies, the SBG mission will be an essential component of a multi-sensor system to fully characterize composition and structure of the Earth's surface as well as the processes driving changes at the Earth's surface. Future work is needed to optimally combine structural data from anticipated concurrent active sensors—such as NISAR, ROSE-L, BIOMASS, and the Surface Deformation and Change (SDC) Designated Observable—with SBG products such as vegetation chemistry, composition, and functional traits. The combination of products capturing coincident structure, function, and composition will enable an improved understanding of global ecosystems but will require algorithms that use both active and passive observations.

In addition, other spectrometers and thermal radiometers may overlap with the SBG mission lifetime, including the European Space Agency's (ESA) Copernicus Hyperspectral Imaging Mission (CHIME; Nieke and Rast, 2019) and Land Surface Temperature Monitoring (LSTM; Koetz et al., 2019), and the joint French and Indian Space Agencies' Thermal InfraRed Imaging Satellite for High-resolution Natural resource Assessment (TRISHNA; Lagouarde et al., 2019), as well as multispectral instruments such as Landsat and Sentinel-2. The global Harmonized Landsat Sentinel-2 (HLS) dataset (Claverie et al., 2018) provides a significant improvement in revisit time—2-3 days for HLS compared to 16 days for Landsat—which will be significant for hazard monitoring and agricultural applications, and illustrates the benefit of harmonized datasets. Similarly, harmonization of CHIME and SBG-VSWIR could reduce the revisit period from 16 to 21 days to ~8 days while harmonization of LSTM, TRISHNA, and SBG-TIR could result in daily or sub-daily global revisits. The HLS workflow has to account for differences in solar and view geometry, as well as small differences in spectral bands, and the harmonization has to be done at radiance level. Coordination between missions during development will enable the implementation of complementary atmospheric, BRDF, solar zenith angle, and other corrections, and thus rapid harmonization of higher-level products such as a subset of products drawn from Tables 1-12. A proposed 16-day revisit for the SBG VSWIR could realistically return only one cloud-free observation per month, or significantly fewer in cloudy regions (Schimel et al., 2020), and harmonization with other instruments will enable increased revisit and improved science return.

Scientists requiring hyperspectral spectroscopic data have typically relied on airborne data, and as a result we have large gaps in spatial coverage and limited capability to monitor changes over time (Schimel et al., 2020). A global mission such as SBG will produce large data volumes, and higher-level products encompassed by some of the algorithms presented here will be needed to disseminate relevant information to users. To that end, existing research code will need to be transferred to a robust processing workflow that will require algorithms that are many orders of magnitude faster than the current state of the art. This will likely require emulators or other forms of machine learning, and the accuracy and uncertainty of these compared to the physical or other foundational models need to be well quantified. While the community requires low-latency data processing, the data processing pipelines will also need to plan for simultaneous reprocessing to account for algorithm improvements and updates.

Despite the large overall data volumes, a 30 m pixel in the VSWIR and 60 m pixel in the TIR is several times larger than some of the features of importance to this mission. For example, individual tree crowns are generally much smaller than 30 m in breadth, and, as such, algorithms designed for high-resolution airborne data may no longer be applicable (Schimel et al., 2020). The algorithms that are to be developed and applied to SBG data will certainly start from the legacies of existing algorithms but will likely need to be adapted to accommodate differences that arise from spaceborne acquisitions that are global in scope. A globally applicable algorithm must be free from geographic or latitudinal bias and provide rigorous uncertainty quantification. This will require global calibration and validation. Certain region-specific algorithms may be more accurate than a globally optimized product, but a global product will enable information to be transferred to community members without the technical ability to implement specialized algorithms. SBG should provide a flexible processing system that (1) allows users to interact with the workflow at any stage, (2) allows researchers to test alternative approaches, and (3) accommodates users from all levels of technical expertise.

Users in various communities need to become accustomed to SBG-scale data products and develop the tools to manipulate and analyze them efficiently. Early distribution of SBG-like products will accelerate community readiness to enable early exploitation of SBG data for science and applications as well as to provide critical feedback to the Algorithms Working Group on limitations of the products. Existing instruments such as DESIS, HISUI, EnMAP, EMIT, PACE, GLIMMR, and ECOSTRESS should be used as pathfinders and to establish the time series that will

Table 11
Categories of algorithms for SBG measurements of vegetation.

Products	Dependencies	External Data	Max SZA	Max VZA	VSWIR	MWIR	TIR	Mission/ Instrument Heritage	Spatial Areas
Vegetation Albedo	BRDF-corrected reflectance				X			AVIRIS/NEON/ EO-1 Hyperion	Global
Evapotranspiration	LST, emissivity, NDVI, LAI, Landcover, Albedo	Meteorological			X		X	ECOSTRESS	Global
Plant functional traits	BRDF-corrected reflectance, topographic correction	PLSR coefficients, spectral libraries for RTMs, vegetation indices			X			AVIRIS/NEON/ GAO, EO-1 Hyperion	Temperate US, Europe, Arctic, Tropics
Vegetation species and communities, fractional cover	BRDF-corrected reflectance, topographic correction, plant functional traits	Biome stratification, spectral libraries			X			EO-1 Hyperion, AVIRIS/GAO PRISMA	Globally distributed localized studies
Diversity	[as above]				X			AVIRIS/GAO/ Apex	[as above]
fAPAR	Terrestrial Spectral Reflectance	RTM, spectral libraries			X			AVIRIS [HyspIRI]	Global

Table 12
Categories of plant functional traits potentially detectable from imaging spectroscopy (see text for references and methods).

Category	Example Traits
Photosynthetic processes and carbon uptake	Pigments (chlorophyll a and b, carotenoids, anthocyanins), nitrogen, phosphorus, leaf mass per area (LMA), water (equivalent water thickness and concentration), carbon, nonstructural carbohydrates (sugars, starches), fAPAR
Leaf structural compounds	Cellulose, fiber, lignin, hemicellulose
Defensive compounds	Phenols, condensed tannins
Macronutrients (multiple functions)	Ca, B, Fe, K, Mg, S
Metabolic traits (typically inferred)	$\delta^{13}C$, $\delta^{15}N$ (isotopic ratios, measures of water (^{13}C) and nitrogen (^{15}N) availability, Vcmax, Ev, Jmax (measures of photosynthetic capacity), light use efficiency
Productivity	Gross primary and/or ecosystem production (GPP)

allow SBG to address issues of decadal scale change.

Despite these constraints, SBG will offer an unprecedented dataset for the understanding of the Earth's surface, biology, and geology.

4. Discussion

We have compiled a list of algorithms developed by researchers specializing in VSWIR hyperspectral and multispectral thermal IR imagery that address the SBG core product needs. These algorithms vary in their maturity, including the geographic scope, the range of viewing conditions and sensor characteristics under which they work well. Following a survey of the maturity of the algorithms and their responsiveness to science questions listed as "most" and "very" important in the Decadal Survey, the SBG Algorithm team will recommend a subset of algorithms to operationalize. This will be subject to technical review and done in consultation with the community experts as the SBG mission develops. Given the number of potential algorithms for SBG—including the Level 1B (orthorectified radiance), Level 2 (reflectance, emissivity, and surface temperature), Level 2+ (L2 products corrected for view and solar geometry and other effects), Levels 3 and 4 (many of which are discussed in this manuscript), applications-specific products, and the range of potential higher-level algorithms identified by the community—SBG will likely have to consider on-demand processing in order to generate products of interest to the user community. This will be necessitated by the large data volume of SBG, and additional considerations, such as the availability of multiple plausible algorithms for many of the desired specific products.

In addition, almost all of the proposed algorithms depend on atmospheric corrections, and many require additional processing (such as HRDF or BRDF corrections) that have implicit assumptions and involve model fitting. SBG will require an adequate characterization of correction uncertainties to characterize derived and higher-level product uncertainties (via error propagation), a practice that is currently not common, but which will be vital for downstream users of the data.

Prior to the anticipated launch of SBG, there will be an intensive effort by the SBG Algorithm Team to further mature and operationalize several of the algorithms outlined in this review and their supporting workflows. A full description of the operational concept for SBG products is premature and beyond the scope of this paper, but a full end-to-end data system is envisioned, with accompanying calibration and validation in addition to the proposed product generation and uncertainty quantification.

5. Conclusions

We have summarized the state-of-the-practice algorithms for a range of products that will answer the very important and most important science questions assigned to SBG in the Decadal Survey (NASEM, 2018):

- "How is the water cycle changing? Are changes in evapotranspiration and precipitation accelerating, with greater rates of evapotranspiration and thereby precipitation, and how are these changes expressed in the space-time distribution of rainfall, snowfall, evapotranspiration, and the frequency and magnitude of extremes such as droughts and floods?";
- "How do anthropogenic changes in climate, land use, water use, and water storage, interact and modify the water and energy cycles locally, regionally and globally and what are the short- and long-term consequences?";
- "How does the water cycle interact with other Earth system processes to change the predictability and impacts of hazardous events and hazard chains (e.g., floods, wildfires, landslides, coastal loss, subsidence, droughts, human health, and ecosystem health), and how do we improve preparedness and mitigation of water-related extreme events?";
- "How do spatial variations in surface characteristics (influencing ocean and atmospheric dynamics, thermal inertia, and water) modify transfer between domains (air, ocean, land, cryosphere) and thereby influence weather and air quality?";
- "What are the structure, function, and biodiversity of Earth's ecosystems, and how and why are they changing in time and space?";
- "What are the fluxes (of carbon, water, nutrients, and energy) between ecosystems and the atmosphere, the ocean, and the solid Earth, and how and why are they changing?";

- "What are the fluxes (of carbon, water, nutrients, and energy) within ecosystems, and how and why are they changing?";
- "How large are the variations in the global carbon cycle and what are the associated climate and ecosystem impacts in the context of past and projected anthropogenic carbon emissions?";
- "How can large-scale geological hazards be accurately forecast in a socially relevant time frame?"; and
- "How do geological disasters directly impact the earth system and society following an event?".

This effort has involved the synthesis of the findings of more than 130 scientists. While the list is comprehensive, it is not complete. However, it provides a framework for additional algorithm development and maturation activities in the lead up to the SBG and other planned global missions such as ESA's CHIME and LSTM and the French-Indian multispectral and multi-band thermal mission, TRISHNA.

Declaration of Competing Interest

The authors declare that they have no known competing financial interests or personal relationships that could have appeared to influence the work reported in this paper.

Acknowledgements

Support to the lead authors (Cawse-Nicholson and Townsend) was provided by NASA Headquarters and the Jet Propulsion Laboratory, California Institute of Technology. This study was also supported by the Space-based Imaging Spectroscopy and Thermal (SISTER) pathfinder, part of the Surface Biology and Geology (SBG) project, a NASA Earth Science Designated Observable. Adam Erickson's contribution was supported by an appointment to the NASA Postdoctoral Program at NASA Goddard Space Flight Center, administered by Universities Space Research Association under contract with NASA. Robert Frouin was supported by NASA's Ocean Biology and Biogeochemistry Program under various grants. The contribution of Michael E. Schaepman is supported by the University of Zurich Research Priority Programme on Global Change and Biodiversity (URPP GCB). Shawn Serbin was supported by the Next-Generation Ecosystem Experiments in the Arctic (NGEE-Arctic) and tropics (NGEE-Tropics) that are supported by the Office of Biological and Environmental Research in the Department of Energy, Office of Science, and through the U.S. DOE contract No. DE-SC0012704 to Brookhaven National Laboratory. The authors thank the other members of the SBG Algorithms Working Group, constituting more than 130 researchers, who participated in telecons and webinars to contribute to the contents of this paper. Two anonymous reviewers provided invaluable insight and recommendations, and we are grateful for their time and suggestions. Part of the research described in this paper was carried out at the Jet Propulsion Laboratory, California Institute of Technology, under contract with the National Aeronautics and Space Administration. © 2021 California Institute of Technology. Government sponsorship is acknowledged.

References

Ahmad, Z., McClain, C.R., Herman, J.R., Franz, B.A., Kwiatkowska, E.J., Robinson, W.D., Bucsela, E.J., Tzortziou, M., 2007. Atmospheric correction for NO2 absorption in retrieving water-leaving reflectance from the SeaWiFS and MODIS measurements. Appl. Opt. 46, 6504–6512. https://doi.org/10.1364/AO.46.006504.

Ahn, Y.-H., Shanmugam, P., 2006. Detecting the red tide algal blooms from satellite ocean color observations in optically complex Northeast-Asia coastal waters. Remote Sens. Environ. 103 (4), 419–437. https://doi.org/10.1016/j.rse.2006.04.007.

Ali, K.A., Witter, D.L., Ortiz, J.D., 2014. Multivariate approach to estimate colour producing agents in case 2 waters using first-derivative spectrophotometer data. Geocarto International 29 (2), 102–127. https://doi.org/10.1080/10106049.2012.743601.

Allen, R.G., Tasumi, M., Trezza, R., 2007. Satellite-based energy balance for mapping evapotranspiration with internalized calibration (METRIC)-model. J. Irrig. Drain. E. 133, 380–394. https://doi.org/10.1061/(ASCE)0733-9437(2007)133:4(380).

Allen, R.G., Pereira, L.S., Howell, T.A., Jensen, M.E., 2011. Evapotranspiration information reporting: I. factors governing measurement accuracy. Agric. Water Manag. 98 (6), 899–920. https://doi.org/10.1016/j.agwat.2010.12.015.

Amin, R., Zhou, J., Gilerson, A., Gross, B., Moshary, F., Ahmed, S., 2009. Novel optical techniques for detecting and classifying toxic dinoflagellate Karenia brevis blooms using satellite imagery. Opt. Express 17, 9126–9144. https://doi.org/10.1364/OE.17.009126.

Anderson, M.C., Norman, J.M., Diak, G.R., Kustas, W.P., Mecikalski, J.R., 1997. A two-source time-integrated model for estimating surface fluxes using thermal infrared remote sensing. Remote Sens. Environ. 60 (2), 195–216. https://doi.org/10.1016/S0034-4257(96)00215-5.

Anderson, M.C., Norman, J.M., Mecikalski, J.R., Otkin, J.A., Kustas, W.P., 2007. A climatological study of evapotranspiration and moisture stress across the continental United States based on thermal remote sensing: 1 Model formulation. J. Geophys. Res. Atmos. 112, 1–17. https://doi.org/10.1029/2006JD007506.

Anderson, C.R., Kudela, R.M., Kahru, M., Chao, Y., Rosenfeld, L.K., Bahr, F.L., Anderson, D.M., Norris, T.A., 2016. Initial skill assessment of the California harmful algae risk mapping (C-HARM) system. Harmful Algae 59, 1–18. https://doi.org/10.1016/j.hal.2016.08.006.

Asner, G.P., Heidebrecht, K.B., 2002. Spectral unmixing of vegetation, soil and dry carbon cover in arid regions: comparing multispectral and hyperspectral observations. Int. J. Remote Sens. 23, 3939–3958. https://doi.org/10.1080/01431160110115960.

Asner, G.P., Martin, R.E., 2015. Spectroscopic remote sensing of non-structural carbohydrates in forest canopies. Remote Sens. 7, 3526–3547. https://doi.org/10.3390/rs70403526.

Asner, G.P., Knapp, D.E., Broadbent, E.N., Oliveira, P.J.C., Keller, M., Silva, J.N.M., 2005. Selective logging in the Brazilian Amazon. Science 310, 480–482. https://doi.org/10.1126/science.1118051.

Asner, G.P., Knapp, D.E., Balaji, A., Paez-Acosta, G., 2009. Automated mapping of tropical deforestation and forest degradation: CLASlite. J. Appl. Remote. Sens. 3, 033543 https://doi.org/10.1117/1.3223675.

Asner, G.P., Martin, R.E., Anderson, C.B., Knapp, D.E., 2015. Quantifying forest canopy traits: imaging spectroscopy versus field survey. Remote Sens. Environ. 158, 15–27. https://doi.org/10.1016/j.rse.2014.11.011.

Asner, G.P., Martin, R.E., Knapp, D.E., Tupayachi, R., Anderson, C.B., Sinca, F., Vaughn, N.R., Llactayo, W., 2017a. Airborne laser-guided imaging spectroscopy to map forest trait diversity and guide conservation. Science 355 (6323), 385–389. https://doi.org/10.1126/science.aaj1987.

Asner, G.P., Martin, R.E., Mascaro, J., 2017b. Coral reef atoll assessment in the South China Sea using Planet Dove satellites. Remote Sens. Ecol. Conserv. 3 (2), 1–9. https://doi.org/10.1002/rse2.42.

Aurin, D., Mannino, A., Lary, D.J., 2018. Remote sensing of CDOM, CDOM spectral slope, and dissolved organic carbon in the global ocean. Appl. Sci. 8 (12), 2687. https://doi.org/10.3390/app8122687.

Avouris, D.M., Ortiz, J.D., 2019. Validation of 2015 Lake Erie MODIS image spectral decomposition using visible derivative spectroscopy and field campaign data. J. Great Lakes Res. 45 (3), 466–479. https://doi.org/10.1016/j.jglr.2019.02.005.

Ayasse, A.K., Dennison, P.E., Foote, M., Thorpe, A.K., Joshi, S., Green, R.O., Duren, R.M., Thompson, D.R., Roberts, D.A., 2019. Methane mapping with future satellite imaging spectrometers. Remote Sens. 11 (24), 3054. https://doi.org/10.3390/rs11243054.

Badgley, G., Fisher, J.B., Jimenez, C., Tu, K.P., Vinukollu, R.K., 2015. On uncertainty in global evapotranspiration estimates from choice of input forcing datasets. J. Hydrometeorol. 16 (4), 1449–1455. https://doi.org/10.1175/JHM-D-14-0040.1.

Balasubramanian, S.V., Pahlevan, N., Smith, B., Binding, C., Schalles, J., Loisel, H., Gurlin, D., Greb, S., Alikas, K., Randla, M., 2020. Robust algorithm for estimating total suspended solids (TSS) in inland and nearshore coastal waters. Remote Sens. Environ. 111768. https://doi.org/10.1016/j.rse.2020.111768.

Baldeck, C.A., Asner, G.P., Martin, R.E., Anderson, C.B., Knapp, D.E., et al., 2015. Operational tree species mapping in a diverse tropical forest with airborne imaging spectroscopy. PLoS One 10, 1–21. https://doi.org/10.1371/journal.pone.0118403.

Bandeen, W.R., Hanel, R.A., Licht, J., Stampfl, R.A., Stroud, W.G., 1961. Infrared and reflected solar radiation measurements from the TIROS II meteorological satellite. J. Geophys. Res. 66 (10), 3169–3185. https://doi.org/10.1029/JZ066i010p03169.

Barnes, B.B., Garcia, R., Hu, C., Lee, Z., 2018. Multi-band spectral matching inversion algorithm to derive water column properties in optically shallow waters: an optimization of parameterization. Remote Sens. Environ. 204, 424–438. https://doi.org/10.1016/j.rse.2017.10.013.

Bartholomeus, H., Kooistra, L., Stevens, A., van Leeuwen, M., van Wesemael, B., Ben-Dor, E., Tychon, B., 2011. Soil organic carbon mapping of partially vegetated agricultural fields with imaging spectroscopy. Int. J. Appl. Earth Obs. Geoinf. 13 (2011), 81–88. https://doi.org/10.1016/j.jag.2010.06.009.

Bastiaanssen, W.G.M., Menenti, M., Feddes, R.A., Holtslag, A.A.M., 1998. A remote sensing energy balance algorithm for land, SEBAL: 1 Formulation. J. Hydrol. 212–213, 198–212. https://doi.org/10.1016/S0022-1694(98)00253-4.

Becker, F., Li, Z.L., 1990. Temperature-independent spectral indexes in thermal infrared bands. Remote Sens. Environ. 32, 17–33. https://doi.org/10.1016/0034-4257(90)90095-4.

Bedini, E., 2012. Mapping alteration minerals at Malmbjerg molybdenum deposit, central East Greenland, by Kohonen self-organizing maps and matched filter analysis of HyMap data. Int. J. Remote Sens. 33, 939–961. https://doi.org/10.1080/01431161.2010.542202.

Behrenfeld, M.J., Boss, E., Siegel, D.A., Shea, D.M., 2005. Carbon-Based Ocean productivity and phytoplankton physiology from space. Glob. Biogeochem. Cycles 19, 1. https://doi.org/10.1029/2004GB002299.

Behrenfeld, M.J., Westberry, T.K., Boss, E.S., O'Malley, R.T., Siegel, D.A., Wiggert, J.D., Franz, B.A., McClain, C.R., Feldman, G.C., Doney, S.C., Moore, J.K., 2009. Satellite-detected fluorescence reveals global physiology of ocean phytoplankton. Biogeosciences 6, 779–794. https://doi.org/10.5194/bg-6-779-2009.

Bell, T.W., Cavanaugh, K.C., Siegel, D.A., 2015. Remote monitoring of giant kelp biomass and physiological condition: an evaluation of the potential for the hyperspectral infrared imager (HyspIRI) mission. Remote Sens. Environ. 167, 218–228. https://doi.org/10.1016/j.rse.2015.05.003.

Ben-Dor, E., Chabrillat, S., Demattê, J.A.M., Taylor, G.R., Hill, J., Whiting, M.L., Sommer, S., 2009. Using imaging spectroscopy to study soil properties. Remote Sens. Environ. 113, S38–S55. https://doi.org/10.1016/j.rse.2008.09.019.

Berger, K., Verrelst, J., Féret, J.B., Hank, T., Wocher, M., Mauser, W., Camps-Valls, G., 2020a. Retrieval of aboveground crop nitrogen content with a hybrid machine learning method. Int. J. Appl. Earth Obs. Geoinf. 92 (10217), 4. https://doi.org/10.1016/j.jag.2020.102174.

Berger, K., Verrelst, J., Feret, J.-B., Wang, Z., Wocher, M., Strathmann, M., Danner, M., Mauser, W., Hank, T., 2020b. Crop nitrogen monitoring: recent progress and principal developments in the context of imaging spectroscopy missions. Remote Sens. Environ. 242 (11175), 8. https://doi.org/10.1016/j.rse.2020.111758.

Berk, A.G.P., Anderson, L.S., Bernstein, P.K., Acharya, H., Dothe, M.W., et al., 1999. MODTRAN4 radiative transfer modeling for atmospheric correction. SPIE Proceeding Optical Spectroscopic Techniques and Instrumentation for Atmospheric and Space Research III 3756. https://doi.org/10.1117/12.366388.

Biermann, L., Clewley, D., Martinez-Vicente, V., Topouzelis, K., 2020. Finding plastic patches in coastal waters using optical satellite data. Sci. Rep. 10, 5364. https://doi.org/10.1038/s41598-020-62298-z.

Binding, C., Greenberg, T., McCullough, G., Watson, S., Page, E., 2018. An analysis of satellite-derived chlorophyll and algal bloom indices on Lake Winnipeg. J. Great Lakes Res. 44, 436–446. https://doi.org/10.1016/j.jglr.2018.04.001.

Black, M., Riley, T.R., Ferrier, G., Fleming, A.H., Fretwell, P.T., 2016. Automated lithological mapping using airborne hyperspectral thermal infrared data: A case study from Anchorage Island, Antarctica. Remote Sens. Environ. 176, 225–241. https://doi.org/10.1016/j.rse.2016.01.022.

Blackburn, G.A., 1998. Spectral indices for estimating photosynthetic pigment concentrations: A test using senescent tree leaves. Int. J. Remote Sens. 19 (4), 657–675. https://doi.org/10.1080/014311698215919.

Bracher, A., Vountas, M., Dinter, T., Burrows, J.P., Rottgers, R., Peeken, I., 2009. Quantitative observation of cyanobacteria and diatoms from space using PhytoDOAS on SCIAMACHY data. Biogeosciences 6 (5), 751–764. https://doi.org/10.5194/bg-6-751-2009.

Bracher, A., Taylor, M.H., Taylor, B., Dinter, T., Rottgers, R., Steinmetz, F., 2015. Using empirical orthogonal functions derived from remote-sensing reflectance for the prediction of phytoplankton pigment concentrations. Ocean Sci. 11 (1), 139–158. https://doi.org/10.5194/os-11-139-2015.

Campbell, P.K.E., Middleton, E.M., Thome, K.J., Kokaly, R.F., Huemmrich, K.F., Lagomasino, D., Novick, K.A., Brunsell, N.A., 2013. EO-1 Hyperion reflectance time series at calibration and validation sites: stability and sensitivity to seasonal dynamics. IEEE J. Selected Top. Appl. Earth Observat. Remote Sens. 6 (2), 276–290. https://doi.org/10.1109/JSTARS.2013.2246139.

Cao, F., Tzortziou, M., Hu, C., Mannino, A., Fichot, C., Del Vecchio, R., Najjar, R., Novak, M., 2018. Remote sensing retrievals of colored dissolved organic matter and dissolved organic carbon dynamics in north American eutrophic estuaries and their margins. Remote Sens. Environ. 205, 151–165. https://doi.org/10.1016/j.rse.2017.11.014.

Cavender-Bares, J., Meireles, J.E., Couture, J.J., Kaproth, M.A., Kingdon, C.C., et al., 2016. Associations of leaf spectra with genetic and phylogenetic variation in oaks: Prospects for remote detection of biodiversity. Remote Sens. 8, 1–17. https://doi.org/10.3390/rs8030221.

Cavender-Bares, J., Gamon, J.A., Townsend, P.A., 2020. Remote Sensing of Plant Biodiversity. https://doi.org/10.1007/978-3-030-33157-3.

Cawse-Nicholson, K., Hook, S.J., Miller, C.E., Thompson, D.R., 2019. Intrinsic dimensionality in combined visible to thermal infrared imagery. IEEE J. Selected Top. Appl. Earth Observat. Remote Sens. 12 (12), 4977–4984. https://doi.org/10.1109/JSTARS.2019.2938883.

Cawse-Nicholson, K., Braverman, A., Kang, E.L., Li, M., Johnson, M., Halverson, G., Anderson, M., Hain, C., Gunson, M., Hook, S., 2020. Sensitivity and uncertainty quantification for the ECOSTRESS evapotranspiration algorithm—DisALEXI. Int. J. Appl. Earth Obs. Geoinf. 89, 10208 https://doi.org/10.1016/j.jag.2020.102088.

Chase, A.P., Boss, E., Cetinić, I., Slade, W., 2017. Estimation of phytoplankton accessory pigments from hyperspectral reflectance spectra: toward a global algorithm. J. Geophys. Res. Oceans 122, 9725–9743. https://doi.org/10.1002/2017JC012859.

Chen, S., Hu, C., Barnes, B.B., Wanninkhof, R., Cai, W.-J., Barbero, L., Pierrot, D., 2019. A machine learning approach to estimate surface ocean pCO2 from satellite measurements. Remote Sens. Environ. 228, 203–226. https://doi.org/10.1016/j.rse.2019.04.019.

Chlus, A., Singh, A., Kruger, E.L., Townsend, P.A., 2019. Patterns and drivers of interannual variation in canopy biochemistry: An analysis of the 27-year record of imaging spectroscopy data over Blackhawk Island, WI (1992–2019). In: American Geophysical Union, Fall Meeting.

Chlus, A., Kruger, E.L., Townsend, P.A., 2020. Mapping three-dimensional variation in leaf mass per area with imaging spectroscopy and lidar in a temperate broadleaf forest. Remote Sens. Environ. 250 (11204) https://doi.org/10.1016/j.rse.2020.112043.

Chomko, R.M., Gordon, H.R., Maritorena, S., Siegel, D.A., 2003. Simultaneous retrieval of oceanic and atmospheric parameters for ocean color imagery by spectral optimization: A validation. Remote Sens. Environ. 84, 208–220. https://doi.org/10.1016/S0034-4257(02)00108-6.

Chuvieco, E., 2020. Fundamentals of Satellite Remote Sensing: An Environmental Approach, Third edition. CRC Press.

Clark, R.N., 1999. Chapter 1 spectroscopy of rocks and minerals, and principles of spectroscopy. In: Rencz, A. (Ed.), Manual of remote sensing, Volume 3, Remote Sensing for the Earth Sciences, 3rd ed. John Wiley and Sons, pp. 3–58.

Clark, R.N., Roush, T.L., 1984. Reflectance spectroscopy: quantitative analysis techniques for remote sensing applications. J. Geophys. Res. Solid Earth 89 (B7), 6329–6340. JB089iB07p06329.

Clark, R.N., Swayze, G.A., Livo, K.E., Kokaly, R.F., Sutley, S.J., Dalton, J.B., McDougal, R. R., Gent, C.A., 2003. Imaging spectroscopy: earth and planetary remote sensing with the USGS Tetracorder and expert systems. J. Geophys. Res. 108 (E12), 5131. https://doi.org/10.1029/2002JE001847.

Clark, R.N., Swayze, G.A., Leifer, I., Livo, K.E., Kokaly, R., Hoefen, T., Lundeen, S., Eastwood, M., Green, R.O., Pearson, N., Sarture, C., McCubbin, I., Roberts, D., Bradley, E., Steele, D., Ryan, T., Dominguez, R., the Airborne Visible/Infrared Imaging Spectrometer (AVIRIS) Team, 2010. A method for quantitative mapping of thick oil spills using imaging spectroscopy. U.S. Geol. Sur. Open-File Rep. 51, 1167. http://pubs.usgs.gov/of/2010/1167/.

Claverie, M., Ju, J., Masek, J.G., Dungan, J.L., Vermote, E.F., Roger, J.C., Skakun, S.V., Justice, C., 2018. The harmonized landsat and sentinel-2 surface reflectance data set. Remote Sens. Environ. 219, 145–161. https://doi.org/10.1016/j.rse.2018.09.002.

Colgan, M.S., Baldeck, C.A., Feret, J.B., Asner, G.P., 2012. Mapping savanna tree species at ecosystem scales using support vector machine classification and BRDF correction on airborne hyperspectral and LiDAR data. Remote Sens. 4 (11), 3462–3480. https://doi.org/10.3390/rs4113462.

Coll, C., Caselles, V., 1997. A split-window algorithm for land surface temperature from advanced very high resolution radiometer data: validation and algorithm comparison. J. Geophys. Res.-Atmos. 102, 16697–16713. https://doi.org/10.1029/97JD00929.

Collings, S., Caccetta, P., Campbell, N., Wu, X., 2010. Techniques for BRDF correction of hyperspectral mosaics. IEEE Trans. Geosci. Remote Sens. 48 (10), 3733–3746. https://doi.org/10.1109/TGRS.2010.2048574.

Coops, N.C., Smith, M.L., Martin, M.E., Ollinger, S.V., 2003. Prediction of eucalypt foliage nitrogen content from satellite-derived hyperspectral data. IEEE Trans. Geosci. Remote Sens. 41 (6), 1338–1346. https://doi.org/10.1109/TGRS.2003.813135.

Coppola, D., Laiolo, M., Piscopo, D., Cigolini, C., 2013. Rheological control on the radiant density of active lava flows and domes. J. Volcanol. Geotherm. Res. 249, 39–48. https://doi.org/10.1016/j.jvolgeores.2012.09.005.

Cotrozzi, L., Townsend, P.A., Pellegrini, E., et al., 2018. Reflectance spectroscopy: A novel approach to better understand and monitor the impact of air pollution onv Mediterranean plants. Environ. Sci. Pollut. Res. 25, 8249–8267. https://doi.org/10.1007/s11356-017-9568-2.

Coulter, D.W., Hauff, P.L., Kerby, W.L., 2007. Airborne hyperspectral remote sensing. In: Milkereit, B. (Ed.), Proceedings of Exploration 07: Fifth Decennial International Conference on Mineral Exploration, pp. 375–386. http://www.dmec.ca/ex07-dvd/E07/pdfs/22.pdf.

Couture, J.J., Singh, A., Rubert-Nason, K.F., Serbin, S.P., Lindroth, R.L., Townsend, P.A., 2016. Spectroscopic determination of ecologically relevant plant secondary metabolites. Methods Ecol. Evol. 7, 1402–1412. https://doi.org/10.1111/2041-210X.12596.

Craig, S.E., Lohrenz, S.E., Lee, Z., Mahoney, K.L., Kirkpatrick, G.J., Schofield, O.M., Steward, R.G., 2006. Use of hyperspectral remote sensing reflectance for detection and assessment of the harmful alga, Karenia brevis. Appl. Opt. 45, 5414–5425. https://doi.org/10.1364/AO.45.005414.

Cudahy, T., 2016. Mineral mapping for exploration: an Australian journey of evolving spectral sensing technologies and industry collaboration. Geosciences 6 (4), 52. https://doi.org/10.3390/geosciences6040052.

Curran, P.J., 1989. Remote sensing of foliar chemistry. Remote Sens. Environ. 30 (3), 271–278. https://doi.org/10.1016/0034-4257(89)90069-2.

Cusworth, D.H., Jacob, D.J., Varon, D.J., Chan Miller, C., Liu, X., Chance, K., Thorpe, A. K., Duren, R.M., Miller, C.E., Thompson, D.R., Frankenberg, C., 2019. Potential of next-generation imaging spectrometers to detect and quantify methane point sources from space. Atmos. Measur. Techn. 12, 10. https://doi.org/10.5194/amt-12-5655-2019.

Czyz, E.A., Guillen Escriba, C., Wulf, H., Tedder, A., Schuman, M.C., Schneider, F.D., Schaepman, M.E., 2020. Intraspecific genetic variation of a Fagus sylvatica population in a temperate forest derived from airborne imaging spectroscopy time series. Ecol. Evolut. 10, 7419–7430. https://doi.org/10.1002/ece3.6469.

Dahlin, K., 2016. Spectral diversity area relationships for assessing biodiversity in a wildland-agriculture matrix. Ecol. Appl. 26, 2758–2768. https://doi.org/10.1002/eap.1390.

Daughtry, C.S.T., Doraiswamy, P.C., Hunt, E.R., Stern, A.J., McMurtrey, J.E., Prueger, J. H., 2006. Remote sensing of crop residue cover and soil tillage intensity. Soil Tillage Res. 91, 101–108. https://doi.org/10.1016/j.still.2005.11.013.

Dekker, A.G., Hestir, E.L., 2012. Evaluating the Feasibility of Systematic Inland Water Quality Monitoring with Satellite Remote Sensing. Commonwealth Scientific and Industrial Research Organization. https://doi.org/10.5072/83/58499fa75c2c9.

Dekker, A.G., Phinn, S.R., Anstee, J., Bissett, P., Brando, V.E., Casey, B., Fearns, P., Hedley, J., Klonowski, W., Lee, Z.P., Lynch, M., Lyons, M., Mobley, C., Roelfsema, C., 2011. Intercomparison of shallow water bathymetry, hydro-optics, and benthos mapping techniques in Australian and Caribbean coastal environments. Limnol. Oceanogr. Methods 9. https://doi.org/10.4319/lom.2011.9.396.

Denis, A., Stevens, A., Van Wesemael, B., Udelhoven, T., Tychon, B., 2014. Soil organic carbon assessment by field and airborne spectrometry in bare croplands: accounting for soil surface roughness. Geoderma 226, 94–102. https://doi.org/10.1016/j.geoderma.2014.02.015.

Dennison, P.E., Matheson, D.S., 2011. Comparison of fire temperature and fractional area modeled from SWIR, MIR, and TIR multispectral and SWIR hyperspectral airborne data. Remote Sens. Environ. 115, 876–888. https://doi.org/10.1016/j.rse.2010.11.015.

Dennison, P.E., Charoensiri, K., Roberts, D.A., Peterson, S.H., Green, R.O., 2006. Wildfire temperature and land cover modeling using hyperspectral data. Remote Sens. Environ. 100 (2), 212–222. https://doi.org/10.1016/j.rse.2005.10.007.

Dennison, P.E., Thorpe, A.K., Pardyjak, E.R., Roberts, D.A., Qi, Y., Green, R.O., Funk, C., 2013. High spatial resolution mapping of elevated atmospheric carbon dioxide using airborne imaging spectroscopy: Radiative transfer modeling and power plant plume detection. Remote Sensing of Environment 139, 116–129. https://doi.org/10.1016/j.rse.2013.08.001.

Dennison, P.E., Qi, Y., Meerdink, S.K., Kokaly, R.F., Thompson, D.R., Daughtry, C.S., Numata, I., 2019. Comparison of methods for modeling fractional cover using simulated satellite hyperspectral imager spectra. Remote Sensing 11 (18), 2072. https://doi.org/10.3390/rs11182072.

Devred, E., Turpie, K.R., Moses, W., Klemas, V.V., Moisan, T., Babin, M., Toro-Farmer, G., Forget, M.H., Jo, Y.H., 2013. Future retrievals of water column bio-optical properties using the hyperspectral infrared imager (HyspIRI). Remote Sens. 5 (12), 6812–6837. https://doi.org/10.3390/rs5126812.

Di Vittorio, A.V., 2009. Enhancing a leaf radiative transfer model to estimate concentrations and in vivo specific absorption coefficients of total carotenoids and chlorophylls a and b from single-needle reflectance and transmittance. Remote Sens. Environ. 113 (9), 1948–1966. https://doi.org/10.1016/j.rse.2009.05.002.

Diek, S., Schaepman, M.E., De Jong, R., 2016. Creating multi-temporal composites of airborne imaging spectroscopy data in support of digital soil mapping. Remote Sens. 8 (11), 906. https://doi.org/10.3390/rs8110906.

Diek, S., Chabrillat, S., Nocita, M., Schaepman, M.E., de Jong, R., 2019. Minimizing soil moisture variations in multi-temporal airborne imaging spectrometer data for digital soil mapping. Geoderma 337, 607–621. https://doi.org/10.1016/j.geoderma.2018.09.052.

Dierssen, H.M., 2019. Hyperspectral measurements, parameterizations, and atmospheric correction of whitecaps and foam from visible to shortwave infrared for ocean color remote sensing. Front. Earth Sci. 7, 14. https://doi.org/10.3389/feart.2019.00014.

Dierssen, H.M., Chlus, A., Russell, B., 2015a. Hyperspectral discrimination of floating mats of seagrass wrack and the macroalgae Sargassum in coastal waters of greater Florida bay using airborne remote sensing. Remote Sens. Environ. https://doi.org/10.1016/j.rse.2015.01.027.

Dierssen, H.M., McManus, G., Chlus, A., Qiua, D., Gao, B., Lin, S., 2015b. Space station image captures a red tide ciliate bloom at high spectral and spatial resolution. Proc. National Academy Sci 112 (48), 14783–14787. https://doi.org/10.1073/pnas.1512538112.

Dierssen, H., Bracher, A., Brando, V., Loisel, H., Ruddick, K., 2020. Data needs for hyperspectral detection of algal diversity across the globe. Oceanography 33, 74–79. https://doi.org/10.5670/oceanog.2020.111.

Dobos, E., 1998. Quantitative Analysis and Evaluation of AVHRR and Digital Terrain Data for Small-Scale Soil Pattern Recognition [PhD Thesis, Purdue University. UMI Number 9914481]. https://docs.lib.purdue.edu/dissertations/AAI9914481/.

Dobos, E., Micheli, E., Baumgardner, M., Biehl, L., Helt, T., 2000. Use of combined digital elevation model and satellite radiometric data for regional soil mapping. Geoderma 97 (3–4), 367–391. https://doi.org/10.1016/S0016-7061(00)00046-X.

Dogliotti, A.I., Ruddick, K.G., Nechad, B., Doxaran, D., Knaeps, E., 2015. A single algorithm to retrieve turbidity from remotely-sensed data in all coastal and estuarine waters. Remote Sens. Environ. 156, 157–168. https://doi.org/10.1016/j.rse.2014.09.020.

Dong, Q., Shang, S., Lee, Z., 2013. An algorithm to retrieve absorption coefficient of chromophoric dissolved organic matter from ocean color. Remote Sens. Environ. 128, 259–267. https://doi.org/10.1016/j.rse.2012.10.013.

Dozier, J., 1981. A method for satellite identification of surface temperature fields of subpixel resolution. Remote Sens. Environ. 11, 221–229. https://doi.org/10.1016/0034-4257(81)90021-3.

DuBois, S., Desai, A.R., Singh, A., Serbin, S.P., Goulden, M.L., Baldocchi, D.D., Ma, S., Oechel, W.C., Wharton, S., Kruger, E.L., Townsend, P.A., 2018. Using imaging spectroscopy to detect variation in terrestrial ecosystem productivity across a water-stressed landscape. Ecol. Appl. 28, 1313–1324. https://doi.org/10.1002/eap.1733.

Dupouy, C., Benielli-Gary, D., Neveux, J., Dandonneau, Y., Westberry, T.K., 2011. An algorithm for detecting Trichodesmium surface blooms in the South Western Tropical Pacific. Biogeosciences 8, 3631–3647. https://doi.org/10.5194/bg-8-3631-2011.

Durán, S.M., Martin, R.E., Diaz, S., Maitner, B.S., Malhi, Y., others, 2019. Informing trait-based ecology by assessing remotely sensed functional diversity across a broad tropical temperature gradient. Sci. Adv. 5. https://doi.org/10.1126/sciadv.aaw8114.

Duren, R.M., Thorpe, A.K., Foster, K.T., Rafiq, T., Hopkins, F.M., Yadav, V., Bue, B.D., Thompson, D.R., Conley, S., Colombi, N.K., Frankenberg, C., 2019. California's methane super-emitters. Nature 575 (7781), 180–184. https://doi.org/10.1038/s41586-019-1720-3.

Elvidge, C.D., 1990. Visible and near infrared reflectance characteristics of dry plant materials. Int. J. Remote Sens. 11 (10), 1775–1795. https://doi.org/10.1080/01431169008955129.

Elvidge, C.D., Chen, Z., 1995. Comparison of broad-band and narrow-band red and near-infrared vegetation indices. Remote Sens. Environ. 54 (1), 38–48. https://doi.org/10.1016/0034-4257(95)00132-K.

Fan, Y., Li, W., Gatebe, C.K., Jamet, C., Zibordi, G., Schroeder, T., Stamnes, K., 2017. Atmospheric correction over coastal waters using multilayer neural networks. Remote Sens. Environ. 199, 218–240. https://doi.org/10.1016/j.rse.2017.07.016.

Farrand, W.H., Harsanyi, J.C., 1997. Mapping the distribution of mine tailings in the Coeur d'Alene River valley, Idaho, through the use of a constrained energy minimization technique. Remote Sens. Environ. 59 (1), 64–76. https://doi.org/10.1016/S0034-4257(96)00080-6.

Fassnacht, F.E., Latifi, H., Stereńczakc, K., Modzelewska, A., Lefsky, M., et al., 2016. Review of studies on tree species classification from remotely sensed data. Remote Sens. Environ. 186, 64–87. https://doi.org/10.1016/j.rse.2016.08.013.

Feilhauer, H., Asner, G.P., Martin, R.E., Schmidtlein, S., 2010. Brightness-normalized partial least squares regression for hyperspectral data. J. Quant. Spectrosc. Radiat. Transf. 111 (12−13), 1947–1957. https://doi.org/10.1016/j.jqsrt.2010.03.007.

Feilhauer, H., Faude, U., Schmidtlein, S., 2011. Combining Isomap ordination and imaging spectroscopy to map continuous floristic gradients in a heterogeneous landscape. Remote Sens. Environ. 115, 2513–2524. https://doi.org/10.1016/j.rse.2011.05.011.

Féret, J.B., Asner, G.P., 2014. Mapping tropical forest canopy diversity using high-fidelity imaging spectroscopy. Ecol. Appl. 24, 1289–1296. https://doi.org/10.1890/13-1824.1.

Féret, J.-B., de Boissieu, F., 2020. BiodivMapR: an r package for α- and β-diversity mapping using remotely sensed images. Methods Ecol. Evol. 11, 64–70. https://doi.org/10.1111/2041-210X.13310.

Féret, J.-B., Gitelson, A.A., Noble, S.D., Jacquemoud, S., 2017. PROSPECT-D: towards modeling leaf optical properties through a complete lifecycle. Remote Sens. Environ. 193, 204–215. https://doi.org/10.1016/j.rse.2017.03.004.

Fichot, C.d.G., Downing, B.D., Bergamaschi, B.A., Windham-Myers, L., Marvin-DiPasquale, M., Thompson, D.R., Gierach, M.M., 2015. High-resolution remote sensing of water quality in the San Francisco Bay-Delta Estuary. Environ. Sci. Technol. 50, 573–583. https://doi.org/10.1021/acs.est.5b03518.

Finley, C.D., Glenn, N.F., 2010. Fire and vegetation type effects on soil hydrophobicity and infiltration in the sagebrush-steppe: II. Hyperspectral analysis. J. Arid Environ. 74 (6), 660–666. https://doi.org/10.1016/j.jaridenv.2009.11.010.

Fisher, J.B., Tu, K.P., Baldocchi, D.D., 2008. Global estimates of the land-atmosphere water flux based on monthly AVHRR and ISLSCP-II data, validated at 16 FLUXNET sites. Remote Sens. Environ. 112 (3), 901–919. https://doi.org/10.1016/j.rse.2007.06.025.

Fisher, J.B., Malhi, Y., de Arajo, A.C., Bonal, D., Gamo, M., Goulden, M.L., et al., 2009. The land-atmosphere water flux in the tropics. Glob. Chang. Biol. 15, 2694–2714. https://doi.org/10.1111/j.1365-2486.2008.01813.x.

Fisher, J.B., Melton, F., Middleton, E., Hain, C., Anderson, M., Allen, R., McCabe, M.F., Hook, S., Baldocchi, D., Townsend, P.A., Kilic, A., Tu, K., Miralles, D.D., Perret, J., Lagouarde, J.-P., Waliser, D., Purdy, A.J., French, A., Schimel, D., Wood, E.F., 2017. The future of evapotranspiration: global requirements for ecosystem functioning, carbon and climate feedbacks, agricultural management, and water resources. Water Resour. Res. 53 (4), 2618–2626. https://doi.org/10.1002/2016WR020175.

Fisher, J.B., Lee, B., Purdy, A.J., Halverson, G.H., Dohlen, M.B., Cawse-Nicholson, K., others, 2020. ECOSTRESS: NASA's next generation mission to measure evapotranspiration from the International Space Station. Water Resour. Res. 56 (4), 1–20. https://doi.org/10.1029/2019WR026058.

Foster, J.R., Townsend, P.A., 2004. Linking hyperspectral imagery and forest inventories for forest assessment in the Central Appalachians. In: Yaussy, D., Hix, D.M., Long, R. P., Goebel, P.C. (Eds.), *14th Central Hardwood Forest Conference* (Pp. 76–86). U.S. Department of Agriculture. https://www.fs.usda.gov/treesearch/pubs/22693.

Foster, J.R., Townsend, P.A., Zganjar, C.E., 2008. Spatial and temporal patterns of gap dominance by low-canopy lianas detected using EO-1 Hyperion and Landsat thematic mapper. Remote Sens. Environ. 112 (5), 2104–2117. https://doi.org/10.1016/j.rse.2007.07.027.

Frankenberg, C., Thorpe, A.K., Thompson, D.R., Hulley, G., Kort, E.A., Vance, N., Borchardt, J., Krings, T., Gerilowski, K., Sweeney, C., Conley, S., 2016. Airborne methane remote measurements reveal heavy-tail flux distribution in four corners region. Proc. Natl. Acad. Sci. 113 (35), 9734–9739. https://doi.org/10.1073/pnas.1605617113.

Freitas, F.H., Dierssen, H.M., 2019. Evaluating the seasonal and decadal performance of red band difference algorithms for chlorophyll in an optically complex estuary with winter and summer blooms. Remote Sens. Environ. 231, 111228 https://doi.org/10.1016/j.rse.2019.111228.

Friedrich, T., Oschlies, A., 2009. Neural network-based estimates of North Atlantic surface pCO2 from satellite data: A methodological study. J. Geophys. Res. Oceans 114 (C3). https://doi.org/10.1029/2007JC004646.

Frolov, S., Kudela, R.M., Bellingham, J.G., 2013. Monitoring of harmful algal blooms in the era of diminishing resources: A case study of the US west coast. Harmful Algae 21, 1–12. https://doi.org/10.1016/j.hal.2012.11.001.

Frouin, R.J., Gross-Colzy, L.S., 2016. Contribution of ultraviolet and shortwave infrared observations to atmospheric correction of PACE Ocean-color imagery. Rem. Sens. Oceans Inland Waters 9878, 98780C. https://doi.org/10.1117/12.2229891.

Frouin, R., Pelletier, B., 2015. Bayesian methodology for inverting satellite ocean-color data. Remote Sens. Environ. 159, 332–360. https://doi.org/10.1016/j.rse.2014.12.001.

Frouin, R., Schwindling, M., Deschamps, P.-Y., 1996. Spectral reflectance of sea foam in the visible and near-infrared: in situ measurements and remote sensing implications. J. Geophys. Res. 101, 14361–14371. https://doi.org/10.1029/96JC0062.

Frouin, R.J., Franz, B.A., Ibrahim, A., Knobelspiesse, K.D., Ahmad, Z., Cairns, B., Chowdhary, J., et al., 2019. Atmospheric correction of satellite ocean-color imagery during the PACE era. Front. Earth Sci. 7, 145. https://doi.org/10.3389/feart.2019.00145.

Gamon, J.A., Peñuelas, J., Field, C.B., 1992. A narrow-waveband spectral index that tracks diurnal changes in photosynthetic efficiency. Remote Sens. Environ. 41 (1), 35–44. https://doi.org/10.1016/0034-4257(92)90059-S.

Gamon, J.A., Huemmrich, K.F., Wong, C.Y., Ensminger, I., Garrity, S., Hollinger, D.Y., Noormets, A., Peñuelas, J., 2016. A remotely sensed pigment index reveals photosynthetic phenology in evergreen conifers. Proc. Natl. Acad. Sci. 113 (46), 13087–13092. https://doi.org/10.1073/pnas.1606162113.

Gao, B.-C., Li, R.-R., 2018. FVI—A Floating Vegetation Index Formed with Three Near-IR Channels in the 1.0–1.24 μm Spectral Range for the Detection of Vegetation Floating over Water Surfaces. Remote Sens. 10, 1421. https://doi.org/10.3390/rs10091421.

Gao, B.-C., Montes, M.J., Davis, C.O., Goetz, A.F., 2009. Atmospheric correction algorithms for hyperspectral remote sensing data of land and ocean. Remote Sens. Environ. 113, S17–S24. https://doi.org/10.1016/j.rse.2007.12.015.

Garaba, S.P., Dierssen, H.M., 2018. An airborne remote sensing case study of synthetic hydrocarbon detection using short wave infrared absorption features identified from marine-harvested macro-and microplastics. Remote Sens. Environ. 205, 224–235. https://doi.org/10.1016/j.rse.2017.11.023.

Garaba, S., Aitken, J., Slat, B., Dierssen, H.M., Lebreton, L., Zielinski, O., Reisser, J., 2018. Sensing ocean plastics with an airborne hyperspectral shortwave IR imager. Environ. Sci. Technol. 52, 11699–11707. https://doi.org/10.1021/acs.est.8b02855.

Garcia, R.A., Lee, Z., Hochberg, E.J., 2018. Hyperspectral shallow-water remote sensing with an enhanced benthic classifier. Remote Sens. 10 (1), 147. https://doi.org/10.3390/rs10010147.

Garcia, R.A., Lee, Z., Barnes, B.B., Hu, C., Dierssen, H.M., Hochberg, E.J., 2020. Benthic classification and IOP retrievals in shallow water environments using MERIS imagery. Remote Sens. Environ. 249, 112015. https://doi.org/10.1016/j.rse.2020.112015.

Garonna, I., de Jong, R., Schaepman, M.E., 2016. Variability and evolution of global land surface phenology over the past three decades (1982-2012). Glob. Chang. Biol. 22, 1456–1468. https://doi.org/10.1111/gcb.13168.

Gatebe, C.K., King, M.D., 2016. Airborne spectral BRDF of various surface types (ocean, vegetation, snow, desert, wetlands, cloud decks, smoke layers) for remote sensing applications. Remote Sens. Environ. 179, 131–148. https://doi.org/10.1016/j.rse.2016.03.029.

Gholizadeh, H., Gamon, J.A., Townsend, P.A., Zygielbaum, A.I., Helzer, C.J., et al., 2019. Detecting prairie biodiversity with airborne remote sensing. Remote Sens. Environ. 221, 38–49. https://doi.org/10.1016/j.rse.2018.10.037.

Ghunowa, K., Medeiros, A.S., Bello, R., 2019. Hyperspectral analysis of algal biomass in northern lakes, Churchill, MB, Canada. Arctic Sci. 5 (4), 240–256. https://doi.org/10.1139/as-2018-0030.

Giglio, L., Kendall, J.D., 2001. Application of the Dozier retrieval to wildfire characterization: A sensitivity analysis. Remote Sens. Environ. 77 (1), 34–49. https://doi.org/10.1016/S0034-4257(01)00192-4.

Giglio, L., Schroeder, W., Justice, C.O., 2016. The collection 6 MODIS active fire detection algorithm and fire products. Remote Sens. Environ. 178, 31–41. https://doi.org/10.1016/j.rse.2016.02.054.

Gilerson, A.A., Gitelson, A.A., Zhou, J., Gurlin, D., Moses, W., Ioannou, I., Ahmed, S.A., 2010. Algorithms for remote estimation of chlorophyll-a in coastal and inland waters using red and near infrared bands. Opt. Express 18 (23), 24109–24125. https://doi.org/10.1364/oe.18.024109.

Gillespie, A., Rokugawa, S., Matsunaga, T., Cothern, J.S., Hook, S., Kahle, A.B., 1998. A temperature and emissivity separation algorithm for advanced Spaceborne thermal emission and reflection radiometer (ASTER) images. IEEE Trans. Geosci. Remote Sens. 36, 1113–1126. https://doi.org/10.1109/36.700995.

Gitelson, A., Solovchenko, A., 2018. Non-invasive quantification of foliar pigments: possibilities and limitations of reflectance- and absorbance-based approaches. J. Photochem. Photobiol. B Biol. 178, 537–544. https://doi.org/10.1016/j.jphotobiol.2017.11.023.

Goetz, A.F.H., 2009. Three decades of hyperspectral remote sensing of the Earth: A personal view. Remote Sens. Environ. 113, S5–S16. https://doi.org/10.1016/j.rse.2007.12.014.

Goodman, J.A., Ustin, S.L., 2007. Classification of benthic composition in a coral reef environment using spectral unmixing. J. Appl. Remote. Sens. 1 (1), 011501 https://doi.org/10.1117/1.2815907.

Goodman, J.A., Lee, Z., Ustin, S.L., 2008. Influence of atmospheric and sea-surface corrections on retrieval of bottom depth and reflectance using a semi-analytical model: a case study in Kaneohe Bay, Hawaii. Appl. Opt. 47, F1–F11. https://doi.org/10.1364/AO.47.0000F1.

Gordon, H.R., 1997. Atmospheric correction of ocean color imagery in the Earth Observing System era. J. Geophys. Res. Oceans 102 (D14), 17081–17106. https://doi.org/10.1029/96JD02443.

Gordon, H.R., Wang, M., 1994. Retrieval of water-leaving radiance and aerosol optical thickness over the oceans with SeaWiFS: a preliminary algorithm. Appl. Opt. 33, 443–452. https://doi.org/10.1364/AO.33.000443.

Graham, G.E., Kokaly, R.F., Kelley, K.D., Hoefen, T.M., Johnson, M.R., Hubbard, B.E., 2018. Application of imaging spectroscopy for mineral exploration in Alaska: A study over porphyry Cu deposits in the Eastern Alaska Range. Econ. Geol. 113 (2), 489–510. https://doi.org/10.5382/econgeo.2018.4559.

Green, A.A., Berman, M., Switzer, P., Craig, M.D., 1988. A transformation for ordering multispectral data in terms of image quality with implications for noise removal. IEEE Trans. Geosci. Remote Sens. 26, 65–74. https://doi.org/10.1109/36.3001.

Grossman, Y.L., Ustin, S.L., Jacquemoud, S., Sanderson, E.W., Schmuck, G., Verdebout, J., 1996. Critique of stepwise multiple linear regression for the extraction of leaf biochemistry information from leaf reflectance data. Remote Sens. Environ. 56 (3), 182–193. https://doi.org/10.1016/0034-4257(95)00235-9.

Grunert, B.K., Mouw, C.B., Ciochetto, A.B., 2019. Deriving inherent optical properties from decomposition of hyperspectral non-water absorption. Remote Sens. Environ. 225, 193–206. https://doi.org/10.1016/j.rse.2019.03.004.

Gu, H., Singh, A., Townsend, P.A., 2015. Detection of gradients of forest composition in an urban area using imaging spectroscopy. Remote Sens. Environ. 167, 168–180. https://doi.org/10.1016/j.rse.2015.06.010.

Guerschman, J.P., Hill, M.J., Renzullo, L.J., Barrett, D.J., Marks, A.S., Botha, E.J., 2009. Estimating fractional cover of photosynthetic vegetation, non-photosynthetic vegetation and bare soil in the Australian tropical savanna region upscaling the EO-1 Hyperion and MODIS sensors. Remote Sens. Environ. 113, 928–945. https://doi.org/10.1016/j.rse.2009.01.006.

Guild, L.S., Kudela, R.M., Hooker, S.B., Palacios, S.L., Housekeeper, H.F., 2020. Airborne radiometry for calibration, validation, and research in oceanic, coastal, and inland waters. *Front*. Environ. Sci. 8, 585529 https://doi.org/10.3389/fenvs.2020.585529.

Gupta, R.P., 2017. Remote sensing geology. Springer.

Gurlin, D., Gitelson, A.A., Moses, W.J., 2011. Remote estimation of chl-a concentration in turbid productive waters—return to a simple two-band NIR-red model? Remote Sens. Environ. 115, 3479–3490. https://doi.org/10.1016/j.rse.2011.08.011.

Hakkenberg, C.R., Zhu, K., Peet, R.K., Song, C., 2018. Mapping multi-scale vascular plant richness in a forest landscape with integrated LiDAR and hyperspectral remote-sensing. Ecology 99, 474–487. https://doi.org/10.1002/ecy.2109.

Hall, F.G., Huemmrich, K.F., Goward, S.N., 1990. Use of narrow-band spectra to estimate the fraction of absorbed photosynthetically active radiation. Remote Sens. Environ. 32 (1), 47–54. https://doi.org/10.1016/0034-4257(90)90097-6.

Hall, D.K., Riggs, G.A., Salomonson, V.V., DiGirolamo, N.E., Bayr, K.A., 2002. MODIS snow-cover products. Remote Sens. Environ. 83, 181–194. https://doi.org/10.1016/S0034-4257(02)00095-0.

Han, B., Loisel, H., Vantrepotte, V., Mériaux, X., Bryère, P., Ouillon, S., Dessailly, D., Xing, Q., Zhu, J., 2016. Development of a semi-analytical algorithm for the retrieval of suspended particulate matter from remote sensing over clear to very turbid waters. Remote Sens. 8, 211. https://doi.org/10.3390/rs8030211.

Han, X., Feng, L., Hu, C., Kramer, P., 2018. Hurricane-induced changes in the Everglades National Park mangrove forest: Landsat observations between 1985 and 2017. J. Geophys. Res. Biogeosci. 123 https://doi.org/10.1029/2018JG004501.

Hapke, B., 1981. Bidirectional reflectance spectroscopy: 1. Theory. *J. Geophys. Res* 86, 3039–3054. https://doi.org/10.1029/JB086iB04p03039.

Hbirkou, C., Patzold, S., Mahlein, A.K., Welp, G., 2012. Airborne hyperspectral imaging of spatial soil organic carbon heterogeneity at the field-scale. Geoderma 175, 21–28. https://doi.org/10.1016/j.geoderma.2012.01.017.

Hedley, J.D., Harborne, A.R., Mumby, P.J., 2005. Technical note: simple and robust removal of sun glint for mapping shallow-water benthos. Int. J. Remote Sens. 26 (10), 2107–2112. https://doi.org/10.1080/01431160500034086.

Hestir, E.L., Brando, V.E., Bresciani, M., Giardino, C., Matta, E., Villa, P., Dekker, A.G., 2015. Measuring freshwater aquatic ecosystems: the need for a hyperspectral global mapping satellite mission. Remote Sens. Environ. 167, 181–195. https://doi.org/10.1016/j.rse.2015.05.023.

Heymann, J., Reuter, M., Buchwitz, M., Schneising, O., Bovensmann, H., Burrows, J.P., Massart, S., Kaiser, J.W., Crisp, D., O'Dell, C.W., 2017. CO2 emission of Indonesian fires in 2015 estimated from satellite-derived atmospheric CO2 concentrations. Geophys. Res. Lett. 44, 1537–1544. https://doi.org/10.1002/2016GL072042.

Hieronymi, M., Müller, D., Doerffer, R., 2017. The OLCI Neural Network Swarm (ONNS): A bio-geo-optical algorithm for open ocean and coastal waters. Front. Mar. Sci. 4, 140. https://doi.org/10.3389/fmars.2017.00140.

Hochberg, E.J., Atkinson, M.J., 2003. Capabilities of remote sensors to classify coral, algae, and sand as pure and mixed spectra. Remote Sens. Environ. 85 (2), 174–189. https://doi.org/10.1016/S0034-4257(02)00202-X.

Hochberg, E.J., Andrefouet, S., Tyler, M.R., 2003. Sea surface correction of high spatial resolution Ikonos images to improve bottom mapping in near-shore environments. IEEE Trans. Geosci. Remote Sens. 41 (7), 1724–1729. https://doi.org/10.1109/TGRS.2003.815408.

Hochberg, E.J., Mobley, C.D., Park, Y., Goodman, J., Turpie, K.R., Gao, B., Bruce, C.F., Green, R.O., Knox, R.G., Muller-Karger, F.E., Middleton, E.M., 2011. HyspIRI sunglint subgroup: Glint characterization, determination of impacts on science, and potential mitigation approaches [Presented Slides]. In: HyspIRI Science Workshop-NASA Decadal Survey Mission. https://hyspiri.jpl.nasa.gov/downloads/2010_Workshop/day1/day1_18_Hochberg_glint.pdf.

Hooker, S.B., Matsuoka, A., Kudela, R.M., Yamashita, Y., Suzuki, K., Housekeeper, H.F., 2020. A global end-member approach to derive aCDOM(440) from near-surface optical measurements. Biogeoscience 17, 475–497. https://doi.org/10.5194/bg-17-475-2020.

Housekeeper, H.F., Hooker, S.B., Kudela, R.M., 2021. Spectral range within global aCDOM(440) algorithms for oceanic, coastal, and inland waters with application to airborne measurements. Remote Sens. Environ. 252C https://doi.org/10.1016/j.rse.2020.112155.

Hu, C., 2009. A novel ocean color index to detect floating algae in the global oceans. Remote Sens. Environ. 113 (10), 2118–2129. https://doi.org/10.1016/j.rse.2009.05.012.

Hu, C., 2011. An empirical approach to derive MODIS Ocean color patterns under severe sun glint. Geophys. Res. Lett. 38, L01603. https://doi.org/10.1029/2010GL045422.

Hu, C., Muller-Karger, F.E., Taylor, C., Carder, K.L., Kelble, C., Johns, E., Heil, C., 2005. Red tide detection and tracing using MODIS fluorescence data: a regional example in

SW Florida coastal waters. Remote Sens. Environ. 97, 311–321. https://doi.org/10.1016/j.rse.2005.05.013.
Hu, C., Li, X., Pichel, W.G., Muller-Karger, F.E., 2009. Detection of natural oil slicks in the NW Gulf of Mexico using MODIS imagery. Geophys. Res. Lett. 36, L01604. https://doi.org/10.1029/2008GL036119.
Hu, C., Cannizzaro, J., Carder, K.L., Muller-Karger, F.E., Hardy, R., 2010. Remote detection of Trichodesmium blooms in optically complex coastal waters: examples with MODIS full-spectral data. Remote Sens. Environ. 114 (9), 2048–2058. https://doi.org/10.1016/j.rse.2010.04.011.
Hu, C., Feng, L., Hardy, R.F., Hochberg, E.J., 2015. Spectral and spatial requirements of remote measurements of pelagic Sargassum macroalgae. Remote Sens. Environ. 167, 229–246. https://doi.org/10.1016/j.rse.2015.05.022.
Hu, L., Hu, C., He, M.-X., 2017. Remote estimation of biomass of Ulva prolifera macroalgae in the Yellow Sea. Remote Sens. Environ. 192, 217–227. https://doi.org/10.1016/j.rse.2017.01.037.
Hubbard, B.E., Hooper, D.M., Solano, F., Mars, J.C., 2018. Determining mineralogical variations of aeolian deposits using thermal infrared emissivity and linear deconvolution methods. Aeolian Res. 30, 54–96. https://doi.org/10.1016/j.aeolia.2017.12.001.
Huemmrich, K.F., Campbell, P.K.E., Gao, B.C., Flanagan, L.B., Goulden, M., 2017. ISS as a platform for optical remote sensing of ecosystem carbon fluxes: A case study using HICO. IEEE J. Selected Top. Appl. Earth Observat. Remote Sens. 10 (10), 4360–4375. https://doi.org/10.1109/JSTARS.2017.2725825.
Huemmrich, K.F., Campbell, P.E., Voorhies, S.K., Landis, D.R., Middleton, E.M., 2018. Describing prairie C4 plant species area coverage using hyperspectral reflectance. Int. J. Remote Sens. 39 (23), 8615–8626. https://doi.org/10.1080/01431161.2018.1488294.
Huemmrich, K.F., Campbell, P.K.E., Landis, D., Middleton, E.M., 2019. Developing a common globally applicable method for optical remote sensing of ecosystem light use efficiency. Remote Sens. Environ. 230, 111190 https://doi.org/10.1016/j.rse.2019.05.009.
Hulley, G.C., Hook, S.J., 2018. ECOsystem Spaceborne Thermal Radiometer Experiment on Space Station (ECOSTRESS): Level-2 Land Surface Temperature and Emissivity Algorithm Theoretical Basis Document (ATBD). Jet Propulsion Laboratory, Pasadena. https://lpdaac.usgs.gov/products/eco2lstev001.
Hulley, G.C., Hughes, C.G., Hook, S.J., 2012. Quantifying uncertainties in land surface temperature and emissivity retrievals from ASTER and MODIS thermal infrared data. J. Geophys. Res.-Atmos. 117 https://doi.org/10.1029/2012JD018506.
Ibrahim, A., Franz, B., Ahmad, Z., Healy, R., Knobelspiesse, K., Gao, B.-C., Proctor, C., Zhai, P.-W., 2018. Atmospheric correction for hyperspectral ocean color retrieval with application to the hyperspectral imager for the Coastal Ocean (HICO). Remote Sens. Environ. 204, 60–75. https://doi.org/10.1016/j.rse.2017.10.041.
Ientilucci, E.J., Adler-Golden, S., 2019. Atmospheric compensation of hyperspectral data: an overview and review of in-scene and physics-based approaches. IEEE Geosci. Rem. Sens. Mag. 7 (2), 31–50. https://doi.org/10.1109/MGRS.2019.2904706.
Islam, T., Hulley, G.C., Malakar, N.K., Radocinski, R.G., Guillevic, P.C., Hook, S.J., 2017. A physics-based algorithm for the simultaneous retrieval of land surface temperature and emissivity from VIIRS thermal infrared data. IEEE Trans. Geosci. Remote Sens. 55 (1), 563–576. https://doi.org/10.1109/TGRS.2016.2611566.
Jensen, D.J., Simard, M., Cavanaugh, K.C., Thompson, D.R., 2018. Imaging spectroscopy BRDF correction for mapping Louisiana's coastal ecosystems. IEEE Trans. Geosci. Remote Sens. 56 (3), 1739–1748. https://doi.org/10.1109/TGRS.2017.2767607.
Jiménez, C., Prigent, C., Mueller, B., Seneviratne, S.I., McCabe, M.F., et al., 2011. Global inter-comparison of 12 land surface heat flux estimates. J. Geophys. Res. 116, D02102. https://doi.org/10.1029/2010JD014545.
Jo, Y.H., Kim, H.C., Hu, C., Klemas, V.V., Turpie, K.R., 2019. Potential applications of HyspIRI for the observation of sea-margin processes. J. Coast. Res. https://doi.org/10.2112/JCOASTRES-D-17-00089.1.
Johnson, M.S., Schwandner, F.M., Potter, C.S., Nguyen, H.M., Bell, E., Nelson, R.R., 2020. Carbon dioxide emissions during the 2018 Kilauea volcano eruption estimated using OCO-2 satellite retrievals. Geophys. Res. Lett. https://doi.org/10.1029/2020GL090507 e2020GL090507.
Johnson, P.E., Smith, M.O., Adams, J.B., 1985. Quantitative analysis of planetary reflectance spectra with principal components analysis. J. Geophys. Res. 90, 805–810. https://doi.org/10.1029/JB090iS02p0C805.
Johnson, P.E., Smith, M.O., Adams, J.B., 1992. Simple algorithms for remote determination of mineral abundance and particle sizes from reflectance spectra. J. Geophys. Res. 97, 2649–2657. https://doi.org/10.1029/91JE02504.
Jones, M.O., Allred, B.W., Naugle, D.E., Maestas, J.D., Donnelly, P., Metz, L.J., Karl, J., Smith, R., Bestelmeyer, B., Boyd, C., Kerby, J.D., McIver, J.D., 2018. Innovation in rangeland monitoring: Annual, 30 m, plant functional type percent cover maps for U. S. rangelands, 1984–2017. Ecosphere 9 (9), e02430. https://doi.org/10.1002/ecs2.2430.
Jutzeler, M., Marsh, R., Carey, R.J., White, J.D.L., Talling, P.J., Karlstrom, L., 2014. On the fate of pumice rafts formed during the 2012 Havre submarine eruption. Nat. Commun. 5, 3660. https://doi.org/10.1038/ncomms4660.
Kahru, M., 2017. Ocean productivity from space: commentary. Glob. Biogeochem. Cycles 31 (1), 214–216. https://doi.org/10.1002/2016GB005582.
Kaiser, J.W., Heil, A., Andreae, M.O., Benedetti, A., Chubarova, N., Jones, L., Van Der Werf, G.R., 2012. Biomass burning emissions estimated with a global fire assimilation system based on observed fire radiative power. Biogeosciences 9 (1), 527. https://doi.org/10.5194/bg-9-527-2012.
Kamoske, A.G., Dahlin, K.M., Serbin, S.P., Stark, S.C., 2020. Leaf traits and canopy structure together explain canopy functional diversity: An airborne remote sensing approach. Ecology, e02230. https://doi.org/10.1002/eap.2230.
Kattenborn, T., Fassnacht, F.E., Schmidtlein, S., 2019. Differentiating plant functional types using reflectance: which traits make the difference? Remote Sens. Ecol. Conserv. 5 (1), 5–19. https://doi.org/10.1002/rse2.86.
Kay, S., Hedley, J.D., Lavender, S., 2009. Sun glint correction of high and low spatial resolution images of aquatic scenes: A review of methods for visible and near-infrared wavelengths. Remote Sens. 1 (4), 697–730. https://doi.org/10.3390/rs1040697.
Kealy, P.S., Hook, S., 1993. Separating temperature and emissivity in thermal infrared multispectral scanner data: implication for recovering land surface temperatures. IEEE Trans. Geosci. Remote Sens. 31, 1155–1164. https://doi.org/10.1109/36.317447.
Kerekes, J., Glennon, M., Lockwood, R., 2003. Unmixing analysis: Model prediction compared to observed results. *IGARSS* 2003. In: 2003 *IEEE International Geoscience and Remote Sensing Symposium (IEEE Cat. No.03CH37477)*, pp. 99–102. https://doi.org/10.1109/IGARSS.2003.1293691.
Khan, A.L., Dierssen, H., Schwarz, J.P., Schmitt, C., Chlus, A., Hermanson, M., Painter, T. H., McKnight, D.M., 2017. Impacts of coal dust from an active mine on the spectral reflectance of Arctic surface snow in Svalbard, Norway. J. Geophys. Res.-Atmos. 122, 1767–1778. https://doi.org/10.1002/2016JD025757.
Khan, A.L., Dierssen, H., Scambos, T., Höfer, J., Cordero, R.R., 2020. Spectral characterization, radiative forcing, and pigment content of coastal Antarctic snow algae: approaches to spectrally discriminate red and green communities and their impact on snowmelt. Cryosphere. 1–27. https://doi.org/10.5194/tc-2020-170.
Kikaki, A., Karantzalos, K., Power, C.A., Raitsos, D.E., 2020. Remotely sensing the source and transport of marine plastic debris in Bay Islands of Honduras (Caribbean Sea). Remote Sens. 12, 1727. https://doi.org/10.3390/rs12111727.
Kim, Y., Yoo, S., Son, Y.B., 2016. Optical discrimination of harmful Cochlodinium polykrikoides blooms in Korean coastal waters. Opt. Express 24, A1471–A1488. https://doi.org/10.1364/OE.24.0A1471.
Klemas, V., 2012. Remote sensing of algal blooms: an overview with case studies. J. Coast. Res. 28 (1A), 34–43. https://doi.org/10.2112/JCOASTRES-D-11-00051.1.
Knaeps, E., Ruddick, K.G., Doxaran, D., Dogliotti, A.I., Nechad, B., Raymaekers, D., Sterckx, S., 2015. A SWIR based algorithm to retrieve total suspended matter in extremely turbid waters. Remote Sens. Environ. 168, 66–79. https://doi.org/10.1016/j.rse.2015.06.022.
Knox, N.M., Skidmore, A.K., Prins, H.H.T., Asner, G., et al., 2011. Dry season mapping of savanna forage quality, using the hyperspectral Carnegie Airborne Observatory sensor. Remote Sens. Environ. 115 (6), 1478–1488. https://doi.org/10.1016/j.rse.2011.02.007.
Knyazikhin, Y., Schull, M.A., Stenberg, P., Mõttus, M., Rautiainen, M., Yang, Y., Myneni, R.B., 2013. Hyperspectral remote sensing of foliar nitrogen content. In: Proceedings of the National Academy of Sciences, 110(3), pp. E185–E192. https://doi.org/10.1073/pnas.1210196109.
Koetz, B., Bastiaanssen, W.G.M., Berger, M., Defourny, P., del Bello, U., et al., 2019. Agriculture: Land Surface Temperature Monitoring (LSTM) Mission. In: ESA Living Planet Symposium.
Kokaly, R.F., 2011. PRISM: Processing routines in IDL for spectroscopic measurements (installation manual and user's guide, version 1.0). In: U.S Geological Survey Open-File Report. https://pubs.usgs.gov/of/2011/1155/.
Kokaly, R.F., Despain, D.G., Clark, R.N., Livo, K.E., 2003. Mapping vegetation in Yellowstone National Park using spectral feature analysis of AVIRIS data. Remote Sens. Environ. 84 (3), 437–456. https://doi.org/10.1016/S0034-4257(02)00.
Kokaly, R.F., King, T.V.V., Hoefen, T.M., 2013. Surface mineral maps of Afghanistan derived from HyMap imaging spectrometer data, version 2. In: U.S. Geological Survey Data Series 787. https://pubs.usgs.gov/ds/787/.
Kokaly, R., Graham, G.E., Hoefen, T.M., Kelley, K.D., Johnson, M.R., Hubbard, B.E., Buchhorn, M., Prakash, A., 2018. Multiscale hyperspectral imaging of the Orange Hill porphyry copper deposit, Alaska, USA, with laboratory-, Field-, and aircraft-based imaging spectrometers. In: Sixth Decennial International Conference on Mineral Exploration. Spectral Geology and Remote Sensing, pp. 923–943. https://pubs.er.usgs.gov/publication/70199140.
Kopacková, V., Ben-Dor, E., Carmon, N., Notesco, G., 2017. Modelling diverse soil attributes with visible to longwave infrared spectroscopy using PLSR employed by an automatic modelling engine. Remote Sens. 9 (2), 134. https://doi.org/10.3390/rs9020134.
Kudela, R.M., Palacios, S.L., Austerberry, D.C., Accorsi, E.K., Guild, L.S., Torres-Perez, J., 2015. Application of hyperspectral remote sensing to cyanobacterial blooms in inland waters. Remote Sens. Environ. 167, 196–205. https://doi.org/10.1016/j.rse.2015.01.025.
Laakso, K., Rivard, B., Rogge, D., 2016. Enhanced detection of gossans using hyperspectral data: example from the cape Smith Belt of northern Quebec, Canada. ISPRS J. Photogramm. Remote Sens. 114, 137–150. https://doi.org/10.1016/j.isprsjprs.2016.02.004.
Lagacherie, P., Baret, F., Feret, J.B., Netto, J.M., Robbez-Masson, J.M., 2008. Estimation of soil clay and calcium carbonate using laboratory, field and airborne hyperspectral measurements. Remote Sens. Environ. 112 (3), 825–835. https://doi.org/10.1016/j.rse.2007.06.014.
Lagouarde, J.P., Bhattacharya, B.K., Crebassol, P., Gamet, P., Adlakha, D., et al., 2019. Indo-French high-resolution thermal infrared space mission for Earth natural resources assessment and monitoring—Concept and definition of TRISHNA. In: International Archives of the Photogrammetry and Remote Sensing and Spatial Information Sciences - ISPRS Archives, pp. 403–407. https://ui.adsabs.harvard.edu/link_gateway/2019ISPAr.423..403L/doi:10.5194/isprs-archives-XLII-3-W6-403-2019.

Lamb, B., Tzortziou, M., McDonald, K., 2019. Evaluation of approaches for mapping tidal wetlands of the Chesapeake and Delaware Bays. Remote Sens. 11 (20), 2366. https://doi.org/10.3390/rs11202366.

Lang, M.W., Townsend, P.A., Kasischke, E.S., 2008. Influence of incidence angle on detecting flooded forests using C-HH synthetic aperture radar data. Remote Sens. Environ. 112 (10), 3898–3907. https://doi.org/10.1016/j.rse.2008.06.013.

Laurent, V.C.E., Schaepman, M.E., Verhoef, W., Weyermann, J., Chavez, R.O., 2014. Bayesian object-based estimation of LAI and chlorophyll from a simulated Sentinel-2 top-of-atmosphere radiance image. Remote Sens. Environ. 140, 318–329. https://doi.org/10.1016/j.rse.2013.09.005.

Le, C., Zhou, X., Hu, C., Lee, Z., Li, L., Stramski, D., 2018. A color-index-based empirical algorithm for determining particulate organic carbon concentration in the ocean from satellite observations. J. Geophys. Res. Oceans 123, 7407–7419. https://doi.org/10.1029/2018JC014014.

Lee, Z., Carder, K.L., Mobley, C.D., Steward, R.G., Patch, J.S., 1998. Hyperspectral remote sensing for shallow waters. I. A semianalytical model. Appl. Opt. 37, 6329–6338. https://doi.org/10.1364/AO.37.006329.

Lee, Z., Carder, K.L., Mobley, C.D., Steward, R.G., Patch, J.S., 1999. Hyperspectral remote sensing for shallow waters: 2. Deriving bottom depths and water properties by optimization. Appl. Opt. 38, 3831–3843. https://doi.org/10.1364/AO.38.003831.

Lee, Z.P., Carder, K.L., Arnone, R.A., 2002. Deriving inherent optical properties from water color: A multiband quasi-analytical algorithm for optically deep waters. Appl. Opt. 41, 5755–5772. https://doi.org/10.1364/AO.41.005755.

Lee, Z., Lubac, B., Werdell, J., Arnone, R., 2009. An update of the quasi-analytical algorithm (QAA_v5). http://www.ioccg.org/groups/Software_OCA/QAA_v5.pdf.

Lee, Z., Hu, C., Casey, B., Shang, S., Dierssen, H., Arnone, R., 2010. Global shallow-water bathymetry from satellite ocean color data. EOS Trans. Am. Geophys. Union 91 (46), 429–430. https://doi.org/10.1029/2010EO460002.

Lekki, J., Anderson, R., Avouris, D., Becker, R., Churnside, J., Cline, M., Demers, J., Leshkevich, G., Liou, L., Luvall, J., Ortiz, J., Royce, A., Ruberg, S., Sawtell, R., Sayers, M., Schiller, S., Shuchman, R., Anita, S.M., Stuart, D., Woude, A., 2017. *Airborne Hyperspectral Sensing of Harmful Algal Blooms in the Great Lakes Region: System Calibration and Validation* (NASA/TM-2017-219071). https://ntrs.nasa.gov/archive/nasa/casi.ntrs.nasa.gov/20170002298.pdf.

Li, J., Yu, Q., Tian, Y.Q., Becker, B.L., 2017. Remote sensing estimation of colored dissolved organic matter (CDOM) in optically shallow waters. ISPRS J. Photogramm. Remote Sens. 128, 98–110. https://doi.org/10.1016/j.isprsjprs.2017.03.015.

Li, J., Yu, Q., Tian, Y.Q., Boutt, D.F., 2018. Effects of landcover, soil property, and temperature on covariations of DOC and CDOM in inland waters. J. Geophys. Res. Biogeosci. 123, 1352–1365. https://doi.org/10.1002/2017JG004179.

Li, J., Knapp, D.E., Schill, S.R., Roelfsema, C., Phinn, S., Silman, M., Asner, G.P., 2019a. Adaptive bathymetry estimation for shallow coastal waters using Planet Dove satellites. Remote Sensing of Environment 232, 11130. https://doi.org/10.1016/j.rse.2019.111302.

Li, J., Schill, S.R., Knapp, D.E., Asner, G.P., 2019b. Object-based mapping of coral reef habitats using planet dove satellites. Remote Sens. 11 (12), 1445. https://doi.org/10.3390/rs11121445.

Lobell, D.B., Asner, G.P., 2004. Cropland distributions from temporal unmixing of MODIS data. Remote Sens. Environ. 93 (3), 412–422. https://doi.org/10.1016/j.rse.2004.08.002.

Lohrenz, S.E., Cai, W.J., 2006. Satellite ocean color assessment of air-sea fluxes of CO2 in a river-dominated coastal margin. Geophys. Res. Lett. 33, 1. https://doi.org/10.1029/2005GL023942.

Loisel, H., Stramski, D., Dessailly, D., Jamet, C., Li, L., Reynolds, R.A., 2018. An inverse model for estimating the optical absorption and backscattering coefficients of seawater from remote-sensing reflectance over a broad range of oceanic and coastal marine environments. J. Geophys. Res. Oceans 123 (3), 2141–2171. https://doi.org/10.1002/2017JC013632.

Lombardo, V., Musacchio, M., Buongiorno, M.F., 2012. Error analysis of subpixel lava temperature measurements using infrared remotely sensed data. Geophys. J. Int. 191 (1), 112–125. https://doi.org/10.1111/j.1365-246X.2012.05632.x.

Loncan, L., Almeida, L.B., Bioucas-dias, M., Briottet, X., Chanussot, J., Dobigeon, N., Fabre, S., Liao, W., Licciardi, G.A., Sim, M., et al., 2015. Hyperspectral pansharpening: A review. IEEE Geosci. Remote Sens. Mag 3, 27–46. https://doi.org/10.1109/MGRS.2015.2440094.

Lu, Y., Shi, J., Wen, Y., Hu, C., Zhou, Y., Sun, S., Zhang, M., Mao, Z., Liu, Y., 2019. Optical interpretation of oil emulsions in the ocean—part I: laboratory measurements and proof-of-concept with AVIRIS observations. Remote Sens. Environ. 230 (11118), 3. https://doi.org/10.1016/j.rse.2019.05.002.

Lu, Y., Shi, J., Hu, C., Zhang, S., Sun, M., 2020. Optical interpretation of oil emulsions in the ocean—part II: applications to multi-band coarse-resolution imagery. Remote Sens. Environ. 242 (111778) https://doi.org/10.1016/j.rse.2020.111778.

Ma, Z., Jia, G., Schaepman, M.E., Zhao, H., 2020. Uncertainty analysis for topographic correction of hyperspectral remote sensing images. Remote Sens. 12 https://doi.org/10.3390/rs12040705.

Madritch Michael, D., Kingdon Clayton, C., Aditya, Singh, Mock Karen, E., Lindroth Richard, L., Townsend Philip, A., 2014. Imaging spectroscopy links aspen genotype with below-ground processes at landscape scales. Phil. Trans. R. Soc. https://doi.org/10.1098/rstb.2013.0194 (B36920130194).

Malakar, N.K., Hulley, G.C., 2016. A water vapor scaling model for improved land surface temperature and emissivity separation of MODIS thermal infrared data. Remote Sens. Environ. 182, 252–264. https://doi.org/10.1016/j.rse.2016.04.023.

Malenovsky, Z., Rott, H., Cihlar, J., Schaepman, M.E., Garcia-Santos, G., Fernandes, R., Berger, M., 2012. Sentinels for science: potential of Sentinel-1, −2, and −3 missions for scientific observations of ocean, cryosphere, and land. Remote Sens. Environ. 120, 91–101. https://doi.org/10.1016/j.rse.2011.09.026.

Manna, A.J., 1985. 25 years of Tiros satellites. Bull. Am. Meteorol. Soc. 66 (4), 421–423. https://doi.org/10.1175/1520-0477(1985)066.

Mannino, A., Russ, M.E., Hooker, S.B., 2008. Algorithm development and validation for satellite-derived distributions of DOC and CDOM in the US Middle Atlantic Bight. J. Geophys. Res. Oceans 113. https://doi.org/10.1029/2007JC004493.

Maritorena, S., Morel, A., Gentili, B., 1994. Diffuse reflectance of oceanic shallow waters: influence of water depth and bottom albedo. Limnol. Oceanogr. 39, 1689–1703. https://doi.org/10.4319/lo.1994.39.7.1689.

Maritorena, S., Siegel, D.A., Peterson, A.R., 2002. Optimization of a semianalytical ocean color model for global-scale applications. Appl. Opt. 41 (15), 2705–2714. https://doi.org/10.1364/AO.41.002705.

Martin, M.E., Newman, S.D., Aber, J.D., Congalton, R.G., 1998. Determining forest species composition using high spectral resolution remote sensing data. Remote Sens. Environ. 65 (3), 249–254. https://doi.org/10.1016/S0034-4257(98)00035-2.

Martin, R.E., Chadwick, K.D., Brodrick, P.G., Carranza-Jimenez, L., Vaughn, N.R., Asner, G.P., 2018. An approach for foliar trait retrieval from airborne imaging spectroscopy of tropical forests. Remote Sens. 10, 199. https://doi.org/10.3390/rs10020199.

Marvin, D.C., Asner, G.P., Schnitzer, S.A., 2016. Liana canopy cover mapped throughout a tropical forest with high-fidelity imaging spectroscopy. Remote Sens. Environ. 176, 98–106. https://doi.org/10.1016/j.rse.2015.12.028.

Masiello, G., Serio, C., De Feis, I., Amoroso, M., Venafra, S., Trigo, I.F., Watts, P., 2013. Kalman filter physical retrieval of surface emissivity and temperature from geostationary infrared radiances. Atmos. Measur. Techn. 6, 3613–3634. https://doi.org/10.5194/amt-6-3613-2013.

Matheson, D.S., Dennison, P.E., 2012. Evaluating the effects of spatial resolution on hyperspectral fire detection and temperature retrieval. Remote Sens. Environ. 124, 780–792. https://doi.org/10.1016/j.rse.2012.06.026.

Matricardi, M., Chevallier, F., Tjemkes, S., 2001. An improved general fast radiative transfer model for the assimilation of radiance observations. ECMWF Research Dept. Tech. Memo. 345. https://doi.org/10.21957/1si9lq6pb.

Matthews, M.W., 2011. A current review of empirical procedures of remote sensing in inland and near-coastal transitional waters. Int. J. Remote Sens. 32 (21), 6855–6899. https://doi.org/10.1080/01431161.2010.512947.

Mckinna, L.I.W., 2015. Three decades of ocean-color remote-sensing Trichodesmium spp. in the World's oceans: A review. Prog. Oceanogr. 131, 177–199. https://doi.org/10.1016/j.pocean.2014.12.013.

Meerdink, S.K., Roberts, D.A., Roth, K.L., King, J.Y., Gader, P.D., Koltunov, A., 2019. Classifying California plant species temporally using airborne hyperspectral imagery. Remote Sens. Environ. 232 (11130), 8. https://doi.org/10.1016/j.rse.2019.111308.

Meireles, J.E., Cavender-Bares, J., Townsend, P.A., Ustin, S., Gamon, J.A., Schweiger, A. K., Schaepman, M.E., Asner, G.P., Martin, R.E., Singh, A., Schrodt, F., Chlus, A., O'Meara, B.C., 2020. Leaf reflectance spectra capture the evolutionary history of seed plants. New Phytol. 228, 485–493. https://doi.org/10.1111/nph.16771.

Meister, G., McClain, C.R., Ahmad, Z., Bailey, S.W., Barnes, R.A., Brown, S., Eplee, R.E., Franz, B., Holmes, A., Monosmith, W.B., Patt, F.S., Stumpf, R.P., Turpie, K.R., Werdell, P.J., 2011. *Requirements for an advanced ocean radiometer*. NASA/TM-2011-215883, GSFC.TM.5375.2011. Goddard Space Flight Center Greenbelt, Maryland, p. 20771. https://pace.oceansciences.org/docs/01_NASATM20110023620.pdf.

Metsämäki, S.J., Anttila, S.T., Markus, H.J., Vepsäläinen, J.M., 2005. A feasible method for fractional snow cover mapping in boreal zone based on a reflectance model. Remote Sens. Environ. 95 (1), 77–95. https://doi.org/10.1016/j.rse.2004.11.013.

Mielke, C., Rogass, C., Boesche, N., Segl, K., Altenberger, U., 2016. EnGeoMAP 2.0: automated hyperspectral mineral identification for the German EnMAP space mission. Remote Sens. 8, 127. https://doi.org/10.3390/rs8020127.

Minnett, P.J., Alvera-Azcarate, A., Chin, T.M., Corlett, G.K., Gentemann, C.L., et al., 2019. Half a century of satellite remote sensing of sea-surface temperature. Remote Sens. Environ. 233, 111366. https://doi.org/10.1016/j.rse.2019.111366.

Miralles, D.G., Holmes, T.R.H., Jeu, R.A.M.D., Gash, J.H., Meesters, A.G.C.A., Dolman, A. J., 2011. Global land-surface evaporation estimated from satellite-based observations. Hydrol. Earth Syst. Sci. 15 (2), 453–469. https://doi.org/10.5194/hess-15-453-2011.

Mitchell, C., Hu, C., Bowler, B., Drapeau, D., Balch, W.M., 2017. Estimating particulate inorganic carbon concentrations of the global ocean from ocean color measurements using a reflectance difference approach. J. Geophys. Res. Oceans 122, 8707–8720. https://doi.org/10.1002/2017JC013146.

Mobley, C.D., Sundman, L.K., Davis, C.O., Downes, T.V., Leathers, R.A., Montes, M.J., Bowles, J.H., Bissett, W.P., Ddr, K., Reid, R.P., Louchard, E.M., Gleason, A., 2005. Interpretation of hyperspectral remote-sensing imagery via spectrum matching and look-up tables. Appl. Opt. 44, 3576–3592. https://doi.org/10.1364/AO.44.003576.

Montes, M.J., Gao, B.C., Davis, C.O., 2001. A new algorithm for atmospheric correction of hyperspectral remote sensing data. In: Roper, W.E. (Ed.), Geo-Spatial Image and Data Exploitation II, pp. 23–30. Proceedings of the SPIE. https://doi.org/10.1117/12.428247.

Moses, W.J., Gitelson, A.A., Berdnikov, S., Saprygin, V., Povazhnyi, V., 2012. Operational MERIS-based NIR-red algorithms for estimating chlorophyll-a concentrations in coastal waters—The Azov Sea case study. Remote Sens. Environ. 121, 118–124. https://doi.org/10.1016/j.rse.2012.01.024.

Mouw, C.B., Barnett, A., McKinley, G.A., Gloege, L., Pilcher, D., 2016. Global ocean particulate organic carbon flux merged with satellite parameters. Earth System Sci. Data 8, 531–541. https://doi.org/10.5194/essd-8-531-2016.

Mouw, C.B., Hardman-Mountford, N.J., Alvain, S., Bracher, A., Brewin, R.J., Bricaud, A., Ciotti, A.M., Devred, E., Fujiwara, A., Hirata, T., Hirawake, T., 2017. A consumer's

guide to satellite remote sensing of multiple phytoplankton groups in the global ocean. Front. Mar. Sci. 4, 41. https://doi.org/10.3389/fmars.2017.00041.
Mu, Q., Zhao, M., Running, S.W., 2011. Improvements to a MODIS global terrestrial evapotranspiration algorithm. Remote Sens. Environ. 111, 519–536. https://doi.org/10.1016/j.rse.2011.02.019.
Muller-Karger, F.E., Hestir, E., Ade, C., Turpie, K., Roberts, D., others, 2018. Satellite sensor requirements for monitoring essential biodiversity variables of coastal ecosystems. Ecol. Appl. 28 (3), 749–760. https://doi.org/10.1002/eap.1682. Ecological Society of America.
Nagler, P.L., Daughtry, C.S.T., Goward, S.N., 2000. Plant litter and soil reflectance. Remote Sens. Environ. 71, 207–215. https://doi.org/10.1016/S0034-4257(99)00082-6.
Nassar, R., Hill, T.G., McLinden, C.A., Wunch Jones, D., Crisp, D., 2017. Quantifying CO2 emissions from individual power plants from space. Geophys. Res. Lett. 44 https://doi.org/10.1002/2017GL074702.
National Academies of Sciences, Engineering, Aand Medicine, 2018. Thriving on Our Changing Planet: A Decadal Strategy for Earth Observation from Space. The National Academies Press. https://doi.org/10.17226/24938.
Nechad, B., Ruddick, K.G., Park, Y., 2010. Calibration and validation of a generic multisensor algorithm for mapping of total suspended matter in turbid waters. Rem. Sens. Environ. 114 (4), 854–866. https://doi.org/10.1016/j.rse.2009.11.022 (ISSN 0034-4257).
Nieke, J., Rast, M., 2019. Status: Copernicus hyperspectral imaging Mission for the. Environment (CHIME). 4609–4611. https://doi.org/10.1109/IGARSS.2019.8899807.
Novoa, S., Doxaran, D., Ody, A., Vanhellemont, Q., Lafon, V., Lubac, B., Gernez, P., 2017. Atmospheric corrections and multi-conditional algorithm for multi-sensor remote sensing of suspended particulate matter in low-to-high turbidity levels coastal waters. Remote Sens. 9, 61. https://doi.org/10.3390/rs9010061.
Numata, I., Roberts, D.A., Chadwick, O.A., Schimel, J.P., Galvão, L.S., Soares, J.V., 2008. Evaluation of hyperspectral data for pasture estimate in the Brazilian Amazon using field and imaging spectrometers. Remote Sens. Environ. 112, 1569–1583. https://doi.org/10.1016/j.rse.2007.08.014.
O'Connor, B., Bojinski, S., Roosli, C., Schaepman, M.E., 2020. Monitoring global changes in biodiversity and climate essential as ecological crisis intensifies. Ecol. Informat. 55, 101033 https://doi.org/10.1016/j.ecoinf.2019.101033.
Odermatt, D., Gitelson, A., Brando, V.E., Schaepman, M., 2012a. Review of constituent retrieval in optically deep and complex waters from satellite imagery. Remote Sens. Environ. 118, 116–126. https://doi.org/10.1016/j.rse.2011.11.013.
Odermatt, D., Pomati, F., Pitarch, J., Carpenter, J., Kawka, M., Schaepman, M.E., Wüest, A., 2012b. MERIS observations of phytoplankton blooms in a stratified eutrophic lake. Remote Sens. Environ. 126, 232–239. https://doi.org/10.1016/j.rse.2012.08.031.
Oppenheimer, C., 1996. Crater lake heat losses estimated by remote sensing. Geophys. Res. Lett. 23 (14), 1793–1796. https://doi.org/10.1029/96GL01591.
Oppenheimer, C., 1997. Remote sensing of the colour and temperature of volcanic lakes. Int. J. Remote Sens. 18 (1), 5–37. https://doi.org/10.1080/014311697219259.
Ortiz, J.D., Witter, D.L., Ali, K.A., Fela, N., Duff, M., Mills, L., 2013. Evaluating multiple colour-producing agents in case II waters from Lake Erie. Int. J. Remote Sens. 34 (24), 8854–8880. https://doi.org/10.1080/01431161.2013.853892.
Ortiz, J.D., Avouris, D., Schiller, S., Luvall, J.C., Lekki, J.D., Tokars, R.P., Anderson, R.C., Shuchman, R., Sayers, M., Becker, R., 2017. Intercomparison of approaches to the empirical line method for vicarious hyperspectral reflectance calibration. Front. Mar. Sci. 4, 296. https://doi.org/10.3389/fmars.2017.00296.
Ortiz, J.D., Avouris, D.M., Schiller, S.J., Luvall, J.C., Lekki, J.D., Tokars, R.P., Anderson, R.C., Shuchman, R., Sayers, M., Becker, R., 2019. Evaluating visible derivative spectroscopy by varimax-rotated, principal component analysis of aerial hyperspectral images from the western basin of Lake Erie. J. Great Lakes Res. 45 (3), 522–535. https://doi.org/10.1016/j.jglr.2019.03.005.
Ozdogan, M., 2010. The spatial distribution of crop types from MODIS data: temporal unmixing using independent component analysis. Remote Sens. Environ. 114 (6), 1190–1204. https://doi.org/10.1016/j.rse.2010.01.006.
Pahlevan, N., Smith, B., Schalles, J., Binding, C., Cao, Z., Ma, R., Alikas, K., Kangro, K., Gurlin, D., Hà, N., Matsushita, B., Moses, W., Greb, S., Lehmann, M.K., Ondrusek, M., Oppelt, N., Stumpf, R., 2020. Seamless retrievals of chlorophyll-a from Sentinel-2 (MSI) and Sentinel-3 (OLCI) in inland and coastal waters: A machine-learning approach. Remote Sens. Environ. 111604 https://doi.org/10.1016/j.rse.2019.111604.
Pahlevan, N., Smith, B., Binding, C., Gurlin, D., Li, L., Bresciani, M., Giardino, C., 2021. Hyperspectral retrievals of phytoplankton absorption and chlorophyll-a in inland and nearshore coastal waters. Remote Sens. Environ. 253, 112200. https://doi.org/10.1016/j.rse.2020.112200.
Painter, T.H., Duval, B., Thomas, W.H., Mendez, M., Heintzelman, S., Dozier, J., 2001. Detection and quantification of snow algae with an airborne imaging spectrometer. Appl. Environ. Microbiol. 67 (11), 5267–5272. https://doi.org/10.1128/AEM.67.11.5267-5272.2001.
Painter, T.H., Dozier, J., Roberts, D.A., Davis, R.E., Green, R.O., 2003. Retrieval of subpixel snow-covered area and grain size from imaging spectrometer data. Remote Sens. Environ. 85 (1), 64–77. https://doi.org/10.1016/S0034-4257(02)00187-6.
Painter, T.H., Seidel, F.C., Bryant, A.C., Skiles, S.M., Rittger, K., 2013. Imaging spectroscopy of albedo and radiative forcing by light-absorbing impurities in mountain snow. J. Geophys. Res.-Atmos. 118 (17), 9511–9523. https://doi.org/10.1002/jgrd.50520.
Painter, T.H., Berisford, D.F., Boardman, J.W., Bormann, K.J., Deems, J.S., Gehrke, F., Hedrick, A., Joyce, M., Laidlaw, R., Marks, D., Mattmann, C., McGurk, B., Ramirez, P., Richardson, M., Skiles, S.K., Seidel, F.C., Winstral, A., 2016. The airborne snow observatory: fusion of scanning lidar, imaging spectrometer, and physically-based modeling for mapping snow water equivalent and snow albedo. Remote Sens. Environ. 184, 139–152. https://doi.org/10.1016/j.rse.2016.06.018.
Palacios, S.L., Peterson, T.D., Kudela, R.M., 2009. Development of synthetic salinity from remote sensing for the Columbia River plume. J. Geophys. Res. Oceans 114 (C2). https://doi.org/10.1029/2008JC004895.
Palacios, S.L., Kudela, R.M., Guild, L.S., Negrey, K.H., Torres-Perez, J., Broughton, J., 2015. Remote sensing of phytoplankton functional types in the coastal ocean from the HyspIRI preparatory flight campaign. Remote Sens. Environ. 167, 269–280. https://doi.org/10.1016/j.rse.2015.05.014.
Pande, H., Tiwari, P.S., 2013. High-resolution and hyperspectral data fusion for classification. In: Miao, Q. (Ed.), New Advances in Image Fusion, pp. 57–77. https://doi.org/10.5772/56944.
Perkins, T., Adler-Golden, S., Matthew, M.W., Berk, A., Bernstein, L.S., Lee, J., Fox, M., 2012. Speed and accuracy improvements in FLAASH atmospheric correction of hyperspectral imagery. Opt. Eng. 51 https://doi.org/10.1117/1.OE.51.11.111707, 11707–1–11707–7.
Polhamus, A., Fisher, J.B., Tu, K.P., 2013. What controls the error structure in evapotranspiration models? Agric. For. Meteorol. 169, 12–24. https://doi.org/10.1016/j.agrformet.2012.10.002.
Pottier, J., Malenovský, Z., Psomas, A., Homolová, L., Schaepman, M.E., et al., 2014. Modelling plant species distribution in alpine grasslands using airborne imaging spectroscopy. Biol. Lett. 10 https://doi.org/10.1098/rsbl.2014.0347.
Poulter, B., MacBean, N., Hartley, A., Khlystova, I., Arino, O., Betts, R., Bontemps, S., Boettcher, M., Brockman, C., Defourny, P., Hagemann, S., Herold, M., Kirches, G., Lamarche, C., Lederer, D., Ottlé, C., Peters, M., Peylin, P., 2015. Plant functional type classification for earth system models: results from the European Space Agency's land cover climate change initiative. Geosci. Model Dev. 8, 2315–2328. https://doi.org/10.5194/gmd-8-2315-2015.
Prata, A.J., 1989a. Infrared radiative transfer calculations for volcanic ash clouds. Geophys. Res. Lett. 16 (11), 1293–1296. https://doi.org/10.1029/GL016i011p01293.
Prata, A.J., 1989b. Observations of volcanic ash clouds in the 10-12 um window using AVHRR/2 data. Int. J. Remote Sens. 10 (4), 751–761. https://doi.org/10.1080/01431168908903916.
Prata, A.J., 1994. Land-surface temperatures derived from the advanced very high-resolution radiometer and the along-track scanning radiometer.2. Experimental results and validation of AVHRR algorithms. J. Geophys. Res.-Atmos. 99, 13025–13058. https://doi.org/10.1029/94JD00409.
Prata, A.J., Bernardo, C., 2007. Retrieval of volcanic SO2 column abundance from atmospheric infrared sounder data. J. Geophys. Res. 112, D20204. https://doi.org/10.1029/2006JD007955.
Prata, F., Lynch, M., 2019. Passive earth observations of volcanic clouds in the atmosphere. Atmosphere 10, 199. https://doi.org/10.3390/atmos10040199.
Prata, A.J., Prata, A.T., 2012. Eyjafjallajokull volcanic ash concentrations determined using Spin Enhanced Visible and Infrared Imager measurements. J. Geophys. Res. 117, DU00U23. https://doi.org/10.1029/2011JD016800.
Price, J.C., 1984. Land surface temperature measurements from the split window channels of the NOAA 7 advanced very high resolution radiometer. J. Geophys. Res. 89, 7231–7237. https://doi.org/10.1029/JD089iD05p07231.
Qi, Lin, Hu, Chuanmin, Mikelsons, Karlis, Wang, Menghua, Lance, Veronica, Sun, Shaojie, Barnes, Brian B., Zhao, Jun, 2020. In search of floating algae and other organisms in global oceans and lakes. Rem. Sens. Environ. 239, 111659. https://doi.org/10.1016/j.rse.2020.111659 (ISSN 0034-4257).
Qi, L., Hu, C., Duan, H., Cannizzaro, J., Ma, R., 2014. A novel MERIS algorithm to derive cyanobacterial phycocyanin pigment concentrations in a eutrophic lake: theoretical basis and practical considerations. Remote Sens. Environ. 154, 298–317. https://doi.org/10.1016/j.rse.2014.08.026.
Qi, L., Hu, C., Xing, Q., Shang, S., 2016. Long-term trend of Ulva prolifera blooms in the western Yellow Sea. Harmful Algae 58, 35–44. https://doi.org/10.1016/j.hal.2016.07.004.
Qi, L.C.H., Mikelsons, K., Wang, M., Lance, V., others, 2019a. In search of floating algae and other organisms in global oceans and lakes. Remote Sens. Environ. 239, 111659. https://doi.org/10.1016/j.rse.2020.111659.
Qi, L., Tsai, S.-F., Chen, Y., Le, C., Hu, C., 2019b. In search of red Noctiluca scintillans blooms in the East China Sea (2019). Geophys. Res. Lett. 46, 5997–6004. https://doi.org/10.1029/2019GL082667.
Queißer, M., Burton, M., Kazahaya, R., 2019. Insights into geological processes with CO2 remote sensing: A review of technology and applications. Earth Sci. Rev. 188, 389–426. https://doi.org/10.1016/j.earscirev.2018.11.016.
Ramsey, M.S., Harris, A.J., 2013. Volcanology 2020: how will thermal remote sensing of volcanic surface activity evolve over the next decade? J. Volcanol. Geotherm. Res. 249, 217–233. https://doi.org/10.1016/j.jvolgeores.2012.05.011.
Randin, C.F., Ashcroft, M.B., Bolliger, J., Cavender-Bares, J., Coops, N.C., others, 2020. Monitoring biodiversity in the Anthropocene using remote sensing in species distribution models. Remote Sens. Environ. 239 (11162), 6. https://doi.org/10.1016/j.rse.2019.111626.
Realmuto, V.J., Berk, A., 2016. Plume tracker: interactive mapping of volcanic sulfur dioxide emissions with high-performance radiative transfer modeling. J. Volcanol. Geotherm. Res. 327, 55–69. https://doi.org/10.1016/j.jvolgeores.2016.07.001.
Realmuto, V.J., Abrams, M.J., Buongiorno, M.F., Pieri, D.C., 1994. The use of multispectral thermal infrared image data to estimate the sulfur dioxide flux from volcanoes: A case study from Mount Etna, Sicily, July 29, 1986. J. Geophys. Res. 99 (B1), 481–488. https://doi.org/10.1029/93JB02062.
Realmuto, V.J., Sutton, A.J., Elias, T., 1997. Multispectral thermal infrared mapping of sulfur dioxide plumes: A case study from the East Rift Zone of Kilauea Volcano,

Hawaii. J. Geophys. Res. 102 (B7), 15057–15072. https://doi.org/10.1029/96JB03916.
Realmuto, V.J., Dennison, P.E., Foote, M., Ramsey, M.S., Wooster, M.J., Wright, R., 2015. Specifying the saturation temperature for the HyspIRI 4-μm channel. Remote Sens. Environ. 167, 40–52. https://doi.org/10.1016/j.rse.2015.04.028.
Richter, R., Schläpfer, D., 2017. *Atmospheric / Topographic Correction for Satellite Imagery*. DLR Report DLR-IB 565–02/15, Wessling, Germany, p. 252. http://www.rese-apps.com.
Rittger, K., Painter, T.H., Dozier, J., 2013. Assessment of methods for mapping snow cover from MODIS. Adv. Water Resour. 51, 367–380. https://doi.org/10.1016/j.advwatres.2012.03.002.
Roberts, D.A., Gardner, M., Church, R., Ustin, S., Scheer, G., Green, R.O., 1998. Mapping chaparral in the Santa Monica mountains using multiple endmember spectral mixture models. Remote Sens. Environ. 65 (3), 267–279. https://doi.org/10.1016/S0034-4257(98)00037-6.
Roberts, G., Wooster, M.J., Perry, G.L., Drake, N., Rebelo, L.M., Dipotso, F., 2005. Retrieval of biomass combustion rates and totals from fire radiative power observations: application to southern Africa using geostationary SEVIRI imagery. J. Geophys. Res.-Atmos. 110 (D21) https://doi.org/10.1029/2005JD006018.
Roberts, D.A., Dennison, P.E., Roth, K.L., Dudley, K., Hulley, G., 2015. Relationships between dominant plant species, fractional cover and land surface temperature in a Mediterranean ecosystem. Remote Sens. Environ. 167, 152–167. https://doi.org/10.1016/j.rse.2015.01.026.
Rocchini, D., Balkenhol, N., Carter, G.A., Foody, G.M., Gillespie, T.W., et al., 2010. Remotely sensed spectral heterogeneity as a proxy of species diversity: recent advances and open challenges. Ecol. Informat. 5, 318–329. https://doi.org/10.1016/j.ecoinf.2010.06.001.
Roesler, C.S., Etheridge, S.M., Pitcher, G.C., 2003. Application of an ocean color algal taxa detection model to red tides in the Southern Benguela. In: Proceedings of the Xth International Conference on Harmful Algae. https://pace.odyseallc.net/docs/Roesler_et_al_XHAB_202003_Ref.pdf.
Rogge, D., Rivard, B., Segl, K., Grant, B., Feng, J., 2014. Mapping of NiCu-PGE ore hosting ultramafic rocks using airborne and simulated EnMAP hyperspectral imagery, Nunavik, Canada. Remote Sens. Environ. 152, 302–317. https://doi.org/10.1016/j.rse.2014.06.024.
Romaniello, V., Spinetti, C., Silvestri, M., Buongiorno, M.F., 2020. A sensitivity study of the 4.8 μm carbon dioxide absorption band in the MWIR spectral range. Remote Sens. 12 (1), 172. https://doi.org/10.3390/rs12010172.
Rossi, C., Kneubuhler, M., Schutz, M., Schaepman, M.E., Haller, R.M., Risch, A.C., 2020. From local to regional: functional diversity in differently managed alpine grasslands. Remote Sens. Environ. 236, 111415 https://doi.org/10.1016/j.rse.2019.111415.
Ryan, J.P., Davis, C.O., Tufillaro, N.B., Kudela, R.M., Gao, B.-C., 2014. Application of the hyperspectral imager for the Coastal Ocean to phytoplankton ecology studies in Monterey Bay, CA, USA. Remote Sens. 6, 1007–1025. https://doi.org/10.3390/rs6021007.
Sadeghi, A., Dinter, T., Vountas, M., Taylor, B., Altenburg-Soppa, M., Bracher, A., 2012. Remote sensing of coccolithophore blooms in selected oceanic regions using the PhytoDOAS method applied to hyper-spectral satellite data. Biogeosciences 9 (6), 2127–2143. https://doi.org/10.5194/bg-9-2127-2012.
Schaepman, M.E., Ustin, S.L., Plaza, A.J., Painter, T.H., Verrelst, J., Liang, S., 2009. Earth system science related imaging spectroscopy–an assessment. Remote Sens. Environ. 113, S123–S137. https://doi.org/10.1016/j.rse.2009.03.001.
Schaepman-Strub, G., Schaepman, M.E., Painter, T.H., Dangel, S., Martonchik, J.V., 2006. Reflectance quantities in optical remote sensing—definitions and case studies. Remote Sens. Environ. 103, 27–42. https://doi.org/10.1016/j.rse.2006.03.002.
Schimel, D., Townsend, P.A., Pavlick, R., 2020. Prospects and pitfalls for spectroscopic remote sensing of biodiversity at the global scale. In: Cavender-Bares, J., Gamon, J., Townsend, P. (Eds.), Remote Sensing of Plant Biodiversity. Springer. https://doi.org/10.1007/978-3-030-33157-3_19.
Schlapfer, D., Richter, R., Feingersh, T., 2015. Operational BRDF effects correction for wide-field-of-view optical scanners (BREFCOR). IEEE Trans. Geosci. Remote Sens. 53 (4), 1855–1864. https://doi.org/10.1109/TGRS.2014.2349946.
Schmidtlein, S., Zimmermann, P., Schupferling, R., Weiss, C., 2007. Mapping the floristic continuum: ordination space position estimated from imaging spectroscopy. J. Veg. Sci. 18, 131–140. https://doi.org/10.1111/j.1654-1103.2007.tb02523.x.
Schneider, F.D., Morsdorf, F., Schmid, B., Petchey, O.L., Hueni, A., Schimel, D.S., Schaepman, M.E., 2017. Mapping functional diversity from remotely sensed morphological and physiological forest traits. Nat. Commun. 8, 1441. https://doi.org/10.1038/s41467-017-01530-3.
Schneider, F.D., Ferraz, A., Schimel, D., 2019. Watching Earth's interconnected systems at work. Eos 100. https://eos.org/science-updates/watching-earths-interconnected-systems-at-work.
Schwandner, F.M., Gunson, M.R., Miller, C.E., Carn, S.A., Eldering, A., Krings, T., Verhulst, K.R., Schimel, D.S., Nguyen, H.M., Crisp, D., et al., 2017. Spaceborne detection of localized carbon dioxide sources. Science 358. https://doi.org/10.1126/science.aam5782 eaam5782.
Schweiger, A.K., 2020. Spectral field campaigns: planning and data collection. In: Cavender-Bares, J., Gamon, J.A., Townsend, P.A. (Eds.), *Remote Sensing of Plant Biodiversity* (Pp. 385–423). Springer International Publishing. https://doi.org/10.1007/978-3-030-33157-3_15.
Schweiger, A.K., Cavender-Bares, J., Townsend, P.A., Hobbie, S.E., Madritch, M.D., Wang, R., Tilman, D., Gamon, J.A., 2018. Plant spectral diversity integrates functional and phylogenetic components of biodiversity and predicts ecosystem function. Nat. Ecol. Evolut. 2 (6), 976–982. https://doi.org/10.1038/s41559-018-0551-1.
Serbin, S.P., Townsend, P.A., 2020. Scaling functional traits from leaves to canopies. In: Cavender-Bares, J., Gamon, J.A., Townsend, P.A. (Eds.), *Remote Sensing of Plant Biodiversity* (Pp. 43–82). Springer International Publishing. https://doi.org/10.1007/978-3-030-33157-3_3.
Serbin, S.P., Dillaway, D.N., Kruger, E.L., Townsend, P.A., 2012. Leaf optical properties reflect variation in photosynthetic metabolism and its sensitivity to temperature. J. Exp. Bot. 63 (1), 489–502. https://doi.org/10.1093/jxb/err294.
Serbin, S.P., Singh, A., McNeil, B.E., Kingdon, C.C., Townsend, P.A., 2014. Spectroscopic determination of leaf morphological and biochemical traits for northern temperate and boreal tree species. Ecol. Appl. 24, 1651–1669. https://doi.org/10.1890/13-2110.1.
Serbin, S.P., Singh, A., Desai, A.R., Dubois, S.G., Jablonski, A.D., Kingdon, C.C., Kruger, E.L., Townsend, P.A., 2015. Remotely estimating photosynthetic capacity, and its response to temperature in vegetation canopies using imaging spectroscopy. Remote Sens. Environ. 167, 78–87. https://doi.org/10.1016/j.rse.2015.05.024.
Serbin, S.P., Wu, J., Ely, K.S., Kruger, E.L., Townsend, P.A., Meng, R., Wolfe, B.T., Chlus, A., Wang, Z., Rogers, A., 2019. From the Arctic to the tropics: multibiome prediction of leaf mass per area using leaf reflectance. New Phytol. 224, 1557–1568. https://doi.org/10.1111/nph.16123.
Shiklomanov, A.N., Dietze, M.C., Viskari, T., Townsend, P.A., Serbin, S.P., 2016. Quantifying the influences of spectral resolution on uncertainty in leaf trait estimates through a Bayesian approach to RTM inversion. Remote Sens. Environ. 183, 226–238. https://doi.org/10.1016/j.rse.2016.05.023.
Shipman, H., Adams, J.B., 1987. Detectability of minerals on desert alluvial fans using reflectance spectra. J. Geophys. Res. 92 (B10), 10391–10402. https://doi.org/10.1029/JB092iB10p10391.
Silsbe, G.M., Behrenfeld, M.J., Halsey, K.H., Milligan, A.J., Westberry, T.K., 2016. The CAFE model: A net production model for global ocean phytoplankton. Glob. Biogeochem. Cycles 30, 1756–1777. https://doi.org/10.1002/2016GB005521.
Simard, M., Zhang, K., Rivera-Monroy, V.H., Ross, M.S., Ruiz, P.L., Castañeda-Moya, E., Twilley, R.R., Rodriguez, E., 2006. Mapping height and biomass of mangrove forests in Everglades National Park with SRTM elevation data. Photogramm. Eng. Remote. Sens. 72 (3), 299–311. https://doi.org/10.14358/PERS.72.3.299.
Singh, A., Serbin, S.P., McNeil, B.E., Kingdon, C.C., Townsend, P.A., 2015. Imaging spectroscopy algorithms for mapping canopy foliar chemical and morphological traits and their uncertainties. Ecol. Appl. 25, 2180–2197. https://doi.org/10.1890/14-2098.1.
Smith, M.E., Bernard, S., 2020. Satellite ocean color based harmful algal bloom indicators for aquaculture decision support in the Southern Benguela. Front. Mar. Sci. 7, 61. https://doi.org/10.3389/fmars.2020.00061.
Smith, M.O., Roberts, D.A., Hill, J., et al., 1994. A new approach to determining spectral abundances of mixtures in multispectral images. IEEE Trans. Geosci. Remote Sens. https://doi.org/10.1109/IGARSS.1994.399741. Proc. IGARSS '94.
Soenen, S.A., Peddle, D.R., Coburn, C.A., 2005. SCS+C: A modified Sun-Canopy-Sensor topographic correction in forested terrain. IEEE Trans. Geosci. Remote Sens. 43 (9), 2148–2159. https://doi.org/10.1109/TGRS.2005.852480.
Somers, B., Asner, G.P., Martin, R.E., Anderson, C.B., Knapp, D.E., et al., 2015. Mesoscale assessment of changes in tropical tree species richness across a bioclimatic gradient in Panama using airborne imaging spectroscopy. Remote Sens. Environ. 167, 111–120. https://doi.org/10.1016/j.rse.2015.04.016.
Soto, I., Muller-Karger, F.E., Hu, C., Wolny, J., 2016. Characterization of Karenia brevis blooms on the West Florida shelf using ocean color satellite imagery: implications for bloom maintenance and evolution. J. Appl. Remote. Sens. 11 (1), 012002. https://doi.org/10.1117/1.JRS.11.012002.
Sousa, D., Davis, F.W., 2020. Scalable mapping and monitoring of Mediterranean-climate oak landscapes with temporal mixture models. Remote Sens. Environ. 247 (11193), 7. https://doi.org/10.1016/j.rse.2020.111937.
Stamnes, K., Li, W., Eide, H., Aoki, T., Hori, M., Storvold, R., 2007. ADEOS-II/GLI snow/ice products—part I: scientific basis. Remote Sens. Environ. 111 (2–3), 258–273. https://doi.org/10.1016/j.rse.2007.03.023.
Steinmetz, F., Deschamps, P.-Y., Ramon, D., 2011. Atmospheric correction in presence of sun glint: application to MERIS. Opt. Express 19, 9783–9800. https://doi.org/10.1364/OE.19.009783.
Stocker, A.D., 1990. Multi-dimensional signal processing for electro-optical target detection. In: Signal and Data Processing of Small Targets 1990, Vol. 1305. International Society for Optics and Photonics, p. 218. https://doi.org/10.1117/12.2321763.
Stramski, D., Reynolds, R.A., Babin, M., Kaczmarek, S., Lewis, M.R., Röttgers, R., Claustre, H., 2008. Relationships between the surface concentration of particulate organic carbon and optical properties in the eastern South Pacific and eastern Atlantic Oceans. Biogeosciences 5 (1), 171–201. https://doi.org/10.5194/bg-5-171-2008.
Stroud, W.G., 1960. Initial results of the TIROS I meteorological satellite. J. Geophys. Res. 65 (5), 1643. https://doi.org/10.1029/JZ065i005p01643.
Stumpf, R.P., 2001. Applications of satellite ocean color sensors for monitoring and predicting harmful algal blooms. Human Ecol. Risk Assess. 7 (5), 1363–1368. https://doi.org/10.1080/20018091095050.
Stumpf, R.P., Davis, T.W., Wynne, T.T., Graham, J.L., Loftin, K.A., Johengen, T.H., Gossiaux, D., Palladino, D., Burtner, A., 2016. Challenges for mapping cyanotoxin patterns from remote sensing of cyanobacteria. Harmful Algae 54, 160–173. https://doi.org/10.1016/j.hal.2016.01.005.
Su, Z., 2002. The surface energy balance system (SEBS) for estimation of turbulent heat fluxes. Hydrol. Earth Syst. Sci. 6, 85–99. https://doi.org/10.5194/hess-6-85-2002.
Sun, S., Hu, C., 2019. The challenges of interpreting oil-water spatial and spectral contrasts for the estimation of oil thickness: examples from satellite and airborne

measurements of the Deepwater horizon oil spill. IEEE Trans. Geosci. Remote Sens. 57, 2643–2658. https://doi.org/10.1109/TGRS.2018.2876091.
Swayze, G.A., Smith, K.S., Clark, R.N., Sutley, S.J., Pearson, R.N., Rust, G.S., Vance, J.S., Hageman, P.L., Briggs, P.H., Meier, A.L., Singleton, M.J., Roth, S., 2000. Using imaging spectroscopy to map acidic mine waste. Environ. Sci. Technol. 34 (1), 47–54. https://doi.org/10.1021/es990046w.
Swayze, G.A., Clark, R.N., Goetz, A.F.H., Chrien, T.G., G, N.S., 2003. Effects of spectrometer bandpass, sampling, and signal-to-noise ratio on spectral identification using the Tetracorder algorithm. J. Geophys. Res. 108 (E9), 5105. https://doi.org/10.1029/2002JE001975.
Swayze, G., Kokaly, R., Higgins, C., Clinkenbeard, J., Clark, R., Lowers, H., Sutley, S., 2009. Mapping potentially asbestos-bearing rocks using imaging spectroscopy. Geology 37 (8), 763–766. https://doi.org/10.1130/G30114A.1.
Swayze, G.A., Clark, R.N., Goetz, A.F., Livo, K.E., Breit, G.N., Kruse, F.A., Sutley, S.J., Snee, L.W., Lowers, H.A., Post, J.L., Stoffregen, R.E., 2014. Mapping advanced argillic alteration at Cuprite, Nevada, using imaging spectroscopy. Econ. Geol. 109 (5), 1179–1221. https://doi.org/10.2113/econgeo.109.5.1179.
Tane, Z., Roberts, D., Veraverbeke, S., Casas, Á., Ramirez, C., Ustin, S., 2018. Evaluating endmember and band selection techniques for multiple endmember spectral mixture analysis using post-fire imaging spectroscopy. Remote Sens. 10, 389. https://doi.org/10.3390/rs10030389.
Thenkabail, P.S.L., G, J., Huete, A., 2018. Hyperspectral Indices and Image Classifications for Agriculture and Vegetation, 2nd edition. Taylor and Francis. https://doi.org/10.1201/9781315159331.
Thompson, D.R., Thorpe, A.K., Frankenberg, C., Green, R.O., Duren, R., Guanter, L., Hollstein, A., Middleton, E., Ong, L., Ungar, S., 2016. Space-based remote imaging spectroscopy of the Aliso Canyon CH4 superemitter. Geophys. Res. Lett. 43 (12), 6571–6578. https://doi.org/10.1002/2016GL069079.
Thompson, D.R., Boardman, J.W., Green, R.O., Eastwood, M., 2017a. A large airborne survey of Earth's visible-infrared spectral dimensionality. Opt. Express 25 (8), 9186–9195. https://doi.org/10.1364/OE.25.009186.
Thompson, D.R., Hochberg, E.J., Asner, G.P., Green, R.O., Knapp, D.E., Gao, B.-C., Garcia, R., Gierach, M., Lee, Z., Maritorena, S., Fick, R., 2017b. Airborne mapping of benthic reflectance spectra with Bayesian linear mixtures. Remote Sens. Environ. 200, 18–30. https://doi.org/10.1016/j.rse.2017.07.030.
Thompson, D.R., Natraj, V., Green, R.O., Helmlinger, M., Gao, B.-C., Eastwood, M.L., 2018. Optimal estimation for imaging spectrometer atmospheric correction. Remote Sens. Environ. 216, 355–373. https://doi.org/10.1016/j.rse.2018.07.003.
Thompson, D.R., Babu, K.N., Braverman, A., Eastwood, M., Green, R.O., Hobbs, J., Jewell, J.B., Mishra, M., Mathur, A., Natraj, V., Seidel, F.C., Townsend, P., Turmon, M., 2019a. Optimal estimation of spectral surface reflectance in challenging atmospheres. Remote Sens. Environ. 232 (11125), 8. https://doi.org/10.1016/j.rse.2019.111258.
Thompson, D.R., Cawse-Nicholson, K., Erickson, Z., Fichot, C., Frankenberg, C., Gao, B.-C., Gierach, M.M., Green, R.O., Jensen, D., Natraj, V., Thompson, A., 2019b. A unified approach to estimate land and water reflectances with uncertainties for coastal imaging spectroscopy. Remote Sens. Environ. 231 (11119), 8. https://doi.org/10.1016/j.rse.2019.05.017.
Thompson, D.R., Guanter, L., Berk, A., Gao, B.-C., Richter, R., Schläpfer, D., Thome, K.J., 2019c. Retrieval of atmospheric parameters and surface reflectance from visible and shortwave infrared imaging spectroscopy data. Surv. Geophys. 40 (3), 333–360. https://doi.org/10.1007/s10712-018-9488-9.
Thonicke, K., Billing, M., von Bloh, W., Sakschewski, B., Niinemets, U., Penuelas, J., Cornelissen, J.H.C., Onoda, Y., van Bodegom, P., Schaepman, M.E., Schneider, F.D., Walz, A., 2020. Simulating functional diversity of European natural forests along climatic gradients. J. Biogeogr. 47, 1069–1085. https://doi.org/10.1111/jbi.13809.
Thorpe, A.K., Frankenberg, C., Roberts, D.A., 2014. Retrieval techniques for airborne imaging of methane concentrations using high spatial and moderate spectral resolution: application to AVIRIS. Atmos. Measur. Techn. 7 (2), 491–506. https://doi.org/10.5194/amt-7-491-2014.
Thorpe, A.K., Frankenberg, C., Thompson, D.R., Duren, R.M., Aubrey, A.D., Bue, B.D., Green, R.O., Gerilowski, K., Krings, T., Borchardt, J., Kort, E.A., 2017. Airborne DOAS retrievals of methane, carbon dioxide, and water vapor concentrations at high spatial resolution: application to AVIRIS-NG. Atmos. Measur. Techn. 10 (10), 3833–3850. https://doi.org/10.5194/amt-10-3833-2017.
Torres-Pérez, J.L., Guild, L.S., Armstrong, R.A., 2012. Hyperspectral distinction of two Caribbean shallow-water corals based on their pigments and corresponding reflectance. Remote Sens. 4, 3813–3832. https://doi.org/10.3390/rs4123813.
Torres-Pérez, J.L., Guild, L.S., Armstrong, R.A., Corredor, J., Zuluaga-Montero, A., others, 2015. Relative pigment composition and remote sensing reflectance of Caribbean shallow-water corals. PLoS One 10 (11), e0143709. https://doi.org/10.1371/journal.pone.0143709.
Townsend, P.A., Walsh, S.J., 2001. Remote sensing of forested wetlands: application of multitemporal and multispectral satellite imagery to determine plant community composition and structure in southeastern USA. Plant Ecol. 157, 129–149. https://doi.org/10.1023/A:1013999513172.
Trunk, L., Bernard, A., 2008. Investigating crater lake warming using ASTER thermal imagery: case studies at Ruapehu, Poás, Kawah Ijen, and Copahué volcanoes. J. Volcanol. Geotherm. Res. 178 (2), 259–270. https://doi.org/10.1016/j.jvolgeores.2008.06.020.
Truslow, E., Manolakis, D., Pieper, M., Cooley, T., Brueggeman, M., 2013. Performance prediction of matched filter and adaptive cosine estimator hyperspectral target detectors. IEEE J. Selected Top. Appl. Earth Observat. Remote Sens. 7 (6), 2337–2350. https://doi.org/10.1109/JSTARS.2013.2272697.
Tukiainen, T., Thomassen, B., 2010. Application of airborne hyperspectral data to mineral exploration in north-East Greenland. Geol. Surv. Denmark Greenland Bull. 20, 71–74. https://doi.org/10.34194/geusb.v20.4982.
Turpie, K.R., 2013. Explaining the spectral red-edge features of inundated marsh vegetation. J. Coast. Res. 29 (5), 1111–1117. https://doi.org/10.2112/JCOASTRES-D-12-00209.1.
Turpie, K.R., Abelev, A., Babin, M., Bachmann, C., Bell, T., Brando, V., Byrd, K., Dekker, A., Devred, E., Forget, M.-H., Goodman, J., Guild, L., Hochberg, E., Hu, C., Jo, Y.-H., Kelly, M., Klemas, V., Lee, Z.-P., Moisan, T., Yu, Q., 2015a. Coastal and Inland Aquatic Data Products for the Hyperspectral Infrared Imager (HyspIRI). Goddard Space Flight Center Greenbelt, Maryland 20771. https://hyspiri.jpl.nasa.gov/downloads/reports_whitepapers/HASG_White_Paper_Report_20150226_v3.pdf.
Turpie, K.R., Klemas, V.V., Byrd, K., Kelly, M., Jo, Y.H., 2015b. Prospective HyspIRI global observations of tidal wetlands. Remote Sens. Environ. 167, 206–217. https://doi.org/10.1016/j.rse.2015.05.008.
Twardowski, M., Tonizzo, A., 2018. Ocean color analytical model explicitly dependent on the volume scattering function. Appl. Sci. 8 (12), 2684. https://doi.org/10.3390/app8122684.
Tzortziou, M., Herman, J.R., Ahmad, Z., Loughner, C.P., Abuhassan, N., Cede, A., 2014. Atmospheric NO2 dynamics and impact on ocean color retrievals in urban nearshore regions. J. Geophys. Res. Oceans 119 (6), 3834–3854. https://doi.org/10.1002/2014JC009803.
Urquhart, E.A., Zaitchik, B.F., Hoffman, M.J., Guikema, S.D., Geiger, E.F., 2012. Remotely sensed estimates of surface salinity in the Chesapeake Bay: A statistical approach. Remote Sens. Environ. 123, 522–531. https://doi.org/10.1016/j.rse.2012.04.008.
Ustin, S.L., 2013. Remote sensing of canopy chemistry. Proc. Natl. Acad. Sci. 110 (3), 804–805. https://doi.org/10.1073/pnas.1219393110.
Ustin, S.L., Gamon, J.A., 2010. Remote sensing of plant functional types: Tansley review. New Phytol. 186 (4), 795–816. https://doi.org/10.1111/j.1469-8137.2010.03284.x.
van der Meer, F.D., van der Werff, H.M., van Ruitenbeek, F.J., Hecker, C.A., Bakker, W.H., Noomen, M.F., van der Meijde, M., Carranza, E.J.M., de Smeth, J.B., Woldai, T., 2012. Multi-and hyperspectral geologic remote sensing: A review. Int. J. Appl. Earth Obs. Geoinf. 14, 112–128. https://doi.org/10.1016/j.jag.2011.08.002.
Vermote, E., Ellicott, E., Dubovik, O., Lapyonok, T., Chin, M., Giglio, L., Roberts, G.J., 2009. An approach to estimate global biomass burning emissions of organic and black carbon from MODIS fire radiative power. J. Geophys. Res.-Atmos. 114 (D18) https://doi.org/10.1029/2008JD011188.
Verrelst, J., Alonso, L., Rivera Caicedo, J.P., Moreno, J., Camps-Valls, G., 2013. Gaussian process retrieval of chlorophyll content from imaging spectroscopy data. IEEE J. Selected Top. Appl. Earth Observat. Remote Sens. 6, 2. https://doi.org/10.1109/JSTARS.2012.2222356.
Verrelst, J., Rivera Caicedo, J.P., Muñoz-Marí, J., Camps-Valls, G., Moreno, J., 2017. SCOPE-based emulators for fast generation of synthetic canopy reflectance and sun-induced fluorescence spectra. Remote Sens. 9, 927. https://doi.org/10.3390/rs9090927.
Verrelst, J., Malenovský, Z., Van der Tol, C., et al., 2019. Quantifying vegetation biophysical variables from imaging spectroscopy data: A review on retrieval methods. Surv. Geophys. *40*, 589–629. https://doi.org/10.1007/s10712-018-9478-y.
Vögtli, M., Schläpfer, D., Richter, R., Hueni, A., Schaepman, M.E., Kneubühler, M., 2021. About the transferability of topographic correction methods from spaceborne to airborne optical data. IEEE J. Selected Top. Appl. Earth Observat. Remote Sens. 14, 1348–1362. https://doi.org/10.1109/JSTARS.2020.3039327.
Wan, Z.M., Dozier, J., 1996. A generalized split-window algorithm for retrieving land-surface temperature from space. IEEE Trans. Geosci. Remote Sens. 34, 892–905. https://doi.org/10.1109/36.508406.
Wan, Z.M., Li, Z.L., 1997. A physics-based algorithm for retrieving land-surface emissivity and temperature from EOS/MODIS data. IEEE Trans. Geosci. Remote Sens. 35, 980–996. https://doi.org/10.1109/36.602541.
Wang, M., 2007. Remote sensing of the ocean contributions from ultraviolet to near-infrared using the shortwave infrared bands: simulations. Appl. Opt. 46, 1535–1547. https://doi.org/10.1364/AO.46.001535.
Wang, M., Bailey, S.W., 2001. Correction of sun glint contamination on the SeaWiFS ocean and atmosphere products. Appl. Opt. 40, 4790–4798. https://doi.org/10.1364/AO.40.004790.
Wang, R., Gamon, J., 2019. Remote sensing of terrestrial plant biodiversity. Remote Sens. Environ. 231, 1–15. https://doi.org/10.1016/j.rse.2019.111218.
Wang, M., Hu, C., 2016. Mapping and quantifying Sargassum distribution and coverage in the central West Atlantic using MODIS observations. Remote Sens. Environ. 183, 350–367. https://doi.org/10.1016/j.rse.2016.04.019.
Wang, G., Lee, Z., Mishra, D.R., Ma, R., 2016. Retrieving absorption coefficients of multiple phytoplankton pigments from hyperspectral remote sensing reflectance measured over cyanobacteria bloom waters. Limnol. Oceanogr. Methods 14 (7), 432–447. https://doi.org/10.1002/lom3.10102.
Wang, Z., Skidmore, A.K., Wang, T., Darvishzadeh, R., Heiden, U., Heurich, M., Latifi, H., Hearne, J., 2017. Canopy foliar nitrogen retrieved from airborne hyperspectral imagery by correcting for canopy structure effects. Int. J. Appl. Earth Obs. Geoinf. 54, 84–94. https://doi.org/10.1016/j.jag.2016.09.008.
Wang, M., Hu, C., Cannizzaro, J., English, D., Han, X., Naar, D., et al., 2018. Remote sensing of Sargassum biomass, nutrients, and pigments. Geophys. Res. Lett. 45 (22), 12359–12367. https://doi.org/10.1029/2018GL078858.
Wang, Z., Townsend, P.A., Schweiger, A.K., Couture, J.J., Singh, A., Hobbie, S.E., Cavender-Bares, J., 2019. Mapping foliar functional traits and their uncertainties across three years in a grassland experiment. Remote Sens. Environ. 221, 405–416. https://doi.org/10.1016/j.rse.2018.11.016.

Wang, Z., Chlus, A., Geygan, R., Ye, Z., Zheng, T., Singh, A., Couture, J.J., Cavender-Bares, J., Kruger, E.L., Townsend, P.A., 2020. Foliar functional traits from imaging spectroscopy across biomes in eastern North America. New Phytol. 228, 494–511. https://doi.org/10.1111/nph.16711.

Wanner, W., Li, X., Strahler, A.H., 1995. On the derivation of kernels for kernel-driven models of bidirectional reflectance. J. Geophys. Res.-Atmos. 100 (D10), 21077–21089. https://doi.org/10.1029/95JD02371.

Wen, S., Rose, W.I., 1994. Retrieval of sizes and total masses of particles in volcanic clouds using AVHRR bands 4 and 5. J. Geophys. Res. 99 (D3), 5421–5431. https://doi.org/10.1029/93JD03340.

Wessman, C., Aber, J., Peterson, D., et al., 1988. Remote sensing of canopy chemistry and nitrogen cycling in temperate forest ecosystems. Nature *335*, 154–156. https://doi.org/10.1038/335154a0.

Westberry, T.K., Behrenfeld, M.J., 2014. Oceanic net primary production. In: Biophysical Applications of Satellite Remote Sensing. Springer, pp. 205–230.

Weyermann, J., Damm, A., Kneubühler, M., Schaepman, M.E., 2014. Correction of reflectance anisotropy effects of vegetation on airborne spectroscopy data and derived products. IEEE Trans. Geosci. Remote Sens. 52, 616–627. https://doi.org/10.1109/TGRS.2013.2242898.

Weyermann, J., Kneubühler, M., Schläpfer, D., Schaepman, M.E., 2015. Minimizing reflectance anisotropy effects in airborne spectroscopy data using Ross-Li model inversion with continuous field land cover stratification. IEEE Trans. Geosci. Remote Sens. 53, 5814–5823. https://doi.org/10.1109/TGRS.2015.2415872.

Wold, S., Sjöström, M., Eriksson, L., 2001. PLS-regression: A basic tool of chemometrics. Chemom. Intell. Lab. Syst. 58, 2. https://doi.org/10.1016/S0169-7439(01)00155-1.

Wooster, M.J., Zhukov, B., Oertel, D., 2003. Fire radiative energy for quantitative study of biomass burning: derivation from the BIRD experimental satellite and comparison to MODIS fire products. Remote Sens. Environ. 86 (1), 83–107. https://doi.org/10.1016/S0034-4257(03)00070-1.

Wooster, M.J., Xu, W., Nightingale, T., 2012. Sentinel-3 SLSTR active fire detection and FRP product: pre-launch algorithm development and performance evaluation using MODIS and ASTER datasets. Remote Sens. Environ. 120, 236–254. https://doi.org/10.1016/j.rse.2011.09.033.

Wooster, M.J., Roberts, G., Freeborn, P.H., Govaerts, Y., Beeby, R., He, J., Mullen, R., 2015. Meteosat SEVIRI Fire Radiative Power (FRP) products from the Land Surface Analysis Satellite Applications Facility (LSA SAF): Part 1-algorithms, product contents and analysis. Atmos. Chem. Phys. 15 (22), 13217–13239. https://doi.org/10.5194/acp-15-13217-2015.

Wright, R., Garbeil, H., Davies, A.G., 2010. Cooling rate of some active lavas determined using an orbital imaging spectrometer. J. Geophys. Res. Solid Earth 115 (B6). https://doi.org/10.1029/2009JB006536.

Wright, R., Glaze, L., Baloga, S.M., 2011. Constraints on determining the eruption style and composition of terrestrial lavas from space. Geology 39 (12), 1127–1130. https://doi.org/10.1130/G32341.1.

Wu, J., Rogers, A., Albert, L.P., Ely, K., Prohaska, N., Wolfe, B.T., Oliveira, R.C.J., Saleska, S.R., Serbin, S.P., 2019. Leaf reflectance spectroscopy captures variation in carboxylation capacity across species, canopy environment and leaf age in lowland moist tropical forests. New Phytol. 224, 663–674. https://doi.org/10.1111/nph.16029.

Wullschleger, S.D., Epstein, H.E., Box, E.O., Euskirchen, E.S., Goswami, S., Iversen, C.M., Kattge, J., Norby, R.J., van Bodegom, P.M., Xu, X., 2014. Plant functional types in earth system models: past experiences and future directions for application of dynamic vegetation models in high-latitude ecosystems. Ann. Bot. 114, 1–16. https://doi.org/10.1093/aob/mcu077.

Wynne, T.T., Stumpf, R.P., Tomlinson, M.C., Ransibrahmanakul, V., Villareal, T.A., 2005. Detecting Karenia brevis blooms and algal resuspension in the western Gulf of Mexico with satellite ocean color imagery. Harmful Algae 4 (6), 992–1003. https://doi.org/10.1016/j.hal.2005.02.004.

Xi, H., Hieronymi, M., Röttgers, R., Krasemann, H., Qiu, Z., 2015. Hyperspectral differentiation of phytoplankton taxonomic groups: A comparison between using remote sensing reflectance and absorption spectra. Remote Sens. 7, 14781–14805. https://doi.org/10.3390/rs71114781.

Xie, J., Kneubuhler, M., Garonna, I., Jong, R., Notarnicola, C., Gregorio, L.D., Schaepman, M.E., 2018. Relative influence of timing and accumulation of nnow on Alpine land surface phenology. J. Geophys. Res. Biogeosci. 123, 561–576. https://doi.org/10.1002/2017JG004099.

Yu, Y., Privette, J.L., Pinheiro, A.C., 2008. Evaluation of split-window land surface temperature algorithms for generating climate data records. IEEE Trans. Geosci. Remote Sens. 46, 179–192. https://doi.org/10.1109/TGRS.2007.909097.

Zhang, Q., Middleton, E.M., Gao, B., Cheng, Y., 2012. Using EO-1 Hyperion to simulate HyspIRI products for a coniferous forest: the fraction of PAR absorbed by chlorophyll fAPAR_chl and leaf water content (LWC). IEEE Trans. Geosci. Remote Sens. 50 (5), 1844–1852. https://doi.org/10.1109/TGRS.2011.2169267.

Zhang, G., Yao, T., Xie, H., Yang, K., Zhu, L., Shum, C.K., Bolch, T., Yi, S., Allen, S., Jiang, L., Chen, W., Ke, C., 2020a. Response of Tibetan plateau lakes to climate change: trends, patterns, and mechanisms. Earth Sci. Rev. 208 (10326), 9. https://doi.org/10.1016/j.earscirev.2020.103269.

Zhang, Q., Yao, T., Huemmrich, K.F., Middleton, E.M., Lyapustin, A.I., Wang, Y., 2020b. Evaluating impacts of snow, surface water, soil and vegetation on empirical vegetation and snow indices for the Utqiaġvik tundra ecosystem in Alaska with the LVS3 model. Remote Sens. Environ. 240 (11167), 7. https://doi.org/10.1016/j.rse.2020.111677.

Zheng, Z., Zeng, Y., Schneider, F.D., Zhao, Y., Zhao, D., Schmid, B., Schaepman, M.E., Morsdorf, F., 2021. Mapping functional diversity using individual tree-based morphological and physiological traits in a subtropical forest. Remote Sens. Environ. 112170. https://doi.org/10.1016/j.rse.2020.112170.

Zhu, W., Yu, Q., 2013. Inversion of chromophoric dissolved organic matter from EO-1 Hyperion imagery for turbid estuarine and coastal waters. IEEE Trans. Geosci. Remote Sens. 51 (6), 3286–3298. https://doi.org/10.1109/TGRS.2012.2224117.

Zhu, W., Yu, Q., Tian, Y.Q., Chen, R.F., Gardner, G.B., 2011. Estimation of chromophoric dissolved organic matter in the Mississippi and Atchafalaya river plume regions using above-surface hyperspectral remote sensing. J. Geophys. Res. 116 (C02011) https://doi.org/10.1029/2010JC006523.